A Study of Flow in Earth's Core Inferred from Satellite Magnetic Measurements

Master's Thesis

Andreas Clemens Kloss
June 2017

Supervisor:
Chris Finlay

DTU Space
National Space Institute

Abstract

Earth's magnetic field is primarily generated and maintained in the core region of the planet by a process known as the geodynamo. The working of the geodynamo is not well understood but thought to be a result of the vigorous motions of the liquid outer core. The changes of the observed field, referred to as secular variation (SV), are due to the induction action of the core motions on the core field. SV observations can therefore be used to infer the flow at the core surface although this is a highly non-unique inverse problem. The non-uniqueness is often reduced by making assumptions about the motions in the outer core (e.g. a large-scale assumption).

In this thesis, an new forward modeling scheme has been developed for predicting SV from core flow parameterized in terms of the normal modes of rotating flow in a sphere. Further, a new inversion scheme was developed using this basis of normal modes and an l_1-regularization of the mode amplitudes was implemented. The developed approach was used to estimate the core flow by inverting SV from a state-of-the-art geomagnetic field model (CHAOS-6-x2) at different epochs between 1999 and 2016. The normal modes are especially well-suited for studying flows at mid and low latitudes. A better understanding of the flow is of particular interest for the study of geomagnetic jerks and related secular acceleration (SA) pulses. The developed inversion scheme was successfully benchmarked against previous results. Strong time-dependent azimuthal flows were found in the equatorial region that could correctly predict localized pulses of increased SA at the core surface. In general, the developed inversion scheme is found to perform well, but further work is needed on how to best specify the prior information on the normal modes, and on linking more directly to satellite and ground magnetic field observations.

Acknowledgments

I would like to thank my supervisor, Chris Finlay, for his support and the valuable comments he gave me throughout my Master's thesis. He has also been contributing to the CHAOS-6 geomagnetic model which was used in this thesis. I would also like to thank Nicolas Gillet for providing the COV-OBS geomagnetic model and LOD changes. Further, my thanks go to Andrew Jackson and David Lloyd for sharing the FORTRAN code to implement the induction equation in the forward modeling scheme. Finally, I would like to thank Olivier Barrois for supplying the covariance matrix structure of the small-scale error from geodynamo calculations.

Contents

1. Introduction

Earth is surrounded by a large and complex magnetic field that changes with time. It is mostly the result of a self-sustaining dynamo acting in the liquid outer core but other sources contribute to it (Olsen et al., 2010). Fig. 1.1 sketches the different sources of the geomagnetic field, which can be broadly categorized into sources of internal and external origin.

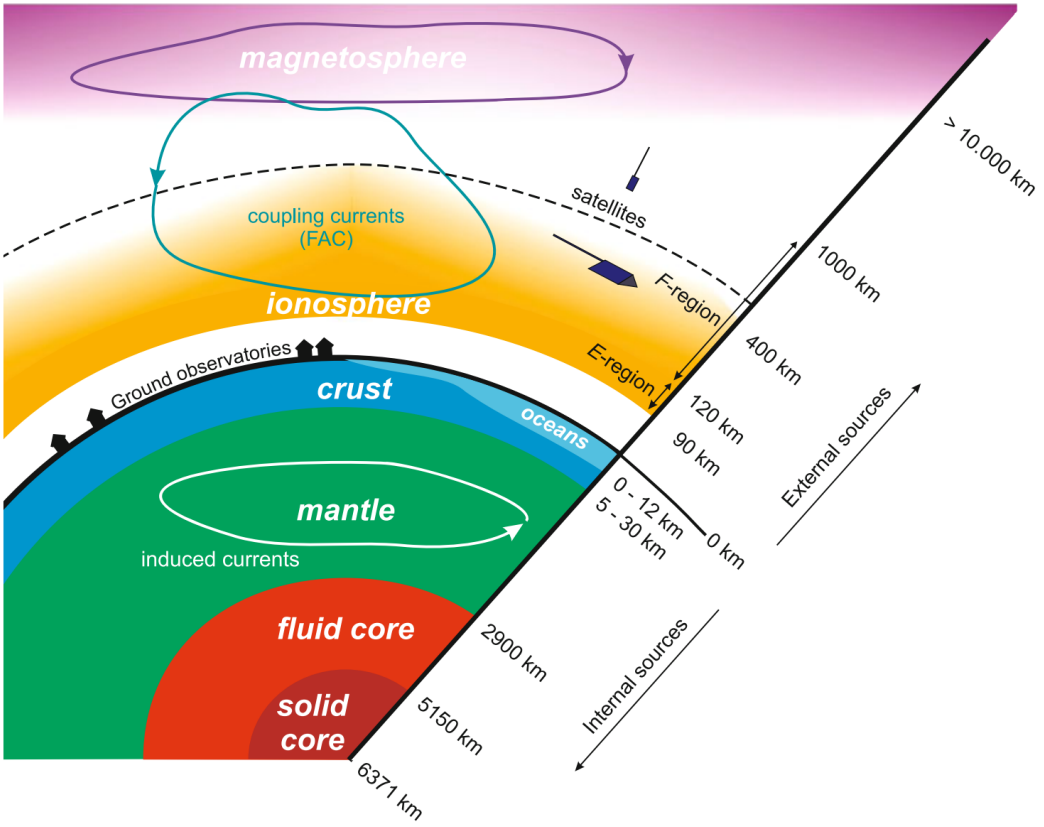

Figure 1.1. Schematic of the sources that contribute to the geomagnetic field (Figure taken from Olsen et al., 2010).

The core and the crustal, or lithospheric, field are generated by internal sources. The core field originates from currents that are maintained by the geodynamo in the liquid outer core and contributes approximately 95 % to the observed field at Earth's surface. The crustal field is caused by magnetized rocks in Earth's crust and is relatively weak. The

currents in the magnetosphere and ionosphere are external sources that also create on average relatively weak fields. Finally, there are contributions to the magnetic field due to the movement of electrically conducting seawater and externally induced currents in the crust and mantle. Although their origin is internal, they are commonly not referred to as internal sources.

Despite the variety of sources, emphasis is put on the outer core where the geodynamo is operating. The processes there, are responsible for the observed changes of the magnetic field, referred to as secular variation (SV) (Holme, 2015).

1.1. The Core Motions

The outer core consists of an electrically conducting and liquid iron-nickel alloy which undergoes vigorous convection driven by the cooling of the planet (Finlay et al., 2010). The core motion stretches, twists and advects the magnetic field into new configurations. The self-sustaining dynamo is a process by which the motions happen in such a way that electrical currents and, hence, the magnetic field are maintained against Ohmic dissipation (Olsen et al., 2010). A detailed knowledge of the core motions is therefore essential to an understanding of the observed SV.

The entire Earth, including the core, is rapidly rotating which creates a strong Coriolis force. It organizes the core motions into columnar structures that circumscribe the solid inner core. Fig. 1.2 shows a three-dimensional simulation of the core motions and in particular the azimuthal (East-West) velocity component. The cut showing a meridional plane features the columnar structures as parallel stripes of increased azimuthal flow which are aligned with the rotation axis. They are especially pronounced at cylindrical radii close to the equator.

SV observations are used as data to invert for the flow at the outer core surface, but it is a difficult inverse problem. Only the radial component of the SV can be connected to the core surface flow which leads to equations with many solutions (Holme, 2015). Even worse, there is an infinite number of them. In practice, assumptions on the structure of the flow are imposed to constrain the number of possible solutions and therefore address the issue of non-uniqueness. This is referred to as regularizing the inverse problem. In contrast, the forward problem of computing SV from a known flow can always be carried out without the problem of non-uniqueness. This study presents a new manner of implementing this forward problem by using a core flow based on the physics of motions in a rotating fluid sphere which allows a good representation of the flow at mid and low latitudes.

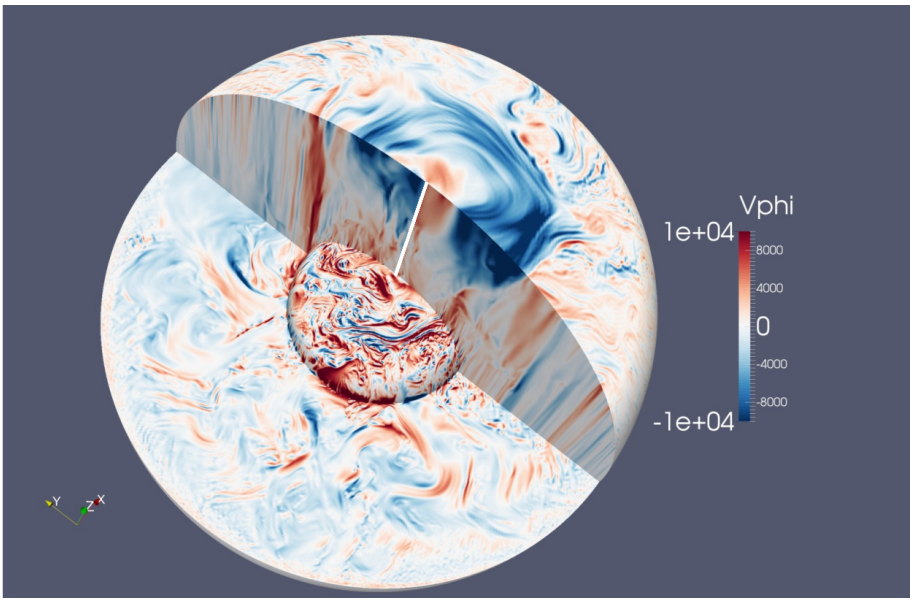

Figure 1.2. Three-dimensional geodynamo simulation of the outer core from Schaeffer et al. (2017). The smaller concentric sphere represents the solid inner core. Colors indicate the size of the azimuthal velocity component and the rotation axis is indicated by the white line.

1.2. Scientific Problem: Origin of Geomagnetic Jerks

This study aims at contributing to a better understanding of geomagnetic jerks. They are defined as abrupt changes (within one year) in the slope of the SV and separate therefore intervals where the SV varies almost linearly with time. They are also observed as events of sudden step-like change in the second time derivative of the geomagnetic field known as secular acceleration (SA) (Mandea et al., 2010). Geomagnetic jerks occur at irregular times and are observed either worldwide or regional with time shifts of up to 3 years between ground observatories (Chulliat and Maus, 2014). Although they have been studied over the past decades, the processes that cause them are still not understood. However, there is now broad consensus that they are caused by internal processes (Mandea et al., 2010). The fact that jerks are the fastest observed SV changes of internal origin makes them interesting in the context of core flow studies.

Chulliat et al. (2010) analyzed geomagnetic jerks west of Africa, which occurred around 2003 and 2007, and argued that both were caused by the same SA pulse (increased SA power on the CMB) peaking in 2006. They further suggested that the pulse should be investigated as the relevant geophysical phenomenon. Fig. 1.3 shows the Y-component (East) of the SV at the magnetic observatory MBour (MBO) at the west coast of Africa and the radial SA in 2006 on the core surface from the CHAOS-6 geomagnetic field model.

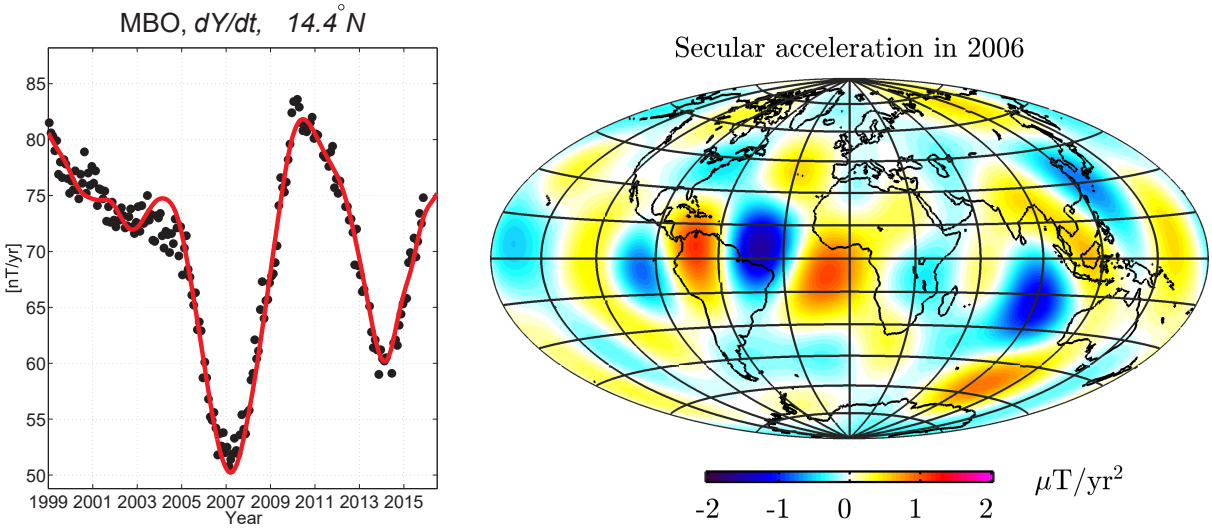

Figure 1.3. Left: observed Y-component of the SV at MBO (14.39°N, 16.96°W) are shown as black dots while the red line was calculated from the CHAOS-6 model. Right: radial secular acceleration (spherical harmonic degree 1 to 8 only) from the CHAOS-6 model in 2006.

The Y-component of the SV decreases suddenly from 70 nT/yr in 2005 to 50 nT/yr in 2007 and increases again to the previous level over a period of two years. This corresponds to the jerk in 2007 with an acceleration change of around 20 $\mathrm{nT/yr^2}$. The right side of Fig. 1.3 shows patches of increased SA, most prominent at low latitudes in the Atlantic sector in 2006 when the SA pulse was at maximum. In agreement with Gillet et al. (2015b), Finlay et al. (2016) found localized structures of non-axisymmetric azimuthal flow close to the equator using the CHAOS-6 geomagnetic model. They noted that some of them undergo time-dependent oscillations at the locations of increased SA, for example at 40°W on the equator. At this location, the modeled flow experienced a high acceleration around the time when SA pulses occurred in 2006, 2009 and also later in 2013 (Finlay et al., 2016). An important scientific question is the robustness of such oscillating azimuthal flow features and whether they can be recovered in core inversions parametrized and estimated in other ways.

1.3. Approach of this Thesis

The aim of this study will be addressed by developing a new inversion scheme based on normal modes of rotating flow in a sphere.

The primary tool of inverting for the core flow from SV observations is the induction equation. On short timescales, magnetic diffusion can be neglected and the SV is primarily considered to be generated by the advection of the magnetic field at the core surface. However, not all lengthscales of the core field can be equally well resolved from magnetic observations at Earth's surface and above, due to the crustal field. The unknown small-scale core field leads to the so-called small-scale error. The forward scheme then combines two terms, the SV produced by the flow in terms of the normal modes advecting the known large-scale core field and the SV due to the small-scale error. In the inverse scheme of this thesis, the non-uniqueness is addressed by regularizing with either a standard l_2-norm penalizing the horizontal divergence and radial vorticity of the flow, or an l_1-norm penalizing the amplitude of the normal modes.

The estimated core flow is studied with regards to length of day predictions and SA pulses which are linked to geomagnetic jerks.

1.4. Outline of the Thesis

Chapter 2 gives the theoretical background on the motion in Earth's core and the resulting induction. It further states the equations of the normal modes to represent rotating flows in a sphere. The chapter concludes with the toroidal-poloidal expansion as an often used numerical tool for representing the involved fields.

Chapter 3 presents the developed methods of this study to invert for the core flow given geomagnetic field models of the SV. This includes the implementation of the forward scheme, the toroidal-poloidal expansion and finally, the inversion scheme.

Chapter 4 summarizes the results obtained by the newly developed forward and inverse schemes. After a comparison with previous results, the chapter gives an overview of the obtained flow models and presents the time-dependence of the flow.

Chapter 5 discusses the results with regards to length of day predictions and geomagnetic jerks. It also examines the effect of the parametrization of the small-scale error term and finishes by briefly discussing the inversion scheme in a probabilistic context. Chapter 6 concludes the thesis and gives an outlook for a future study.

2. Theoretical Background

In this chapter, the equations governing the flow in Earth's core (Sec. 2.1) and the resulting magnetic induction producing changes in the core magnetic field (Sec. 2.3 and 2.4) are presented. A basis for efficiently representing flows in a rapidly rotating sphere in terms of normal modes is set out (Sec. 2.2), and numerical tools including the toroidal-poloidal expansion (Sec. 2.5), which are often used to represent the field of interest, are presented.

2.1. Flow in the Outer Core

In the following, spherical coordinates (r, θ, ϕ) with radius r, colatitude θ and azimuth ϕ are used to parametrize Earth's geometry. The mean surface radius is taken to be $r_\mathrm{s} = 6371.2\,\mathrm{km}$. The interface between the solid mantle and the core region is of major importance and called the core mantle boundary (CMB), which it is located at $r_\mathrm{c} = 3485\,\mathrm{km}$. It represents the transition of the solid mantle to the core region which is further subdivided into the outer liquid and the inner solid core. The motion of the liquid iron alloy in the outer core is assumed to be responsible for generating the main part of Earth's magnetic field.

The fluid motion in the outer core is ultimately driven by density variations due to the cooling of the planet. The description of the motion is given in terms of magnetohydrodynamics which considers the conducting fluid on macroscopic scales as a continuum. By further assuming the density to vary only slightly, one can employ the Navier-Stokes momentum equation in the Boussinesq approximation. Effects other than buoyancy are then neglected and the description is essentially that of an incompressible fluid. In the reference frame of the mantle rotating with constant angular frequency $\boldsymbol{\Omega}$, the fluid motion $\mathbf{u}$ in the outer core is described by the equations stating the conservation of mass and momentum in the Boussinesq approximation (Finlay et al., 2010)

$$\nabla \cdot \mathbf{u} = 0, \tag{2.1a}$$

$$\rho_0 \left(\frac{\partial \mathbf{u}}{\partial t} + (\mathbf{u} \cdot \nabla)\mathbf{u} + 2\boldsymbol{\Omega} \times \mathbf{u} - \nu \nabla^2 \mathbf{u} \right) = -\nabla p + \rho' \mathbf{g} + \mathbf{J} \times \mathbf{B} \tag{2.1b}$$

where ρ' is a small deviation from the constant reference density ρ_0, ν the constant kinematic viscosity, p the reduced pressure including the hydrostatic pressure and the centrifugal acceleration, $\mathbf{g}$ the acceleration due to gravity, $\mathbf{J}$ the current density and $\mathbf{B}$ the magnetic field. The nonlinear term $(\mathbf{u}\cdot\nabla)\mathbf{u}$ describes advection of angular momentum and $\nu\nabla^2\mathbf{u}$ the viscous effect while $2\boldsymbol{\Omega}\times\mathbf{u}$ is the Coriolis acceleration. Since ρ_0 is constant, the gravitational acceleration can be given as $\mathbf{g} = -\frac{g_\mathrm{c}}{r_\mathrm{c}}\mathbf{r}$ with respect to a reference acceleration g_c at the CMB with radius r_c and $\mathbf{r}$ the radial vector. The term $\mathbf{J}\times\mathbf{B}$ represents the Lorentz force and is usually re-written in terms of the magnetic field alone as

$$\mathbf{J}\times\mathbf{B} = \frac{1}{\mu_0}(\nabla\times\mathbf{B})\times\mathbf{B} = \frac{1}{\mu_0}\left((\mathbf{B}\cdot\nabla)\mathbf{B} - \frac{1}{2}\nabla B^2\right), \tag{2.2}$$

where μ_0 is the magnetic permeability and $B = |\mathbf{B}|$. The evolution of the magnetic field is described with an additional equation, called the induction equation (see Sec. 2.3). At solid boundaries such as the inner core boundary and the CMB, the viscous fluid is forced to match the motion of the boundary in such a way that no penetration or slipping can occur. Generally, the prescription of an initial velocity field completes the formulation of the problem which then consists of solving Eq. (2.1) subject to the boundary conditions.

In order to assess the relative importance of the individual terms in Eq. (2.1) and discuss possible simplifications, it is best to consider the corresponding dimensionless equation. Consider the CMB radius r_c, Earth's angular frequency Ω^{-1} and U as typical length, time and relative velocity scales of a particular motion. The governing equations in their dimensionless form with $\boldsymbol{\Omega} = \Omega\mathbf{e}_z$ and $\mathbf{e}_z$ the unit vector along the positive z-axis are then given by

$$\nabla\cdot\mathbf{u} = 0, \tag{2.3a}$$

$$\frac{\partial\mathbf{u}}{\partial t} + \epsilon(\mathbf{u}\cdot\nabla)\mathbf{u} + 2\mathbf{e}_z\times\mathbf{u} - E\nabla^2\mathbf{u} = -\nabla p + \mathbf{f}, \tag{2.3b}$$

where $\mathbf{u}$, t and p represent the dimensionless counterparts of the quantities in Eq. (2.1). The buoyancy and the Lorentz force are combined for convenience into a single dimensionless quantity, denoted $\mathbf{f}$. As a result, two dimensionless parameters E and ϵ appear (Greenspan, 1968). The Ekman number

$$E = \frac{\nu}{\Omega r_\mathrm{c}^2} \tag{2.4}$$

measures how typical viscous forces compare to the Coriolis force while the Rossby number

$$\epsilon = \frac{U}{\Omega r_\mathrm{c}} \tag{2.5}$$

gives the ratio of the convective force and the Coriolis force, and provides a measure of the relative importance of nonlinear effects. In the case of Earth, the Ekman number is

very small with $E \approx 10^{-15}$ (Finlay et al., 2010). Also, the Rossby number is expected to be very small since the typical amplitude of the fluid motion is small compared to the rotation speed.

An important consequence that illustrates how rotation affects the motion of fluids follows by considering inviscid ($E = 0$), slow ($\epsilon = 0$) and steady ($\frac{\partial \mathbf{u}}{\partial t} = 0$) conditions while neglecting $\mathbf{f}$ on the right side of Eq. (2.3). The momentum equation then reduces to

$$2\mathbf{e}_z \times \mathbf{u} = -\nabla p, \tag{2.6}$$

which expresses that the pressure force is completely balanced by the Coriolis force. This is referred to as the geostrophic balance. By taking the curl of the geostrophic balance and using the conservation of mass, the Taylor-Proudman theorem follows. It states that

$$(\mathbf{e}_z \cdot \nabla)\mathbf{u} = 0 \tag{2.7}$$

and as a consequence, the velocity field must be invariant along the rotation axis (z-axis), i.e., $\mathbf{u} = \mathbf{u}(x, y)$. Since particles on a vertical line move identically, the flow can be considered as comprised of vertically elongated or columnar fluid cells. The fluid columns move as if rigid along the rotation axis and must therefore maintain a constant height. Although the stated assumptions are quite restrictive, it has been found that broadly columnar structures are relevant in short timescale core dynamics. Strongly columnar dynamic regimes have been observed in a number of both experimental and numerical simulations dealing with thermally driven convection, and including the impact of the magnetic field and the backreaction of the convective flow (see Pais and Jault, 2008 for a review). Also, Jault (2008) suggests that rotation dominates in Earth's core for timescales small compared to magnetic diffusion. Hence, a plausible conclusion is that the presence of buoyancy and Lorentz force leads to relatively small departures from the exact geostrophic balance. This allows approximately z-invariant or broadly columnar flows within the whole core region which are referred to as being quasi-geostrophic (QG).

There are different approaches to modeling QG dynamics (e.g. Pais and Jault, 2008). In this study, the QG flow is represented by a subset of QG modes that arise in rotating homogeneous fluid spheres. Use of the complete set of modes allows more general flows beyond the QG assumption offering an alternative means of representing core motions. The equations and analytical expressions for the normal modes of flow in a rapidly rotating fluid sphere are given in the following section.

2.2. Flow in a Rotating Fluid Sphere

Consider a rapidly rotating spherical shell of unit radius, representing the CMB, completely filled with an incompressible and viscous core fluid. In this study, the effect of the inner core is completely ignored and the focus is on motions at cylindrical radius outside the inner core. The fluid motion is assumed to be close to rigid rotation i.e., the motions deviate only slightly from solid body rotation ($\mathbf{u} = 0$ in the rotating reference frame). Consequently, the typical velocity magnitude is small compared to the rotation speed and $\epsilon \ll 1$. The nonlinear term in the momentum equation can then be neglected to a first approximation. In addition, the Ekman number is considered to be small and the corresponding viscous dissipation weak so that a small external force is sufficient to sustain the fluid motion. The effect of viscosity is mainly confined to a thin boundary layer at the CMB. Hence, the interior of the fluid is practically inviscid and a leading order solution neglecting the viscous correction at the boundary can be found. Importantly, the solution of the leading order problem is sufficient to connect the observed magnetic field with the core flow (further details in Sec. 2.4).

The inviscid flow $\mathbf{u}$ of the leading order problem in the co-rotating reference frame then satisfies the dimensionless equations (Zhang et al., 2001)

$$\nabla \cdot \mathbf{u} = 0, \tag{2.8a}$$

$$\frac{\partial \mathbf{u}}{\partial t} + 2\mathbf{e}_z \times \mathbf{u} = -\nabla p, \tag{2.8b}$$

subject to the boundary condition of an impenetrable CMB

$$\mathbf{e}_r \cdot \mathbf{u} = 0, \quad \text{at} \quad r = 1. \tag{2.9}$$

Here p is also the leading order approximation of the pressure. The leading order problem of inviscid interior motion can be given as a superposition of two types of modes, namely a single geostrophic mode corresponding to a steady-state flow, and an infinite number of inertial modes. Ivers et al. (2015) show that the modes are mutually orthogonal over the volume of the sphere provided their frequencies are different. They further establish the completeness of the modes in a sphere.

2.2.1. Geostrophic Mode

The geostrophic mode represents the steady-state flow of an incompressible and sufficiently slow fluid of negligible viscosity. The equation of motion is identical to the Taylor-Proudman theorem in Eq. (2.7) subject to the boundary condition in Eq. (2.9). The

solutions can be given in the form of a zonal, i.e. axisymmetric, azimuthal flow (Liao and Zhang, 2010a)

$$\mathbf{u} = u_\phi(r\sin\theta)\mathbf{e}_\phi. \tag{2.10}$$

The Taylor-Proudman theorem indicates it is simplest to use cylindrical coordinates for the rotating flow while spherical coordinates are more appropriate to account for the boundary condition. Liao and Zhang (2010a) suggest the existence of a polynomial G_{2k-1} with integer k that resolves the conflict between the geometry of the flow and the boundary. They derived a second-order ordinary differential equation in $s = r\sin\theta$

$$(1-s^2)G''_{2k-1}(s) + \frac{1-4s^2}{s}G'_{2k-1}(s) - \left(2+\frac{1}{s}\right)G_{2k-1}(s) = -2k(2k+1)G_{2k-1}(s) \tag{2.11}$$

with $k = 1, 2, 3...$ and $'$ denoting the derivative with respect to s. The solution is a polynomial of order $(2k-1)$ with

$$G_{2k-1} = \sum_{j=1}^{k} \frac{(-1)^{k-j}[2(k+j)-1]!!}{2^{k-1}(k-j)!(j-1)!(2j)!!}(r\sin\theta)^{2j-1}. \tag{2.12}$$

This so-called "geostrophic" polynomial is orthogonal over the sphere (Liao and Zhang, 2010a)

$$\int_0^{2\pi}\int_0^{\pi}\int_0^1 G_{2k-1}(r\sin\theta)G_{2n-1}(r\sin\theta)r^2\sin\theta\mathrm{d}r\mathrm{d}\theta\mathrm{d}\phi = 0, \quad n \neq k \tag{2.13}$$

and can be normalized with

$$\frac{3}{4\pi}\int_0^{2\pi}\int_0^{\pi}\int_0^1 [G_{2k-1}(r\sin\theta)]^2 r^2\sin\theta\mathrm{d}r\mathrm{d}\theta\mathrm{d}\phi = \frac{3(2k+1)!!(2k-1)!!}{(4k+1)(2k)!!(2k-2)!!}. \tag{2.14}$$

The combination of a geostrophic polynomial G_{2k-1} with the azimuthal unit vector will be referred to as the geostrophic mode of wavenumber k. The geostrophic flow, which is a zonal flow, is then given as a linear combination of the geostrophic modes for all integer k

$$\mathbf{u} = \sum_k a_k G_{2k-1}(r\sin\theta)\mathbf{e}_\phi. \tag{2.15}$$

Fig. 2.1 shows three examples of the geostrophic modes with $k = 2, 4, 6$ in the meridional plane and on the CMB.

2.2.2. Inertial Modes

Aside from the steady geostrophic flow, there is a time-dependent flow that is a superposition of an infinite number of non-axisymmetric modes, called inertial modes. The inertial modes are described by the full leading order problem in Eq. (2.8) and the boundary

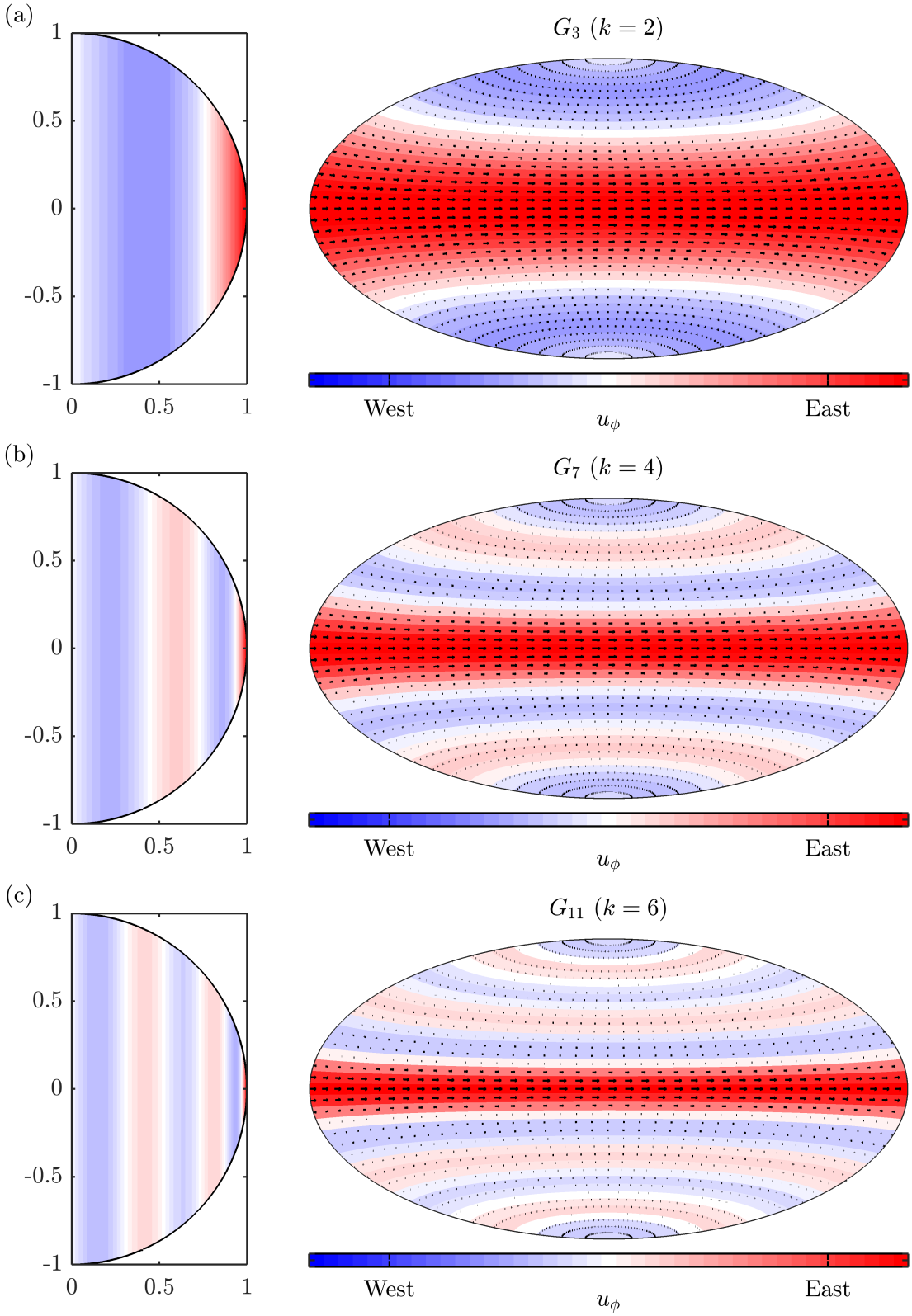

Figure 2.1. Three examples of the geostrophic modes with (a) $k = 2$, (b) $k = 4$ and (c) $k = 6$ in the meridional plane (left) and on the CMB (right). The color indicates the direction and strength of the azimuthal flow.

condition (2.9). Following Liao and Zhang (2010b), the modes can be given in terms of three velocity components in spherical coordinates as

$$\mathbf{u} = [u_r(r,\theta,\phi), u_\theta(r,\theta,\phi), u_\phi(r,\theta,\phi)]\mathrm{e}^{2\mathrm{i}\sigma t}, \tag{2.16}$$

where i is the imaginary unit and $\sigma = \frac{\omega}{2}$ the half-frequency. Further, the modes can be divided into two classes according to their symmetry with respect to the equatorial plane. There are the equatorially symmetric modes satisfying

$$\big(u_r, u_\theta, u_\phi\big)(r,\theta,\phi) = \big(u_r, -u_\theta, u_\phi\big)(r,\pi-\theta,\phi), \tag{2.17}$$

and the equatorially antisymmetric modes, having

$$\big(u_r, u_\theta, u_\phi\big)(r,\theta,\phi) = \big(-u_r, u_\theta, -u_\phi\big)(r,\pi-\theta,\phi). \tag{2.18}$$

In the explicit solution presented by Liao and Zhang (2010b), the spatial complexity of the inertial modes is controlled by two wavenumbers, N and M. The first parameter determines the structure in the meridional plane while the second one controls the sinusoidal structure in azimuth. Explicit expressions of the symmetric and antisymmetric inertial modes are given below.

Symmetric and Quasi-Geostrophic Modes

The half-frequency, σ, of the symmetric inertial modes are the roots of the polynomial (Liao and Zhang, 2010b)

$$0 = \sum_{j=0}^{N}(-1)^j \frac{[2(2N+M-j)]!}{j!(2N+M-j)![2(N-j)]!}\left[(M+2N-2j) - \frac{2(N-j)}{\sigma}\right]\sigma^{2(N-j)} \tag{2.19}$$

for which $N = 1,2,3,...$ and $M = 1,2,3,...$. For a given pair N and M, there are $2N$ symmetric inertial modes corresponding to the $2N$ roots of Eq. (2.19). Their three components in spherical coordinates are given by (Zhang et al., 2001)

$$\begin{aligned} u_r = -\mathrm{i}\sum_{i=0}^{N}\sum_{j=0}^{N-i} & C_{ij;NM} r^{M+2(i+j)-1} \sin^{M+2j}\theta \cos^{2i}\theta \mathrm{e}^{\mathrm{i}M\phi} \\ & \cdot \sigma^{2i-1}(1-\sigma^2)^{j-1}[\sigma(M+M\sigma+2j\sigma) - 2i(1-\sigma^2)] \end{aligned} \tag{2.20a}$$

$$\begin{aligned} u_\theta = -\mathrm{i}\sum_{i=0}^{N}\sum_{j=0}^{N-i} & C_{ij;NM} r^{M+2(i+j)-1} \sin^{M+2j-1}\theta \cos^{2i-1}\theta \mathrm{e}^{\mathrm{i}M\phi} \\ & \cdot \sigma^{2i-1}(1-\sigma^2)^{j-1}[\sigma(M+M\sigma+2j\sigma)\cos^2\theta + 2i(1-\sigma^2)\sin^2\theta] \end{aligned} \tag{2.20b}$$

$$\begin{aligned} u_\phi = \sum_{i=0}^{N}\sum_{j=0}^{N-i} & C_{ij;NM} r^{M+2(i+j)-1} \sin^{M+2j-1}\theta \cos^{2i}\theta \mathrm{e}^{\mathrm{i}M\phi} \\ & \cdot \sigma^{2i}(1-\sigma^2)^{j-1}(M+M\sigma+2j), \end{aligned} \tag{2.20c}$$

where the coefficients $C_{ij;NM}$ are defined as

$$C_{ij;NM} = \frac{(-1)^{i+j}[2(N+M+i+j)-1]!!}{2^{j+1}(2i-1)!!(N-i-j)!i!j!(M+j)!}. \tag{2.21}$$

It can be shown that $u_r(r=1)=0$, hence satisfying the required boundary condition in Eq. (2.9). Also, a normalization of the modes with (Liao and Zhang, 2010b)

$$\begin{aligned}
&\frac{3}{4\pi}\int_0^{2\pi}\int_0^{\pi}\int_0^1 |\mathbf{u}|^2 r^2 \sin\theta \mathrm{d}r\mathrm{d}\theta\mathrm{d}\phi = \\
&\sum_{i=0}^{N}\sum_{j=0}^{N-i}\sum_{k=0}^{N}\sum_{l=0}^{N-k} C_{ij;NM}C_{kl;NM}\frac{3[2(M+j+l-1)]!!}{[2(M+i+j+k+l)+1]!!}\sigma^{2(i+k)}(1-\sigma^2)^{j+l} \\
&\cdot\Bigg([(M+M\sigma+2j)(M+M\sigma+2l)+(M+M\sigma+2j\sigma)(M+M\sigma+2l\sigma)] \\
&\cdot\frac{[2(i+k)-1]!!}{(1-\sigma^2)^2}+8ik(M+j+l)\frac{[2(i+k)-3]!!}{\sigma^2}\Bigg)
\end{aligned} \tag{2.22}$$

can be established. Zhang et al. (2001) found a special subclass that is almost z-invariant and characterized by a small frequency. Hence, when rearranging the absolute values of the $2N$ frequencies in an ascending order

$$|\sigma_1 = \sigma_{\mathrm{QG}}| < |\sigma_2| < ... < |\sigma_{2N}|\,,$$

the smallest frequency can be identified as the QG mode of frequency σ_{QG} that is characterized by flows nearly invariant to the rotation axis (Fig. 2.2a and 2.3e, f). For sufficiently small σ_{QG}, the frequency can be approximated with (Zhang et al., 2001)

$$\omega_{\mathrm{QG}} = 2\sigma_{\mathrm{QG}} \approx -\frac{2}{M+2}\left[\sqrt{1+\frac{M(M+2)}{N(2N+2M+1)}}-1\right]. \tag{2.23}$$

Fig. 2.2 and 2.3 show examples of symmetric inertial modes with the slowest being QG modes.

Antisymmetric Modes

The half-frequency of equatorially antisymmetric inertial modes satisfy (Zhang et al., 2001)

$$\begin{aligned}
0 = \sum_{j=0}^{N}(-1)^j &\frac{[2(2N+M-j+1)]!}{j!(2N+M-j+1)![2(N-j)+1]!} \\
&\cdot\left[(M+2N-2j+1)-\frac{2(N-j)+1}{\sigma}\right]\sigma^{2(N-j)+1}
\end{aligned} \tag{2.24}$$

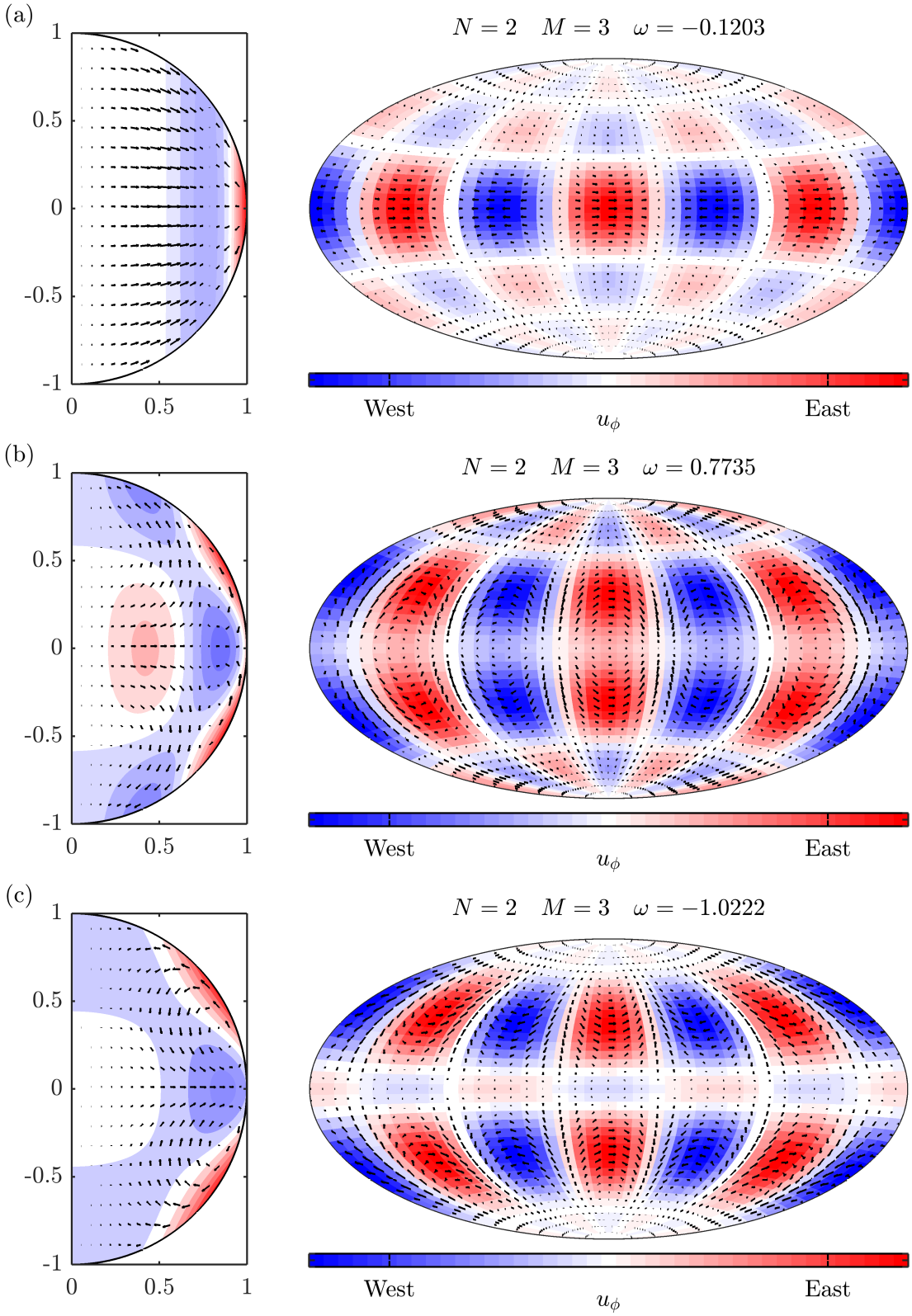

Figure 2.2. The first three symmetric inertial modes of the four possible modes having the wavenumbers $N = 2$ and $M = 3$. The slowest mode of this selection in (a) is an example of a QG mode.

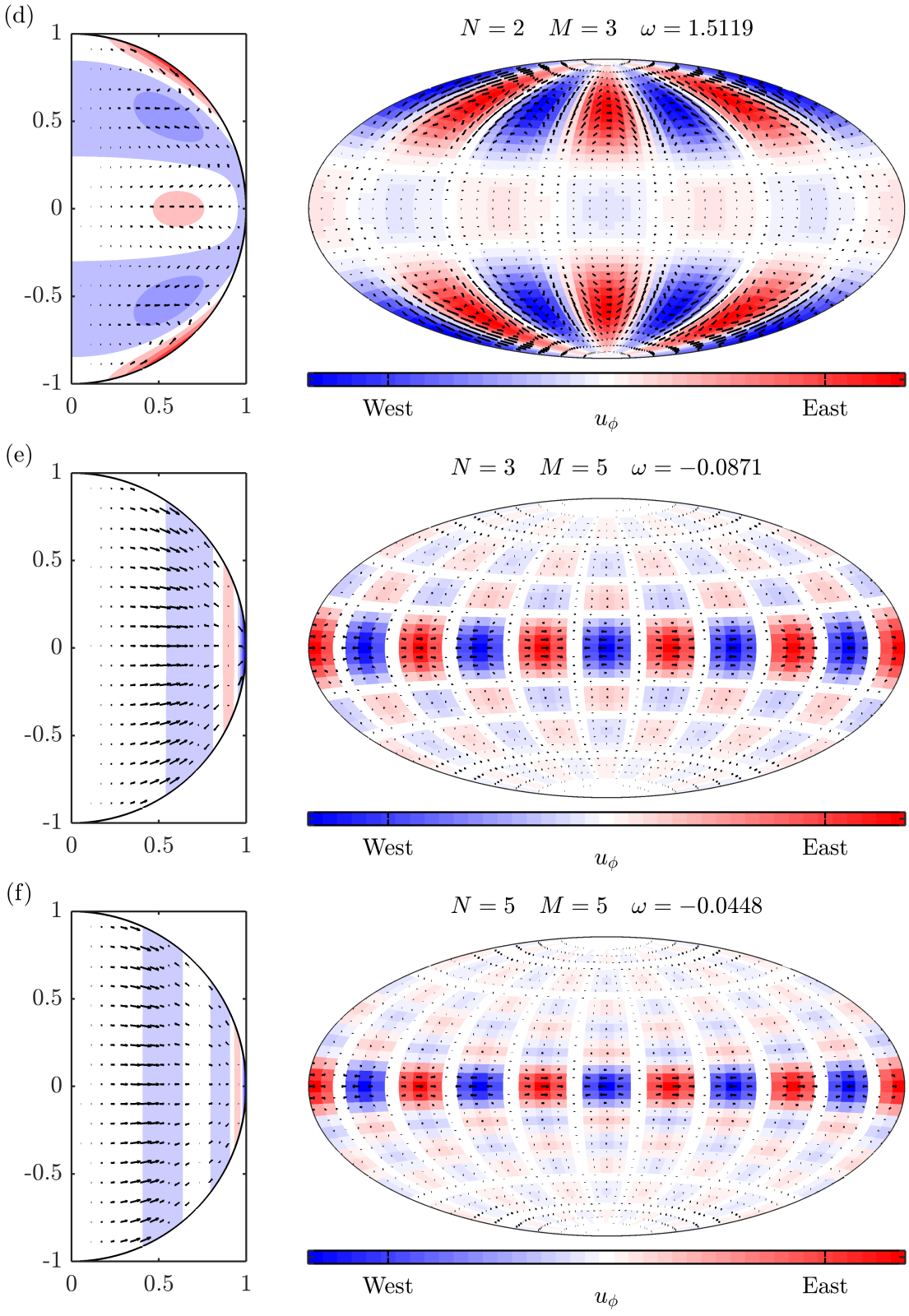

Figure 2.3. The fastest symmetrical inertial mode having $N = 2$ and $M = 3$ is shown in (d). (e) and (f) give examples of other QG modes.

where $N = 0, 1, 2, ...$ and $M = 1, 2, 3, ...$. The polynomial has $2N + 1$ roots, each representing the frequency of an antisymmetric inertial mode for a given N and M. The three velocity components in spherical coordinates are (Zhang et al., 2001)

$$u_r = -\mathrm{i}\sum_{i=0}^{N}\sum_{j=0}^{N-i} C_{ij;NM} r^{M+2(i+j)} \sin^{M+2j}\theta \cos^{2i+1}\theta \mathrm{e}^{\mathrm{i}M\phi} \cdot \sigma^{2i-1}(1-\sigma^2)^{j-1}[\sigma(M + M\sigma + 2j\sigma) - (2i+1)(1-\sigma^2)] \tag{2.25a}$$

$$u_\theta = -\mathrm{i}\sum_{i=0}^{N}\sum_{j=0}^{N-i} C_{ij;NM} r^{M+2(i+j)} \sin^{M+2j-1}\theta \cos^{2i}\theta \mathrm{e}^{\mathrm{i}M\phi}\sigma^{2i-1}(1-\sigma^2)^{j-1} \cdot [\sigma(M + M\sigma + 2j\sigma)\cos^2\theta + (2i+1)(1-\sigma^2)\sin^2\theta] \tag{2.25b}$$

$$u_\phi = \sum_{i=0}^{N}\sum_{j=0}^{N-i} C_{ij;NM} r^{M+2(i+j)} \sin^{M+2j-1}\theta \cos^{2i+1}\theta \mathrm{e}^{\mathrm{i}M\phi} \cdot \sigma^{2i}(1-\sigma^2)^{j-1}(M + M\sigma + 2j), \tag{2.25c}$$

where the coefficients $C_{ij;NM}$ are defined as

$$C_{ij;NM} = \frac{(-1)^{i+j}[2(N+M+i+j)+1]!!}{2^{j+1}(2i+1)!!(N-i-j)!i!j!(M+j)!}. \tag{2.26}$$

Again, the boundary condition $u_r(r = 1) = 0$ is satisfied and a normalization similar to the one given in Liao and Zhang (2010b) for the symmetric inertial modes could be derived as

$$\begin{aligned}&\frac{3}{4\pi}\int_0^{2\pi}\int_0^{\pi}\int_0^{1} |\mathbf{u}|^2 r^2 \sin\theta \mathrm{d}r\mathrm{d}\theta\mathrm{d}\phi = \\ &\sum_{i=0}^{N}\sum_{j=0}^{N-i}\sum_{k=0}^{N}\sum_{l=0}^{N-k} C_{ij;NM}C_{kl;NM}\frac{3[2(M+j+l-1)]!!}{[2(M+i+j+k+l)+3]!!}\sigma^{2(i+k)}(1-\sigma^2)^{j+l} \\ &\cdot\Bigg([(M+M\sigma+2j)(M+M\sigma+2l)+(M+M\sigma+2j\sigma)(M+M\sigma+2l\sigma)] \\ &\cdot\frac{[2(i+k)+1]!!}{(1-\sigma^2)^2} + 2(2i+1)(2k+1)(M+j+l)\frac{[2(i+k)-1]!!}{\sigma^2}\Bigg).\end{aligned} \tag{2.27}$$

Fig. 2.4 shows three of the five possible antisymmetric inertial modes having $N = 2$ and $M = 3$.

2.3. Induction Equation and Secular Variation

The magnetic field within Earth's core is changed by the motion of the electrically conducting core fluid. Consider Ohm's law of a conductor submerged in the magnetic field $\mathbf{B}$ and the electric field $\mathbf{E}$ while moving with velocity $\mathbf{u}$

$$\mathbf{J} = \sigma(\mathbf{E} + \mathbf{u} \times \mathbf{B}),$$

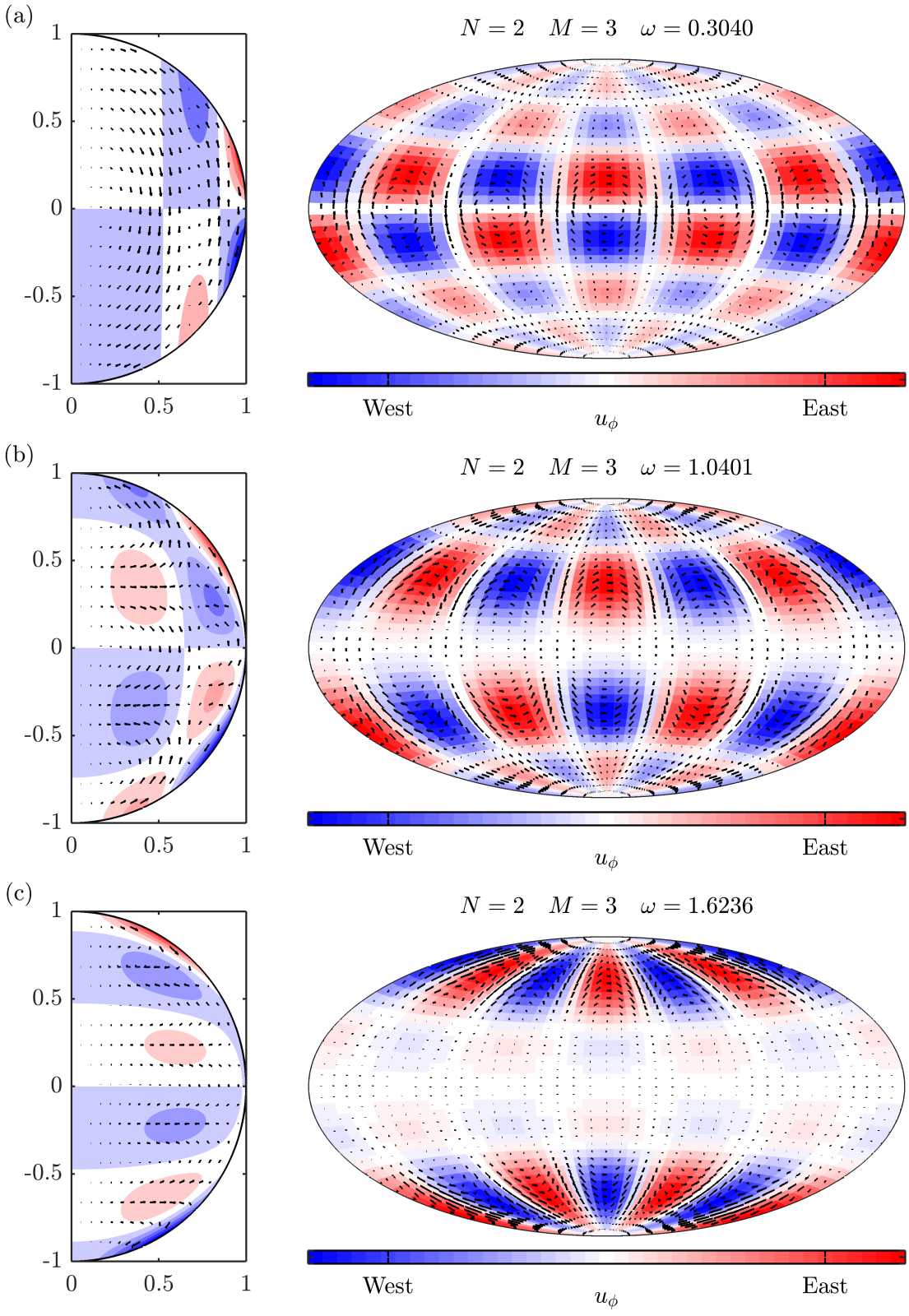

Figure 2.4. The slowest (a), an intermediate (b) and the fastest mode (c) of antisymmetric inertial modes sharing the same wavenumbers $N = 2$ and $M = 3$.

where σ denotes here a constant electrical conductivity. By taking the curl of Ohm's law and using Faraday's and Ampere's law

$$\nabla \times \mathbf{E} = -\frac{\partial \mathbf{B}}{\partial t}$$
$$\nabla \times \mathbf{B} = \mu_0 \mathbf{J}$$

for slowly varying fields, one can replace the current density and the electric field with expressions in terms of the magnetic field

$$\nabla \times \mathbf{J} = \frac{1}{\mu_0} \nabla \times (\nabla \times \mathbf{B}) = \sigma \left(-\frac{\partial \mathbf{B}}{\partial t} + \nabla \times (\mathbf{u} \times \mathbf{B}) \right).$$

Rearranging the second equality and using the identity $\nabla \times (\nabla \times \mathbf{B}) = \nabla(\nabla \cdot \mathbf{B}) - \nabla^2 \mathbf{B}$ with $\nabla \cdot \mathbf{B} = 0$ yields the induction equation which describes the evolution of the magnetic field in the presence of a moving conductor

$$\frac{\partial \mathbf{B}}{\partial t} = \nabla \times (\mathbf{u} \times \mathbf{B}) + \eta \nabla^2 \mathbf{B}, \tag{2.28}$$

where $\eta = \frac{1}{\mu_0 \sigma}$ denotes the magnetic diffusivity. The first term on the right side represents the effect of magneto-advection while the second one is connected to magnetic diffusion. Hence, there are two mechanisms responsible for changing the magnetic field with time.

The change of the geomagnetic field on timescales of years to decades is commonly referred to as secular variation (SV). The characteristic timescale associated with diffusion can be estimated with the help of assumed to be appropriate values for the core diffusivity $\eta = 1.69 \, \frac{\mathrm{m}^2}{\mathrm{s}}$ and the length $L = 1000 \, \mathrm{km}$ for magnetic field structures. Then, the diffusion time follows as $L^2/\eta \approx 19\,000 \, \mathrm{yrs}$ (Finlay et al., 2010) and is long compared to the timescale of the observed SV. Going further and carrying out a scale analysis of the induction equation (2.28) yields an estimate of the relative importance of magneto-advection and magnetic diffusion. The magnetic Reynolds number

$$R_\mathrm{m} = \frac{|\nabla \times (\mathbf{u} \times \mathbf{B})|}{|\eta \nabla^2 \mathbf{B}|} \approx \frac{UL}{\eta}$$

with U a typical velocity scale follows. Taking L and η as before, and assuming $U = 16 \, \mathrm{km/yr}$ results in $R_\mathrm{m} \approx 300$ (Finlay et al., 2010), which is much bigger than one. The analysis suggests that magnetic diffusion in the bulk of the core is negligible compared to advection and small on short timescales for characteristic lengthscales of the field. Neglecting magnetic diffusion in the induction equation (2.28) is known as the frozen-flux approximation. The name refers to the fact that under this approximation magnetic flux patches are carried along with the flow and appear as if they are frozen to it.

2.4. Flow Inversion and Non-Uniqueness

Since the core region is not directly accessible to measurements, inferences of the core motions and dynamics rely on magnetic field measurements at Earth's surface and above. The key is to connect the observations and the core flow given the equations governing the physics in the core region. Of great importance here is the region just below the CMB.

By assuming an electrically insulating mantle, one can downward-continue magnetic field models based on surface measurements via potential theory until the CMB. Aside from a very thin viscous boundary layer that ensures no-slip of the core fluid, there exists a magnetic boundary layer. It arises from the fact that the conductivity jumps when going from the insulating mantle to the conducting core region. The flow at the CMB is zero and, hence, inverting for the flow at the core surface actually refers to the flow at the top of the free stream, just below the viscous and magnetic boundary layers.

Only the radial component of the magnetic field can be safely continued through the viscous and magnetic boundary layer given the characteristic timescale of the SV and length of the large-scale field. Together with the expected high magnetic Reynolds numbers and very long diffusion times, it can be concluded that the frozen-flux approximation holds for the radial part on short timescales (Finlay et al., 2010). Also, the Lorentz forces associated with the field in the magnetic boundary layer are negligible and do not affect the fluid dynamics (Jault and Le Mouël, 1991). Therefore and since the flow on top of the free stream is by definition just below the boundary layers, the horizontal components are those of a rapidly rotating inviscid fluid while the radial flow component is zero as if being directly at the CMB. This justified for only considering the leading-order problem of a rotating fluid sphere here.

The radial component of the induction equation in the frozen flux approximation at the core surface, where $u_r(r=1)=0$ and using $\nabla \cdot \mathbf{u} = 0$, simplifies to

$$\frac{\partial B_r}{\partial t} = -\nabla_{\mathrm{H}} \cdot (\mathbf{u} B_r)\,, \tag{2.29}$$

where $\nabla_{\mathrm{H}} \equiv \nabla - \vec{e}_r \frac{\partial}{\partial r}$ is the horizontal part of the gradient. The induction equation is the primary tool that enables SV observations to be used to infer the flow at the core surface.

Unfortunately, it is not enough to completely constrain the flow as can be seen from a simple argument. Although the radial flow component is assumed to be zero, there remain two horizontal components as unknowns but only one equation to solve for them. Backus (1968) examined what can be learned about the flow at the core surface provided that the

frozen-flux approximation holds and both the magnetic field and SV are known. It turns out that only flow components perpendicular to the null-flux curves (lines of $B_r = 0$) can be determined and even worse, one flow satisfying Eq. (2.29) implies infinitely many. The non-uniqueness needs to be reduced by additional assumptions on the dynamics of the flow. For example in this study, the core flow is represented by geostrophic and inertial modes, and in particular, the subclass of quasi-geostrophic modes. In addition, other constraints are applied to the flow for example by requiring it to be large-scale or as simple as possible (e.g. Bloxham and Jackson, 1991; Holme, 2015).

2.5. Toroidal-Poloidal Expansion of Incompressible Flows

Divergence-free vector fields in spherical geometry can be conveniently represented in terms of their toroidal-poloidal expansion. Both the magnetic field and the core flow can be expanded in such a way. In case of the core flow, it may be rewritten as (Sabaka et al., 2010)

$$\begin{aligned} \mathbf{u} &= \nabla \times (T\mathbf{r}) + \nabla \times \nabla \times (P\mathbf{r}) \\ &= \mathbf{u}_{\text{tor}} + \mathbf{u}_{\text{pol}}, \end{aligned} \tag{2.30}$$

introducing the toroidal and poloidal scalar potentials $T(r, \theta, \phi)$ and $P(r, \theta, \phi)$. Hence, the first term on the right side represents the toroidal part while the second one gives the poloidal part of the original vector field. The potentials can then further be expanded into a basis of Schmidt quasi-normalized spherical harmonics $Y_n^{m(c,s)}(\theta, \phi)$ of degree n and order m

$$\begin{aligned} T(r,\theta,\phi) &= \sum_{n=1}^{\infty}\sum_{m=0}^{n} \left(t_n^{mc}(r) Y_n^{mc}(\theta,\phi) + t_n^{ms}(r) Y_n^{ms}(\theta,\phi)\right) \\ P(r,\theta,\phi) &= \sum_{n=1}^{\infty}\sum_{m=0}^{n} \left(p_n^{mc}(r) Y_n^{mc}(\theta,\phi) + p_n^{ms}(r) Y_n^{ms}(\theta,\phi)\right), \end{aligned} \tag{2.31}$$

where $n = 0$ was omitted, since it is a divergence-free vector field. The spherical harmonics are defined as

$$Y_n^{m(c,s)} = \begin{cases} Y_n^{mc} \equiv P_n^m(\cos\theta)\cos m\phi \\ Y_n^{ms} \equiv P_n^m(\cos\theta)\sin m\phi \end{cases} \tag{2.32}$$

using associated Legendre function $P(x = \cos\theta)$ normalized to

$$\begin{aligned} P_n^m(x) &= \begin{cases} P_{n,m}(x), & \text{for } m = 0 \\ \sqrt{\frac{2(n-m)!}{(n+m)!}} P_{n,m}(x), & \text{for } m \neq 0 \end{cases} \\ P_{n,m}(x) &= \frac{1}{2^n n!}(1-x^2)^{\frac{m}{2}} \frac{\mathrm{d}^{n+m}}{\mathrm{d}x^{n+m}}(x^2-1)^n,\ m \leq n, \end{aligned}$$

and satisfying the orthogonality relations

$$\begin{aligned} \langle Y_n^{mc}, Y_l^{kc} \rangle &\equiv \frac{1}{4\pi} \int_0^{\pi} \int_0^{2\pi} Y_n^{mc} Y_l^{kc} \sin\theta \mathrm{d}\theta \mathrm{d}\phi = \frac{1+\delta_{m0}}{2n+1} \delta_{nl} \delta_{mk}, \\ \langle Y_n^{ms}, Y_l^{ks} \rangle &= \frac{1+\delta_{m0}}{2n+1} \delta_{nl} \delta_{mk} \qquad \text{and} \qquad \langle Y_n^{mc}, Y_l^{ks} \rangle = 0, \end{aligned} \tag{2.33}$$

where δ_{nl} is the Kronecker-delta. Inserting the expressions above into Eq. (2.30) and evaluating the vector operations yields (Sabaka et al., 2010)

$$\mathbf{u}_{\mathrm{tor}}(r,\theta,\phi) = \sum_{n=1}^{\infty} \sum_{m=0}^{n} \left(t_n^{mc}(r) \mathbf{T}_n^{mc}(\theta,\phi) + t_n^{ms}(r) \mathbf{T}_n^{ms}(\theta,\phi) \right) \tag{2.34a}$$

$$\begin{aligned} \mathbf{u}_{\mathrm{pol}}(r,\theta,\phi) = &\sum_{n=1}^{\infty} \sum_{m=0}^{n} n(n+1) \left(p_n^{mc}(r) \mathbf{P}_n^{mc}(\theta,\phi) + p_n^{ms}(r) \mathbf{P}_n^{ms}(\theta,\phi) \right) \\ &+ \sum_{n=1}^{\infty} \sum_{m=0}^{n} \left(s_n^{mc}(r) \mathbf{S}_n^{mc}(\theta,\phi) + s_n^{ms}(r) \mathbf{S}_n^{ms}(\theta,\phi) \right), \end{aligned} \tag{2.34b}$$

introducing vector spherical harmonics $\mathbf{T}_n^{m(c,s)}$, $\mathbf{P}_n^{m(c,s)}$ and $\mathbf{S}_n^{m(c,s)}$. Note that $s_n^{m(c,s)} = \frac{\mathrm{d}}{\mathrm{d}r}\left(r p_n^{m(c,s)} \right)$. The vector spherical harmonics are given by (Sabaka et al., 2010)

$$\begin{aligned} \mathbf{P}_n^{m(c,s)} &\equiv Y_n^{m(c,s)} \mathbf{e}_r \\ &= P_{n,r}^{m(c,s)} \mathbf{e}_r \end{aligned} \tag{2.35a}$$

$$\begin{aligned} \mathbf{S}_n^{m(c,s)} &\equiv r \nabla_{\mathrm{H}} Y_n^{m(c,s)} = \frac{\partial Y_n^{m(c,s)}}{\partial \theta} \mathbf{e}_\theta + \frac{1}{\sin\theta} \frac{\partial Y_n^{m(c,s)}}{\partial \phi} \mathbf{e}_\phi \\ &= S_{n,\theta}^{m(c,s)} \mathbf{e}_\theta + S_{n,\phi}^{m(c,s)} \mathbf{e}_\phi \end{aligned} \tag{2.35b}$$

$$\begin{aligned} \mathbf{T}_n^{m(c,s)} &\equiv \nabla \times \left(Y_n^{m(c,s)} \mathbf{e}_r \right) = \frac{1}{\sin\theta} \frac{\partial Y_n^{m(c,s)}}{\partial \phi} \mathbf{e}_\theta - \frac{\partial Y_n^{m(c,s)}}{\partial \theta} \mathbf{e}_\phi \\ &= T_{n,\theta}^{m(c,s)} \mathbf{e}_\theta + T_{n,\phi}^{m(c,s)} \mathbf{e}_\phi. \end{aligned} \tag{2.35c}$$

In general, the radial dependence of the decomposition in Eq. (2.34) involves expressions of Bessel functions of the first and second kind. However, for vector fields given on a spherical surface alone, it is sufficient to know $t_n^{m(c,s)}$, $p_n^{m(c,s)}$ and $s_n^{m(c,s)}$ evaluated at the radius of the sphere. The three resulting sets of coefficients are then considered the toroidal-poloidal expansion coefficients on the relevant sphere. Note also that a vector field without a radial component requires the $p_n^{m(c,s)}$ to completely disappear. In this case, the coefficients $t_n^{m(c,s)}(r)$ and $s_n^{m(c,s)}(r)$ are sufficient to fully represent the vector field, for example the flow at the core surface.

In this study, the toroidal-poloidal expansion is used to expand geostrophic and inertial modes that have been chosen to represent the flow at the core surface into their respective toroidal and poloidal coefficients. In this form, they can be implemented in the inversion scheme.

3. Methods

This chapter presents the methods that have been developed in this study to infer the core flow given field models of the observed SV. In a first part, the input data and geomagnetic field models are introduced (Sec. 3.1). Next, a detailed account of the new scheme for modeling is given (Sec. 3.2). Finally, the relatively simple approach of this study to inversion is outlined (Sec. 3.3).

3.1. Input Data: Time-dependent Geomagnetic Field Models

In this study, the geomagnetic field model CHAOS-6-x2 (extension of CHAOS-6 using ground and satellite data up to November 2016) is used. It is the latest in a series of models providing high resolution information on the time variation of the core-generated part of Earth's magnetic field between 1999.0 and 2016.5 (see Finlay et al. (2016) for a detailed presentation and account of its construction). Though mostly derived from magnetic satellite data, ground observatory monthly means were also used. In particular, CHAOS-6-x2 relies on ground-observatory data of 160 observatories up to November 2016 and satellite data of the Ørsted, CHAMP and SAC-C missions as well as *Swarm* up to December 2016. The *Swarm* mission, launched on 22 November 2013, with its three satellites *Alpha*, *Bravo* and *Charlie* in low-Earth-orbit represent a new opportunity for studying SV as they provide valuable constraints on time-varying SV with global coverage.

For core flow computations, only the core field within Earth's core is relevant. It is partly obscured by the crustal field but dominates the internal field at large length-scales (spherical harmonic degrees less than 14). The time-dependent internal field $\mathbf{B}(t) = -\nabla V(t)$ in CHAOS-6 is represented as the gradient of the scalar potential $V(t)$ which is decomposed into real-valued spherical harmonics (Finlay et al., 2016). In general,

the decomposition involves an infinite series of the form

$$V(t) = r_\mathrm{s} \sum_{n=1}^{\infty} \sum_{m=0}^{n} \left(\frac{r_\mathrm{s}}{r}\right)^{n+1} (g_n^m(t) Y_n^{mc} + h_n^m(t) Y_n^{ms}), \tag{3.1}$$

with $r_\mathrm{s} = 6371.2\,\mathrm{km}$ the reference radius and $Y_n^{m(c,s)}$ are the Schmidt quasi-normalized spherical harmonics as given in Eq. (2.32). The time-dependent coefficients $g_n^m(t)$ and $h_n^m(t)$ are the spherical harmonic (SH) coefficients of the potential, often referred to as Gauss coefficients. An expression for the magnetic field and in particular its radial component immediately follows after applying the gradient to the potential

$$B_r(r,\theta,\phi) = \sum_{n=1}^{\infty} \sum_{m=0}^{n} (n+1) \left(\frac{r_\mathrm{s}}{r}\right)^{n+2} \left(g_n^m(t) Y_n^{mc} + h_n^m(t) Y_n^{ms}\right) \tag{3.2}$$

and similarly for the radial SV

$$\frac{\partial B_r}{\partial t}(r,\theta,\phi) = \sum_{n=1}^{\infty} \sum_{m=0}^{n} (n+1) \left(\frac{r_\mathrm{s}}{r}\right)^{n+2} \left(\dot{g}_n^m(t) Y_n^{mc} + \dot{h}_n^m(t) Y_n^{ms}\right), \tag{3.3}$$

where the SH coefficients have been replaced with their respective time derivatives $\dot{g}_n^m(t)$ and $\dot{h}_n^m(t)$. Specifying the SH coefficients is therefore enough to specify the field itself or other related quantities. For example, the power spectrum per harmonic degree of the magnetic field is defined as (Sabaka et al., 2010)

$$W_n(r) = (n+1) \left(\frac{r_\mathrm{s}}{r}\right)^{2n+4} \sum_{m=1}^{n} (g_n^m)^2 + (h_n^m)^2 \tag{3.4}$$

and similarly for the SV. This spectrum is often referred to as Lowes-Mauerberger spectrum. In CHAOS-6-x2, the spherical harmonic decomposition is truncated at degree $n_\mathrm{max} = 20$ and the time-dependent SH coefficients of the potential are represented using a 6th-order B-spline basis defined over the time interval of the model. Since the time-dependence of the coefficients is absorbed into known B-spline functions, their derivative with respect to time is automatically known. Hence, the set of estimated spline coefficients can be used to calculate model predictions of both the internal field and its SV.

In this study, CHAOS-6-x2 model predictions for the core field and the SV at the core surface are required. By assuming the mantle to be insulating, the potential of the internal field in Eq. (3.1) can be downward-continued to the core surface by setting $r = r_\mathrm{c}$. However, Finlay et al. (2016) observed upward trends in the power spectrum at high degrees indicating that not the full model up to degree $n = 20$ can be safely evaluated at the core surface. They suggest using the model only up to degree $N_\mathrm{b} = 13$ for the core field prediction as lithospheric sources contaminate the spectrum at higher degrees. In the case of the SV, a maximum degree of $N_\mathrm{sv} = 16$ or possibly 18 is believed to provide

satisfactory predictions since increased noise is observed for higher degrees. In this study it was decided to truncate the model at degree $N_\mathrm{b} = N_\mathrm{sv} = 14$ for both the core field and the SV prediction in order to facilitate comparisons with previous studies, in particular Gillet et al. (2015b). Those are based on the COV-OBS model (Gillet et al., 2015a) that provides longer time series for the field and SV as well as related model covariance matrices.

3.2. Forward Problem

The forward problem formally consists of the radial part of the frozen-flux induction equation and involves predicting the SV given the flow and the magnetic field at the core surface at a given time. In practice however, not all lengthscales of the field and SV are accessible to observation or can be handled in practical computations. Hence, a truncation of the flow and field in spectral space cannot be avoided. However, one must take care when neglecting scales of the fields as the interaction of any lengthscale of the flow and the core field can result in appreciable large-scale SV. A detailed analysis of the model errors is therefore required (see Backus, 1968 for a detailed account of truncation problems of the induction equation).

3.2.1. Accounting for Unresolved Scales in the Induction Equation

At the core surface, only the large-scale core field and SV are known. The small-scales of the core field above degree 14 cannot be resolved due to the presence of the lithospheric field while knowledge of the small-scale SV is limited by the presence of noise in the field models. The large-scale radial SV, denoted $\partial\overline{B}_r/\partial t$, is then given by a modified version of Eq. (2.29) (Gillet et al., 2015a)

$$\frac{\partial \overline{B}_r}{\partial t} = -\overline{\nabla_\mathrm{H} \cdot \left(\mathbf{u}\overline{B}_r\right)} + e, \tag{3.5}$$

where the first term on the right describes the SV due to the interaction between the flow and the large-scale core field whereas $e = -\overline{\nabla_\mathrm{H} \cdot \left(\mathbf{u}\widetilde{B}_r\right)}$, the so-called small-scale error, accounts for the unknown small-scale field. Note that the total radial field has been written as $B_r = \overline{B}_r + \widetilde{B}_r$, the sum of the known large-scale and the small-scale core field. In the past, the uncertainties of the SV models themselves used to be the main limitation on flow computations. But thanks to high quality observations from satellites, this is no longer the case and instead the unknown small-scales of the core field and its influence on

the observable large-scale SV needs to be parametrized in the form of a small-scale error term e.

The truncation in the spectral domain of the radial magnetic field component is formally carried out by first assuming the field to be given as a potential field, then introducing a SH expansion of it and, finally, stopping the infinite series at a certain degree. Similarly, the core flow is replaced by its toroidal-poloidal expansion truncated at a chosen degree. This procedure allows Eq. (3.5) to be reformulated as a finite dimensional matrix equation of the involved expansion coefficients (see details in Sec. 3.2.3)

$$\dot{\mathbf{g}} = \mathbf{A}(\mathbf{g}) \cdot \mathbf{w} + \mathbf{e}. \tag{3.6}$$

Here, the vector $\dot{\mathbf{g}} = (\dot{g}_1^0, \dot{g}_1^1, \dot{h}_1^1, ...)^{\mathrm{T}}$ contains the SH coefficients up to degree N_{sv} of the SV and the vector $\mathbf{w} = (t_1^{0c}, t_1^{1c}, t_1^{1s}, ..., s_1^{0c}, ...)^{\mathrm{T}}$ has first the toroidal and then the poloidal flow coefficients at the core surface both truncated at degree N_{u}, whereas $\mathbf{g} = (g_1^0, g_1^1, h_1^1, ...)^{\mathrm{T}}$ contains the SH coefficients of the magnetic field up to N_{b}. The vector $\mathbf{e}$ consists of the SH coefficients of the small-scale error up to the same truncation degree as the SV. The matrix $\mathbf{A}$ is then a linear function in the magnetic field and contains the physics relating the flow to the radial field SV in form of the induction equation.

3.2.2. Forward Problem for Mode Amplitudes

By further representing the flow expansion as a linear combination of a set of modes (geostrophic and inertial, see Sec. 2.2) with coefficients a_i arranged in the vector $\mathbf{a} = (a_1, a_2, ...)^{\mathrm{T}}$ and the respective toroidal-poloidal expansion of the modes as columns $\mathbf{w}_i$ in a matrix $\mathbf{W} = (\mathbf{w}_1, \mathbf{w}_2, ...)$, one can write $\mathbf{w} = \mathbf{W} \cdot \mathbf{a}$ and the forward problem in terms of the mode coefficients can be written

$$\dot{\mathbf{g}} = \mathbf{H}(\mathbf{g}) \cdot \mathbf{a} + \mathbf{e} \quad \text{with} \quad \mathbf{H} = \mathbf{AW}. \tag{3.7}$$

The choice of the truncation degree N_{u} of the toroidal-poloidal expansion of the flow is related to the question of which flow scales are required to explain the observed SV. It is always possible to exactly fit the data with arbitrary small-scale flows which, however, might not be necessary. Often when inverting for the core flow, as many as possible flow scales are parametrized and then a solution is sought by penalizing the small-scales according to some norm (a large-scale approximation e.g. Bloxham and Jackson, 1991; Gillet et al., 2009).

Both the mode coefficients in $\mathbf{a}$ and the small-scale error in $\mathbf{e}$ need to be determined in order to predict the SV. It is therefore useful to write them together in a single augmented

vector $\mathbf{m} = (\mathbf{a}^{\mathrm{T}}, \mathbf{e}^{\mathrm{T}})^{\mathrm{T}}$, hereafter referred to as the model, such that

$$\dot{\mathbf{g}} = \mathbf{H}_{\mathrm{aug}}(\mathbf{g})\mathbf{m} \quad \text{with} \quad \mathbf{H}_{\mathrm{aug}} = \begin{pmatrix} \mathbf{H}(\mathbf{g}) & \mathbf{I} \end{pmatrix} \tag{3.8}$$

follows. Here, the unit matrix $\mathbf{I}$ augments the original matrix $\mathbf{H}$ and gives the forward problem in its final form. Note that $\mathbf{H}$ is a constant matrix since the magnetic field $\mathbf{g}$ is considered to be given and free of uncertainty at a specific epoch throughout this study.

3.2.3. Numerical Treatment of the Induction Equation

In the following, details are given of the numerical solution of the induction equation. Inspired by a FORTRAN code originally written by D. Lloyd in 1987 (Lloyd and Gubbins, 1990) and later amended by A. Jackson, a code to reproduce the matrix $\mathbf{A}$ was written and tested in MATLAB as part of a development project prior to this study.

First, the induction Eq. (2.28) is rewritten by applying the horizontal gradient on the product $\mathbf{u}B_r$. Making use of the incompressibility of the flow allows the elimination of the horizontal derivatives of the flow components in favor of the radial derivative u_r'

$$\frac{\partial \mathbf{B}}{\partial t} = -\big(\mathbf{u} \cdot \nabla_{\mathrm{H}}\big) B_r + B_r u_r'.$$

On the right side of the induction equation, the toroidal-poloidal expansions of the flow components

$$u_\theta(r,\theta,\phi) = \sum_{n=1}^{\infty}\sum_{m=0}^{n} \left(t_n^{mc}(r)T_{n,\theta}^{mc} + t_n^{ms}(r)T_{n,\theta}^{ms} + s_n^{mc}(r)S_{n,\theta}^{mc} + s_n^{ms}(r)S_{n,\theta}^{ms}\right) \tag{3.9a}$$

$$u_\phi(r,\theta,\phi) = \sum_{n=1}^{\infty}\sum_{m=0}^{n} \left(t_n^{mc}(r)T_{n,\phi}^{mc} + t_n^{ms}(r)T_{n,\phi}^{ms} + s_n^{mc}(r)S_{n,\phi}^{mc} + s_n^{ms}(r)S_{n,\phi}^{ms}\right) \tag{3.9b}$$

$$u_r'(r,\theta,\phi) = \sum_{n=1}^{\infty}\sum_{m=0}^{n} n(n+1)\left(\frac{\mathrm{d}p_n^{mc}}{\mathrm{d}r}P_{n,r}^{mc} + \frac{\mathrm{d}p_n^{ms}}{\mathrm{d}r}P_{n,r}^{ms}\right) \tag{3.9c}$$

are then inserted and the whole expression is evaluated at the CMB with $r = r_{\mathrm{c}}$. While remembering that

$$s_n^{m(c,s)} = \frac{\mathrm{d}}{\mathrm{d}r}\left(r p_n^{m(c,s)}\right) = p_n^{m(c,s)} + r\frac{\mathrm{d}p_n^{m(c,s)}}{\mathrm{d}r}$$
$$\overset{\text{at CMB}}{\Longrightarrow} \left.\frac{\mathrm{d}p_n^{m(c,s)}}{\mathrm{d}r}\right|_{r_{\mathrm{c}}} = -\frac{1}{r_{\mathrm{c}}}s_n^{m(c,s)}(r_{\mathrm{c}}),$$

since $p_n^{m(c,s)}(r_{\mathrm{c}}) = 0$ at the CMB, one can establish an expression for the radial SV consisting of terms that originate from either the toroidal or the poloidal part of the flow

$$\frac{\partial B_r}{\partial t} = \left(\frac{\partial B_r}{\partial t}\right)_{\mathrm{tor}} + \left(\frac{\partial B_r}{\partial t}\right)_{\mathrm{pol}} \tag{3.10a}$$

with

$$\left(\frac{\partial B_r}{\partial t}\right)_{\text{tor}} = -\frac{1}{r_\text{c}}\sum_{n=1}^{\infty}\sum_{m=0}^{n}\left[\left(T_{n,\theta}^{mc}\frac{\partial B_r}{\partial\theta}+\frac{T_{n,\phi}^{m,c}}{\sin\theta}\frac{\partial B_r}{\partial\phi}\right)t_n^{m,c} + \left(T_{n,\theta}^{ms}\frac{\partial B_r}{\partial\theta}+\frac{T_{n,\phi}^{ms}}{\sin\theta}\frac{\partial B_r}{\partial\phi}\right)t_n^{m,s}\right] \tag{3.10b}$$

and

$$\left(\frac{\partial B_r}{\partial t}\right)_{\text{pol}} = -\frac{1}{r_\text{c}}\sum_{n=1}^{\infty}\sum_{m=0}^{n}\left[\left(S_{n,\theta}^{mc}\frac{\partial B_r}{\partial\theta}+\frac{S_{n,\phi}^{mc}}{\sin\theta}\frac{\partial B_r}{\partial\phi}-n(n+1)P_{n,r}^{mc}B_r\right)s_n^{mc} + \left(S_{n,\theta}^{ms}\frac{\partial B_r}{\partial\theta}+\frac{S_{n,\phi}^{ms}}{\sin\theta}\frac{\partial B_r}{\partial\phi}-n(n+1)P_{n,r}^{ms}B_r\right)s_n^{m,s}\right]. \tag{3.10c}$$

If the magnetic field is also a potential field, then the dependence of the induction equation on spatial coordinates can be entirely eliminated by relating the flow coefficients to the SH coefficients of the SV. The radial components of the core field and the SV are then given by Eq. (3.2) and (3.3). The SH coefficients of the SV are isolated by making use of the orthogonality relations of the spherical harmonics in Eq. (2.33) so that the integral over the complete spherical surface (Eq. 2.33) yields the expression

$$\dot{g}_l^k = \frac{1}{l+1}\frac{2l+1}{1+\delta_{0k}}\left(\frac{r_\text{c}}{r_\text{s}}\right)^{l+2}\left\langle\left(\frac{\partial B_r}{\partial t}\right), Y_l^{kc}\right\rangle, \tag{3.11}$$

where again, $r_\text{s} = 6371.2\,\text{km}$ is the mean surface radius of Earth, and similarly for $\dot{h}_l^k$ by using Y_l^{ks} instead. Since the toroidal-poloidal coefficients are constant on the CMB, they can be moved out of the surface integration. Truncating the expansion of the SV at degree N_sv and the flow at N_u allows Eq. (3.11) to be written for all SV coefficients at once in terms of a finite dimensional matrix equation involving the multiplication of matrix $\mathbf{A}$ and the vector $\mathbf{w}$ which contains the flow expansion coefficients. $\mathbf{A}$ is then of size $N_\text{sv}(N_\text{sv}+2)\times 2N_\text{u}(N_\text{u}+1)$ and its elements are the normalized surface integrals Eq. (3.11) of spherical harmonics and the expressions in front of the toroidal-poloidal coefficients in Eq. (3.10).

The numerical evaluation of the surface integrals is carried out on a grid on the spherical surface with constant spacing in azimuth and points in colatitude at the roots of the Legendre polynomial $P_{N_\theta}(x=\cos\theta)$ of degree N_θ. This choice of grid allows a numerical integration in colatitude by using the Gauss-Legendre quadrature (GLQ) and in azimuth the Fast Fourier Transform (FFT). The GLQ is exact when applied to polynomials of degree smaller than or equal to $2N_\theta - 1$. The minimum grid size in colatitude can be found by identifying in Eq. (3.10) from the polynomial the highest possible degree in $x = \cos\theta$. The degree of the magnetic field derivatives is N_b because they are derived from

a truncated model. The maximum possible degree of the vector spherical harmonic flow components is N_u while it is N_sv for the SV. The multiplication of all three polynomials for the surface integration gives a polynomial of degree $N_\mathrm{u}+N_\mathrm{b}+N_\mathrm{sv}$ in x. Hence for the GLQ, a grid in colatitude must have at least $N_\theta > \frac{1}{2}(N_\mathrm{u}+N_\mathrm{b}+N_\mathrm{sv}+1)$ points. A similar consideration of the azimuthal dependence shows that $N_\phi = 2N_\theta$ points are required for the FFT.

3.2.4. Toroidal-Poloidal Expansion of Geostrophic and Inertial Modes

In order to relate the radial SV to the geostrophic and inertial mode amplitudes, a toroidal-poloidal expansion is required. Once the expansion for a set of modes is selected, the matrix $\mathbf{W}$ containing the mode expansion coefficients as columns is built. In the following, the approach used in this study to represent the analytical mode expressions (Eq. 2.15, 2.20 and 2.25) is presented. A MATLAB implementation was built as part of a development project prior to this study. In the same project, tests and comparisons with independent codes were carried out to benchmark the approach. It is important to note that the approach relies on the fact that the vector SH spectra of the modes has a finite width being zero beyond the chosen truncation degree.

The implementation of the toroidal-poloidal expansion involved generating a sufficiently dense and equally-spaced grid at the spherical CMB and explicitly calculating the horizontal components of a chosen mode there as specified in Sec. 2.2, normalizing by the volume integral of the squared velocity. Since the components are equally well represented as a linear combination of explicitly evaluated vector spherical harmonics $\mathbf{T}_n^{m(c,s)}$ and $\mathbf{S}_n^{m(c,s)}$ up to a truncation degree N_u on the same grid, a system of equations connecting the flow components with the toroidal-poloidal coefficients can be found. The $\mathbf{P_n^{m(c,s)}}$ components are not required since there is no radial component of the modes at the CMB. Let $N = N_\theta N_\phi$ be the total number of grid points on the sphere with N_θ the number of points in colatitude and N_ϕ in azimuth. At every grid point, there are two equations relating the horizontal flow components with the corresponding components of the vector spherical harmonics. Hence, in total there are $2N$ equations which can be rearranged to the matrix equation

$$\mathbf{q} = \mathbf{G_{exp}}\mathbf{w}, \tag{3.12}$$

where the vector $\mathbf{q}$ of length $2N$ contains the horizontal components of the mode evaluated at the grid points whereas the vector $\mathbf{w}$ consists of $2N_\mathrm{u}(N_\mathrm{u}+2)$ toroidal-poloidal expansion coefficients up to degree N_u. Both are connected through the matrix $\mathbf{G_{exp}}$ which is of size $2N \times 2N_\mathrm{u}(N_\mathrm{u}+2)$ and has then in every single column the components of a vector spherical

harmonic evaluated on the same grid. Provided that N_u is high enough to capture the non-zero part of the toroidal-poloidal spectrum, the vector $\mathbf{w}$ can be estimated by using Gaussian elimination by solving the normal equation

$$(\mathbf{G}_{\mathbf{exp}}^{\mathrm{T}}\mathbf{G}_{\mathbf{exp}})\hat{\mathbf{w}} = \mathbf{G}_{\mathbf{exp}}^{\mathrm{T}}\mathbf{q}. \tag{3.13}$$

The expansion coefficients in $\hat{\mathbf{w}}$ are then by construction the ones that minimize the squared norm $\|\mathbf{q} - \mathbf{G}_{\mathbf{exp}}\mathbf{w}\|^2$ and ensure the closest representation in this measure given the truncation N_u. Based on several tests during the development project and the repeated observation that the spectrum is bounded, it can be stated that $\mathbf{w} = \hat{\mathbf{w}}$ holds[1] and represents the desired toroidal-poloidal expansion. The grid size must be chosen in such a way that both the modes and the vector spherical harmonics are adequately sampled on the sphere. By observing that they are polynomials of sines and cosines in colatitude and azimuth, one can choose a grid size based on the degree of the polynomials and the sampling theorem. Here for explanatory purposes, the highest polynomial degree of the mode components in colatitude is called degree while in azimuth it is denoted order by analogy with spherical harmonics. The geostrophic modes then have degree $2k-1$ and order zero since they are axisymmetric. The symmetric modes have degree $2N+M$ and the antisymmetric modes $2N+M+1$ while both share the same order M. Since the vector spherical harmonics should have at least the same degree and order as the modes they are decomposing, it follows that N_u must be greater than or equal to the degree of the involved modes either geostrophic or inertial. When the decomposition is truncated at N_u then the highest order of the spherical vector harmonics is also equal to $m = N_\mathrm{u}$. Hence, the grid should at least have a sample spacing of $\Delta\theta = \Delta\phi = \frac{2\pi}{2N_\mathrm{u}+1}$ while excluding the poles as the vector spherical harmonics are singular there. It should also be noted that the vector spherical harmonics and the inertial modes share the same order, i.e., an inertial mode of order M will be solely represented by harmonics of order $m = M$.

For every member in a set of modes, the vectors $\mathbf{q}_i$ were constructed by numerically determining the mode frequencies as the roots of the polynomials in σ and evaluating the horizontal components on the grid. The components were then together normalized by the mean of their squared magnitude over the unit sphere (square roots of Eq. 2.14, 2.22 and 2.27) and arranged in a matrix $\mathbf{Q} = (\mathbf{q}_1, \mathbf{q}_2, ...)$. Finally, they were collectively decomposed into their expansion, denoted with the matrix $\mathbf{W}$, by solving Eq. (3.13) with $\mathbf{Q}$ instead of $\mathbf{q}$. Note that the geostrophic modes only have velocity components in the azimuthal direction. Therefore, the same number of zero-valued meridional components had to be added to ensure the correct length of the vectors. Note also in the case of the inertial modes that there are in fact two modes, corresponding to the real and the

[1] To an accuracy smaller than 1×10^{-4} as measured by the rms ratio $(\mathbf{q} - \mathbf{G}_{\mathrm{exp}}\hat{\mathbf{w}})_{\mathrm{rms}}/(\mathbf{q})_{\mathrm{rms}}$.

imaginary parts, for a given N, M and σ in order to allow for the correct phase in azimuth. When the modes on the grid were computed, it turned out that numerical problems appear for inertial modes of $N > 5$ and $M > 10$. The reason is that the mode expressions involve the addition of terms of very different scales for which the precision of 16 digits was not sufficient. Especially when the mean over the volume for the normalization was computed, this problem became apparent in the form of negative values. For complex modes of high N and M, high precision computing was therefore required[2].

3.2.5. Prediction of SV Only Outside the Tangent Cylinder

So far, the description of the core motions in terms of the geostrophic and inertial modes has been based on a full-sphere geometry which completely neglects the influence of the solid inner core. In reality, the existence of the inner core imposes additional boundary conditions that will change the motions although they are still likely to be dominated by the Coriolis force and broadly columnar. The cylinder parallel to the rotation axis and touching tangentially the inner core is called the tangent cylinder (TC). It separates regions of distinct physical processes and intersects the CMB at around $\pm 69°$ latitude (Livermore et al., 2017). The region outside the TC extends over mid and low latitudes and includes the equatorial region. The core motion there is assumed to be only slightly affected by the inner core so that a representation of motions in terms of geostrophic and inertial modes is still possible. This is especially a reasonable assumption for the QG-modes which are mostly localized to the equator and are small close to the rotation axis or inside the TC. The geostrophic modes (and more generally all toroidal modes) are in fact not affected by the inner core as they automatically also satisfy the impenetrable condition there.

The separation of the field into a region inside and outside the TC is not possible when inverting the SV given as global SH. However, the polar regions can be excluded by evaluating the SV on a grid outside the TC with the help of a SH synthesis matrix $\mathbf{G}_{\mathrm{grd}}$. It multiplies a vector containing SH coefficients to give gridded values at the specified points. Here, an equal area grid on the sphere between $\pm 60°$ latitude was defined, thus, making sure to account only for the region well-outside the TC (Fig. 3.1). In MATLAB, the grid was implemented with the help of the Recursive Zonal Equal Area Sphere Partitioning Toolbox (Leopardi, 2006). The equal-area grid ensures that high-latitude SV is not disproportionally weighted compared to low-latitudes. The equal-area

[2]This was implemented in MATLAB by using variable-precision arithmetic.

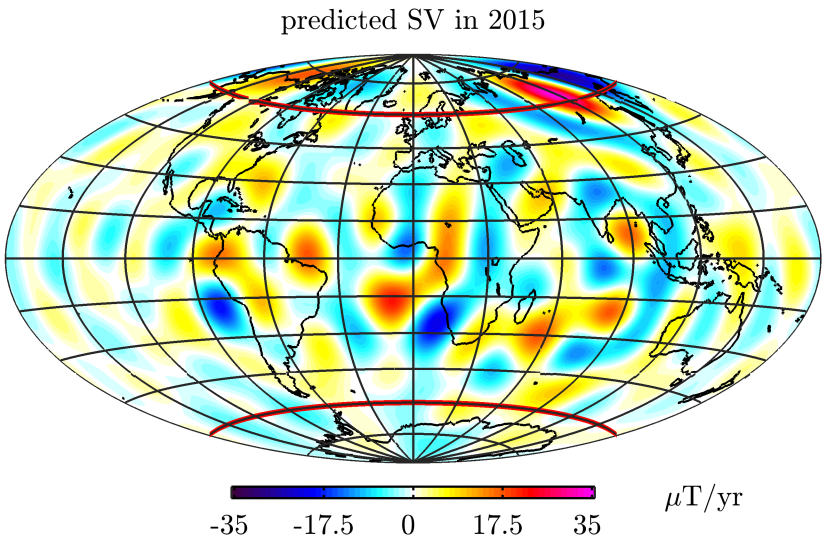

Figure 3.1. SV calculated from CHAOS-6-x2 in 2015 up to degree 14 at the CMB. The red lines at ±60° latitude indicate the borders of the region outside the TC.

gridded radial field SV outside the TC is arranged in the column vector $\dot{\mathbf{b}}$ given by

$$\dot{\mathbf{b}} = \mathbf{G}_{\text{grd}}\dot{\mathbf{g}} = \mathbf{G}_{\text{grd}}\mathbf{H}_{\text{aug}}\mathbf{m}, \tag{3.14}$$

where $\dot{\mathbf{g}}$ stores the SH coefficients of the SV and Eq. (3.8) has been used. This equation is then equivalent to the forward problem in Eq. (3.8) except that it predicts gridded values of SV at the core surface, outside the TC.

3.3. Inversion for Modes of Core Flow

In this study, the inverse problem consists of finding a core flow model that reproduces the SV observations to an appropriate level of misfit according to the forward modeling scheme expressed as

$$\mathbf{d}_{\text{prd}} = \mathbf{G}\mathbf{m}, \tag{3.15}$$

where $\mathbf{d_{prd}}$ denotes the predicted data in terms of either the SH coefficients $\dot{\mathbf{g}}$ or gridded values $\dot{\mathbf{b}}$ of the SV. Correspondingly, the system matrix $\mathbf{G}$ is either $\mathbf{H_{aug}}$ or $\mathbf{G_{grd}H_{aug}}$ while the model $\mathbf{m}$ always contains the core flow mode coefficients and the SH coefficients of the small-scale error $(\mathbf{a}^{\text{T}}, \mathbf{e}^{\text{T}})^{\text{T}}$.

A simple solution to the inverse problem is found by minimizing the cost function (Aster et al., 2013)

$$\Phi = (\mathbf{d}_{\text{prd}} - \mathbf{d}_{\text{obs}})^{\text{T}}\mathbf{W}_{\text{d}}(\mathbf{d}_{\text{prd}} - \mathbf{d}_{\text{obs}}) + R(\mathbf{x}) \tag{3.16}$$

with respect to the model $\mathbf{m}$. The first term measures the least-squares misfit between the predicted data $\mathbf{d}_{\text{pred}}$ and the observed data $\mathbf{d}_{\text{obs}}$ with weights $\mathbf{W}_{\text{d}}$ whereas $R(\mathbf{x})$ is some measure of the model complexity, based on a linear operation on the model parameters $\mathbf{x} = \mathbf{L}\mathbf{m}$ and serves as a regularization to reduce the inherent ambiguities on the flow inversion.

For a linear problem, a minimum can be found by taking the derivative of the cost function Eq. (3.16) with respect to the model and setting it to zero.

Considering a general measure of complexity $R(\mathbf{x})$ of a vector $\mathbf{x}$ having N elements. R may be written as (Farquharson and Oldenburg, 1998)

$$R(\mathbf{x}) = \sum_{j=1}^{N} \rho(x_j), \tag{3.17}$$

where $\rho(x)$ is chosen such that R is equivalent to the l_p-norm of $\mathbf{x}$

$$\|\mathbf{x}\|_p^p = \sum_{j=1}^{N} |x_j|^p$$

with $1 \leq p < \infty$. In particular, the two cases with $p = 1$ and $p = 2$ are of interest in this study. In the second case with $p = 2$, $\rho(x) = x^2$, and R corresponds to the square of the Euclidean norm. In the other case with $p = 1$, R becomes the sum of the absolute values of the elements in $\mathbf{x}$. By assuming $\mathbf{x}$ to be a function of the model $\mathbf{m}$, the derivative of R with respect to the model can be written

$$\frac{\partial R(\mathbf{x})}{\partial \mathbf{m}} = \sum_{j=1}^{N} \rho'(x_j) \frac{\partial x_j}{\partial \mathbf{m}} \tag{3.18}$$

where $\frac{\partial}{\partial \mathbf{m}} = (\frac{\partial}{\partial m_1}, \frac{\partial}{\partial m_2}, ...)^{\text{T}}$ is a column vector and ρ' the derivative with respect to its argument. Following Farquharson and Oldenburg (1998), ρ' can be replaced with $(\rho'/x_j)x_j$ in order to yield a system of equations that can be handled within a least-squares routine. Eq. (3.18) can be rewritten as a matrix equation

$$\frac{\partial R(\mathbf{x})}{\partial \mathbf{m}} = \begin{pmatrix} \frac{\partial x_1}{\partial \mathbf{m}} & \frac{\partial x_2}{\partial \mathbf{m}} & \cdots \end{pmatrix} \begin{pmatrix} \frac{\rho'(x_1)}{x_1} & & \\ & \frac{\rho'(x_2)}{x_2} & \\ & & \ddots \end{pmatrix} \begin{pmatrix} x_1 \\ x_2 \\ \vdots \end{pmatrix}. \tag{3.19}$$

The derivative of $R(\mathbf{x})$ with respect to the model is then given by

$$\frac{\partial R(\mathbf{x})}{\partial \mathbf{m}} = \mathbf{L}^{\text{T}} \mathbf{W}_{\text{m}} \mathbf{L} \ \ \mathbf{m}, \tag{3.20}$$

where $(\mathbf{W}_{\text{m}})_{ij} = \delta_{ij} \frac{\rho'(x_i)}{x_i}$ are weights that depends on the form of the chosen norm. For a simple l_2-norm the diagonal entries are constant and equal to two. In case of an l_1-norm,

however, the diagonal entries are equivalent to the inverse of the absolute values of x_i provided they are strictly non-zero.

From a numerical point of view, small values of x_i will cause problems so that instead, Ekblom's measure

$$\rho(x) = (x^2 + \epsilon^2)^{\frac{p}{2}} \tag{3.21}$$

with $p = 1$ is used as an approximation of the l_1-norm provided the constant ϵ is sufficiently small compared to the typical size of the entries in $\mathbf{x}$ (Farquharson and Oldenburg, 1998). With the Ekblom measure, the elements of the weighting matrix are $(\mathbf{W}_\mathrm{m})_{ij} = \delta_{ij} \frac{1}{\sqrt{x_i^2+\epsilon^2}}$.

Recalling that $\mathbf{d}_\mathrm{prd} = \mathbf{G}\mathbf{m}$, the cost function in Eq. (3.16) can be now differentiated, set to zero and rearranged to yield an equation in terms of the model estimate $\hat{\mathbf{m}}$

$$\left(\mathbf{G}^\mathrm{T}\mathbf{W}_\mathrm{d}\mathbf{G} + \mathbf{L}^\mathrm{T}\mathbf{W}_\mathrm{m}\mathbf{L}\ \right)\hat{\mathbf{m}} = \mathbf{G}^\mathrm{T}\mathbf{W}_\mathrm{d}\mathbf{d}_\mathrm{obs}. \tag{3.22}$$

Since $\mathbf{W}_\mathrm{m}$ can depend on the model itself, Eq. (3.22) is non-linear in terms of the model. It should be therefore understood as an iterative procedure of computing models $\hat{\mathbf{m}}^{(k)}$ of the kth iteration given such that

$$\hat{\mathbf{m}}^{(k)} = \left(\mathbf{G}^\mathrm{T}\mathbf{W}_\mathrm{d}\mathbf{G} + \mathbf{L}^\mathrm{T}\mathbf{W}_\mathrm{m}^{(\mathrm{k}-1)}\mathbf{L}\right)^{-1} \cdot \mathbf{G}^\mathrm{T}\mathbf{W}_\mathrm{d}\mathbf{d}_\mathrm{obs}. \tag{3.23}$$

The inverse $(\cdot)^{-1}$ is only explicitly stated here but implicitly calculated in the actual computations by using the backslash-operator to solve the linear system in MATLAB. The procedure is initiated by choosing $\mathbf{W}_\mathrm{m}^{(0)} = \mathbf{I}$ which is then updated to $\mathbf{W}_\mathrm{m}^{(1)}(\hat{\mathbf{m}}^{(1)})$ after the first iterate has been computed. These steps are then repeated until a convergence criterion is fulfilled (see Sec. 4.3 for details). The described iterative procedure is commonly referred to as iteratively re-weighted least-squares (IRLS) for minimizing a non-linear system of equations.

It is assumed that residuals $\mathbf{d}_\mathrm{prd} - \mathbf{d}_\mathrm{obs}$ are Gaussian distributed with zero mean and variances as specified in the diagonal data covariance matrix $\mathbf{C}_\mathrm{d}$ so that $\mathbf{W}_\mathrm{d} = \mathbf{C}_\mathrm{d}^{-1}$.

3.3.1. Choice of Model Regularization

In this study, the two parts of the model vector, the mode amplitude $\mathbf{a}$ and the small-scale error $\mathbf{e}$, are treated separately. Therefore, the measure of model complexity is written

$$R(\mathbf{m}) = \lambda R_\mathrm{a}(\mathbf{a}) + R_\mathrm{e}(\mathbf{e}), \tag{3.24}$$

where $\mathbf{m} = (\mathbf{a}^\mathrm{T}, \mathbf{e}^\mathrm{T})^\mathrm{T}$ and λ is a positive and constant regularization parameter that has to be adjusted in order to find an appropriate balance between the data misfit and the

model complexity. The regularization parameter has only been included in front of the term that measures the flow structure. This stresses the point that the prior information of the small-scale error is considered to be fixed and does not need to be tuned by a regularization parameter.

Taking the derivative with respect to the model yields, according to Eq. (3.20),

$$\frac{\partial R}{\partial \mathbf{m}} = \begin{pmatrix} \lambda \mathbf{W}_\mathrm{a} & \\ & \mathbf{W}_\mathrm{e} \end{pmatrix} \mathbf{m} = \mathbf{R}\mathrm{m}, \tag{3.25}$$

where $\mathbf{W}_\mathrm{a}$ and $\mathbf{W}_\mathrm{e}$ are the weights depending on the chosen norm for the mode coefficients and the small-scale error term. Two choices of R_a in Eq. (3.24) are explored, a conventional quadratic (l_2) measure and a new approach, based on the l_1-norm of the mode amplitudes.

Regularization of Small-Scale Error

The small-scale error is assumed to be correlated and Gaussian distributed with zero mean. The corresponding covariance matrix $\mathbf{C}_\mathrm{e}$ is then a full matrix and $\mathbf{W}_\mathrm{e} = \mathbf{C}_\mathrm{e}^{-1}$. Prior information regarding $\mathbf{C}_\mathrm{e}$ is derived from statistics provided by 3D and self-consistent numerical simulations of the geodynamo (Aubert, 2013). For this study, the matrix $\mathbf{C}_\mathrm{e}$ was supplied by courtesy of Barrois et al. (2017). The matrix $\mathbf{R}$ in Eq. (3.25) becomes

$$\mathbf{R} = \begin{pmatrix} \lambda \mathbf{W}_\mathrm{a} & \\ & \mathbf{C}_\mathrm{e}^{-1} \end{pmatrix} \tag{3.26}$$

l_2-Norm Regularization of Flow

In this study, two types of regularization are explored. The first, is a standard l_2-norm as used by Gillet et al. (2009). It acts on the SH coefficients of the toroidal-poloidal scalar flow potentials and can be derived from the surface integral at the CMB (Gillet et al., 2009)

$$\int_\mathrm{CMB} (\mathcal{D}^2 + \mathcal{V}^2) \mathrm{d}S \propto \mathbf{w}^\mathrm{T} \mathbf{N} \mathbf{w}, \tag{3.27}$$

with $\mathcal{D} = \nabla_\mathrm{H} \cdot \mathbf{u}$ the horizontal divergence, $\mathcal{V} = \mathbf{e}_r \cdot \nabla \times \mathbf{u}$ the radial component of the vorticity, the vector $\mathbf{w}$ with the toroidal-poloidal coefficients of the flow $\mathbf{u}$ and the matrix $\mathbf{N}$. $\mathbf{N}$ is diagonal and has entries that vary with n^3 of the harmonic degree of the toroidal-poloidal coefficients. Projecting from the toroidal-poloidal basis onto the modes of core flows means minimizing $(\mathbf{Wa})^\mathrm{T}\mathbf{NWa}$ with $\mathbf{w} = \mathbf{Wa}$ (similarly to Eq. 3.7). In this case, Eq. (3.26) is

$$\mathbf{R} = \begin{pmatrix} \lambda \mathbf{W}^\mathrm{T} \mathbf{N} \mathbf{W} & \\ & \mathbf{C}_\mathrm{e}^{-1} \end{pmatrix} \tag{3.28}$$

and Eq. (3.23) reduces to

$$\hat{\mathbf{m}} = \left(\mathbf{G}^{\mathrm{T}}\mathbf{W}_{\mathrm{d}}\mathbf{G} + \mathbf{R}\right)^{-1} \cdot \mathbf{G}^{\mathrm{T}}\mathbf{C}_{\mathrm{d}}^{-1}\mathbf{d}_{\mathrm{obs}}. \tag{3.29}$$

with λ being the chosen regularization parameter. Note that the computation of the model estimate now only contains constant weighting matrices such that an iterative procedure is not required and the solution immediately follows by solving for $\hat{\mathbf{m}}$.

l_1-Norm Regularization of the Mode Amplitudes

The interesting point of using the l_1-norm is that it approximates the l_0-norm which measures the non-zero entries of some vector. Minimizing the mode coefficients $\mathbf{a}$ with respect to the l_1-norm therefore promotes sparsity in the sense that most of the mode are pushed towards zero while a few important ones are retained to fit the data. Similar to Eq. (3.26),

$$\mathbf{R} = \begin{pmatrix} \lambda\mathbf{W}_{\mathrm{a}} & \\ & \mathbf{C}_{\mathrm{e}}^{-1} \end{pmatrix} \quad \text{with} \quad (\mathbf{W}_{\mathrm{a}})_{ij} = \frac{\delta_{ij}}{\sqrt{a_i^2 + \epsilon^2}}. \tag{3.30}$$

The weighting matrix $\mathbf{W}_{\mathrm{a}}$ depends on the mode coefficients in $\mathbf{a}$. The iterative procedure in Eq. (3.23) is given by

$$\hat{\mathbf{m}}^{(k)} = \left(\mathbf{G}^{\mathrm{T}}\mathbf{C}_{\mathrm{d}}^{-1}\mathbf{G} + \mathbf{R}^{(\mathrm{k}-1)}\right)^{-1} \cdot \mathbf{G}^{\mathrm{T}}\mathbf{C}_{\mathrm{d}}^{-1}\mathbf{d}_{\mathrm{obs}}. \tag{3.31}$$

4. Results

This chapter presents the application of the developed inversion scheme to observations of the geomagnetic field, as provided by the CHAOS-6-x2 model. After a comparison to previous results (Sec. 4.1), the estimated flow structure given different sets of modes is described in detail (Sec. 4.2 and 4.3) before the time-dependence of the estimated flows is documented in the context of single epoch inversions (Sec. 4.4). Associated changes in the length of day are calculated as means of assessing the models.

4.1. Comparisons to Previous Results

In a first application of the inversion scheme using the geostrophic and inertial modes of this study, the ability to reproduce core surface flows derived by other authors under similar dynamical constraints was tested. In particular, columnar flows derived by Gillet et al. (2015b) in a time-dependent ensemble method were used for the comparison here. Although their approach is different, the inversion scheme developed in this study proved under similar regularization constraints to be capable of producing almost identical looking flow patterns.

Gillet et al. (2015b) propose a stochastic framework which consists of inverting recursively for an ensemble of solutions given SH coefficients of observed SV and corresponding uncertainties. They also account for temporal correlations of the uncertainties and calculate the covariance matrix for the small-scale error. The most probable solution is then computed as an average of the ensemble of flow solutions. They rely on the columnar flow constraint at the core surface (Gillet et al., 2015b)

$$\nabla_\mathrm{H} \cdot (\mathbf{u} \cos^2 \theta),$$

and simultaneously impose equatorial symmetry while allowing the flow to penetrate the TC. For the comparison reported here, only the ensemble average of the flow solutions in epoch 2005 will be used.

The inversion scheme of this study was adjusted to resemble as much as possible the set-up of the approach from Gillet et al. (2015b) in terms of observation data and model. In particular, it was decided to use the SH coefficients of the magnetic field and SV from COV-OBS.x1 up to degree 14 in epoch 2005 as used by Gillet et al. (2015b). For regularization of the flow, Gillet's l_2-norm in Eq. (3.27), which increasingly suppresses high degree components with n^3 of the toroidal-poloidal spectrum, was chosen. The use of this norm effectively penalizes small-scale flow. In order to resemble the columnar flow constraint of Gillet et al. (2015b), a set of geostrophic modes with $1 \leq k \leq 20$ and QG inertial modes with $1 \leq N \leq 10$ and $1 \leq M \leq 16$ was chosen. Consequently, the first 20 entries of the coefficients vector $\mathbf{a}$ was associated with the geostrophic modes, while the remaining part of $\mathbf{a}$ consisting of 320 entries accounted for the 160 QG inertial modes with two coefficients per each mode. Hence, there was a total number of 340 mode coefficients that were combined with the 224 SH coefficients of the small-scale error up to degree 14 to the model vector $\mathbf{m}$ of length 564. Since, following Gillet et al. (2015b), the observations were given in terms of SH coefficients of the COV-OBS field model, the SV on the entire CMB was included in this inversion and no distinction between the inner and outer part of the TC was made. The model was determined by solving Eq. (3.29) with $\mathbf{d}_{\text{obs}} = \dot{\mathbf{g}}$, the SV of COV-OBS in 2005, and $\mathbf{G} = \mathbf{H}_{\text{aug}}$. The unknown regularization parameter λ leads to a whole family of solutions. Instead of specifying a target misfit, the regularization parameter was picked based on maximizing two correlation factors which measured the similarity between the estimated flow $\mathbf{u}$ and Gillet's flow $\bar{\mathbf{u}}$. The first one provided a point-wise correlation defined as (Amit et al., 2007)

$$c_{\text{point}} = 1 - \frac{\int_{\text{CMB}} |\mathbf{u} - \bar{\mathbf{u}}| \, \mathrm{d}S}{\int_{\text{CMB}} |\mathbf{u} + \bar{\mathbf{u}}| \, \mathrm{d}S} \tag{4.1}$$

whereas the second one, known as the pattern correlation factor, assessed the fields more globally (Rau et al., 2000)

$$c_{\text{pattern}} = \frac{\int_{\text{CMB}} \mathbf{u} \cdot \bar{\mathbf{u}} \mathrm{d}S}{\sqrt{\int_{\text{CMB}} |\mathbf{u}|^2 \, \mathrm{d}S} \sqrt{\int_{\text{CMB}} |\bar{\mathbf{u}}|^2 \, \mathrm{d}S}}. \tag{4.2}$$

The surface integral in the pattern correlation factor could be related to the toroidal-poloidal coefficients with

$$\int_{\text{CMB}} \mathbf{u} \cdot \bar{\mathbf{u}} \mathrm{d}S = \sum_n \sum_m \frac{n(n+1)}{2n+1} (t_n^{mc} \bar{t}_n^{mc} + t_n^{ms} \bar{t}_n^{ms} + s_n^{mc} \bar{s}_n^{mc} + s_n^{ms} \bar{s}_n^{ms})$$

while the point-wise correlation was calculated by first evaluating the velocity fields on a Gauss-Legendre grid and then summing the grid points with the appropriate weights. Since the Gillet et al. (2015b) flow was only provided up to harmonic degree 20 of the

toroidal-poloidal spectrum, zero valued coefficients up to degree 39 were added to match the number of the expansion coefficients.

In order to maximize point-wise and pattern correlation factors with the flow of Gillet et al. (2015b) in epoch 2005, the regularization parameter was fixed to $\lambda = 0.0128$. Maps of the estimated flow and the ensemble average at that epoch are presented for comparison in Fig. 4.1.

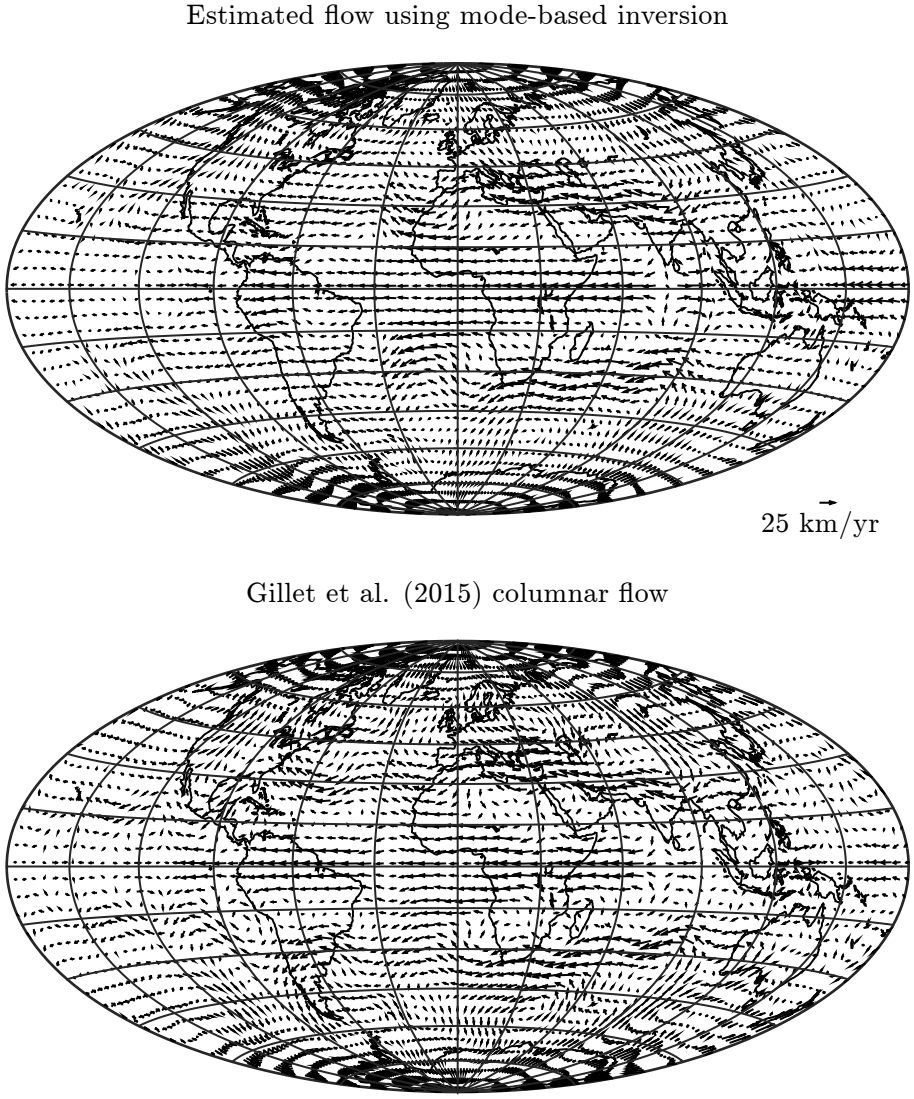

Figure 4.1. Top panel: estimated QG flow at the CMB (Hammer-Aitoff projection centered on the Greenwich meridian) in epoch 2005 under a regularized inversion given the l_2-norm to penalize small-scale flow. The meridians (parallels) are drawn every 30° (15°). Bottom panel: ensemble average at the CMB in epoch 2005 (Gillet et al., 2015b).

The flow derived from the inversion scheme of this study and the flow of Gillet et al. (2015b) are found to have very similar features at the CMB including a strong westward flow in mid and low latitudes as well as gyres of different scales. Both maps show an

equator-directed flow along the 100°E meridian which becomes a strong and meandering west-ward drift between 30° and 45° latitude, and finally flows back to the polar regions at around 90°W. This flow at the CMB looks similar to the one caused by an eccentric planetary-scale gyre which has been described in earlier studies using broadly columnar flow constraints (Gillet et al., 2009; Jault, 2008). Furthermore, two smaller anticyclones within the gyre centered at (45°E, 60°N and S) and (60°W, 45°N and S) are identified by Gillet et al. (2015b) and at least the first of the two also appear here. When looking at the region around the Atlantic sector within 15°N and S, a strong westward drift in both maps is present. However, the estimated flow obtained in this study appears more uniform there compared to the flow of Gillet et al. (2015b) which shows small deflections from westward flow at around 30°E and W in that region. Overall, however, this test demonstrates that the new inversion scheme based on geostrophic and inertial modes can reproduce previous results.

4.2. Regularized Inversion Using l_2-Norm

Next moving to explore the developed mode-based inversion scheme and the latest geomagnetic data, the data in terms of SH coefficients from Sec. 4.1 was replaced with a gridded representation of the SV outside the TC from the CHAOS-6-x2 model. For this purpose, an equal-area grid of 20 000 points was first defined on the entire CMB and the polar regions (where the modes of this study may not be a good representation) were then removed which produced a total number of 17 394 grid points between 60°N and S. Radial field SV values were derived at every grid point from, in this test, the CHAOS-6-x2 field model in epoch 2015 which is mostly based on data from the *Swarm* satellite constellation. The uncorrelated and isotropic a priori uncertainty of the SV coefficients in the epoch 2005 of the COV-OBS field model was used again to determine the data error but adjusted by first projecting the uncertainty onto the grid and then, for simplicity, setting all off-diagonal covariances to zero. Hence, the matrix $\mathbf{C}_\mathrm{d}$ was diagonal with a constant value of $4.11 \times 10^6\,(\mathrm{nT/yr})^2$ corresponding to a noise level of around $2\,\mu\mathrm{T/yr}$ at every grid point. This should be compared with a typical signal of $\approx 10\,\mu\mathrm{T/yr}$. Again, a base of geostrophic ($k \leq 20$) and QG inertial modes ($N \leq 10$, $M \leq 16$) containing a total of 180 modes was used. The modes were sorted in $\mathbf{m}$ with increasing spatial complexity i.e., the geostrophic modes with increasing k were followed by the QG-modes arranged in blocks of growing N with increasing M within each block.

The flow structure was regularized using Gillet's l_2-norm (Eq. 3.27) and the regularization parameter was set to the value found in the benchmark test of Sec. 4.1. With

these parameters, the inversion was carried out according to Eq. (3.29) with $\mathbf{d}_{\text{obs}} = \dot{\mathbf{b}}$ and $\mathbf{G} = \mathbf{G}_{\text{grd}}\mathbf{H}_{\text{aug}}$. The results are presented in Fig. 4.2.

The misfit norm $(\mathbf{d}_{\text{prd}} - \mathbf{d}_{\text{obs}})^{\text{T}}\mathbf{C}_{\text{d}}^{-1}(\mathbf{d}_{\text{prd}} - \mathbf{d}_{\text{obs}})$ between the observed and the predicted gridded SV outside the TC is 78 which corresponds to an rms misfit of 136 nT/yr well within the a priori uncertainty of 2 µT/yr on the gridded SV. Gillet et al. (2015b) have argued that such an apparent overfitting is necessary in order to reproduce both changes of length of day and rapid field changes at ground observatories. The estimated flow is again mostly westward-directed with high velocities at mid and low latitudes outside the Pacific region. The overall westward drift of the radial SV is also reflected by the fact that most of the estimated geostrophic mode coefficients are negative. Noteworthy is a localized strong westward flow at the equator, at around 90°W which was not present in epoch 2005. Further, it is noteworthy that alternating radial SV patches are correctly predicted in the northern but not in the southern polar region although they were excluded from the data. The map of the radial SV due to the small-scale error is also given in Fig. 4.2 and shows that more of its power is spatially distributed along 90°E and W meridians. In accordance with the relatively low misfit level, the map of the residuals shows that only little power remains outside the TC. From the SV power spectra at the CMB, it can be also seen that there is consistently less power per harmonic degree in the SV predicted by the small-scale error than in the SV predicted by the estimated flow. Further, note that the decreasing mode amplitude with increasing mode number reflects the effect of the chosen l_2-norm (Eq. 3.27) which suppresses small-scale flows.

4.3. Regularized Inversion Using l_1-Norm

Instead of penalizing the small-scale flow, one can seek a flow that consists of as few non-zero modes as possible by regularizing the inversion with the l_1-norm of the mode coefficients. This way, a simple flow is preferred in the sense that only a small number of modes is needed to represent it.

Similar to the set up in the previous section, gridded SV at 17 394 points outside the TC from CHAOS-6-x2 in epoch 2015 were used with an uncorrelated and isotropic a priori uncertainty of 2 µT/yr. In contrast to the l_2-regularized inversion of Sec. 4.1, in order to implement the l_1-norm, recursive estimation of the mode coefficients was required within an iteratively re-weighted least-squares approach as given in Eq. (3.31) with $\mathbf{d}_{\text{obs}} = \dot{\mathbf{b}}$ and $\mathbf{G} = \mathbf{G}_{\text{grd}}\mathbf{H}_{\text{aug}}$. After tests, a value of $\epsilon = 1 \times 10^{-5}$ was chosen in Ekblom's measure Eq. (3.21). A convergence criterion was adopted that the recursive

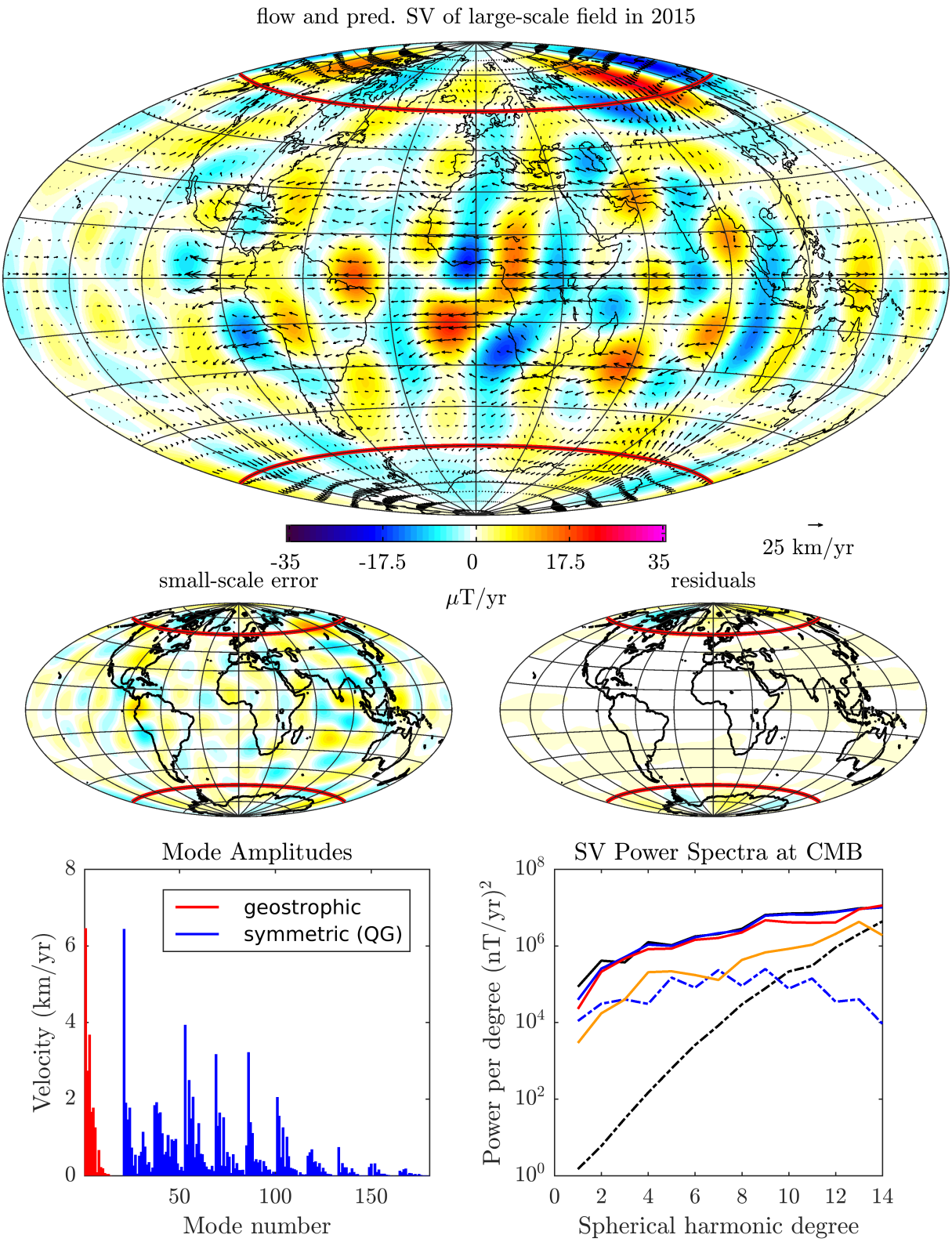

Figure 4.2. Regularized inversion using Gillet's l_2-norm for geostrophic ($k \leq 20$) and QG modes ($N \leq 10$, $M \leq 16$). Top panel: estimated flow at CMB and predicted radial SV due to large-scale field advection in epoch 2015. Middle panel: map of radial SV due to the small-scale error term (left) and radial SV residuals (right). Bottom panel: mode amplitudes (left) and SV power spectra at the CMB (right) showing observed SV derived from CHAOS-6 (black); total predicted SV (blue); predicted SV from large-scale field advection (red); small-scale error (orange); SV residuals (dashed blue); and SV observation uncertainty (dashed black).

estimation was terminated when no model parameter changed more than 0.01 km/yr between successive iterations (see App. A.1 for parts of the MATLAB code).

In the following, the results of the l_1-regularized inversion using three different sets of modes are presented. For each set, two cases are further distinguished which refer to the level of misfit. In the first case, referred to as weakly l_1-regularized, the misfit in epoch 2015 was 136 nT in terms of the rms of the residuals, identical to the l_2-norm inversion presented in Sec. 4.2. In the second case, referred to as strongly l_1-regularized, the misfit in epoch 2015 was chosen three times as high corresponding to an rms residuals of 235 nT/yr.

4.3.1. l_1-Inversion for QG Modes

Similar to the l_2-regularized inversion above, a set of geostrophic ($k \leq 20$) and QG modes ($N \leq 10$, $M \leq 16$) was used to represent the flow. In order to have the same misfit level as for the l_2-norm inversion (Sec. 4.2), the regularization parameter was set to $\lambda = 2.42$. The results are summarized in Fig. 4.3. Probably the most striking difference with the l_2-inversion of Fig. 4.2 is the much rougher westward flow in the equatorial region between 15°N and S. This is due to the increased power in the small-scale flow which is not as strongly damped as before with the l_2-norm (see mode amplitudes). Again, most of the power in the predicted SV comes from the action of the estimated flow on the large-scale field which is higher for every harmonic degree than the contribution of the SV due to the small-scale error term.

In a next step, the regularization parameter was increased to $\lambda = 29.8$ in order to promote to a greater extent a sparse model and a simple flow. The misfit level in epoch 2015 therefore grew to an rms value of 235 nT/yr or three times the previous level (see Fig. 4.4). There is less power in many modes and the overall flow appears very uniformly westward-directed without many small eddies on the CMB. The small-scale error term accounts for most of the spatial structure in the observed SV around the 90°E and W meridians. When looking at the spectrum of the predicted radial SV (Fig. 4.4, bottom right), the power per harmonic degree of the small-scale error is on the same level and similarly distributed as the predicted SV from advecting the large-scale field. Hence, when the flow is stronger regularized, the small-scale error takes most of the predicted SV.

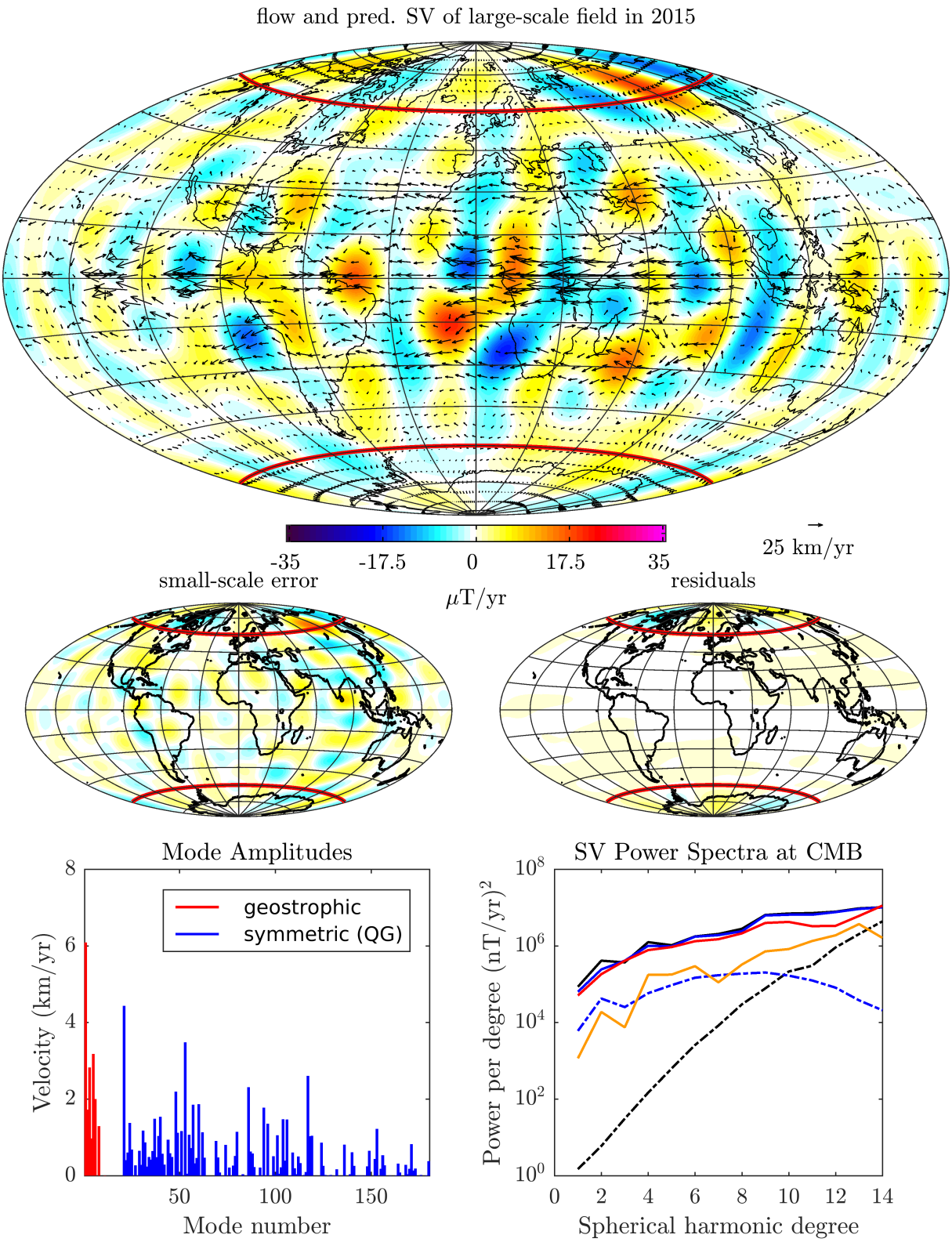

Figure 4.3. Weakly l_1-regularized inversion for geostrophic ($k \leq 20$) and quasi-geostrophic modes ($N \leq 10$, $M \leq 16$). Top panel: estimated flow at CMB and predicted radial SV due to large-scale field advection in epoch 2015. Middle panel: map of radial SV due to the small-scale error term (left) and radial SV residuals (right). Bottom panel: mode amplitudes (left) and SV power spectra at the CMB (right) showing observed SV derived from CHAOS-6 (black); total predicted SV (blue); predicted SV from large-scale field advection (red); small-scale error (orange); SV residuals (dashed blue); and SV observation uncertainty (dashed black).

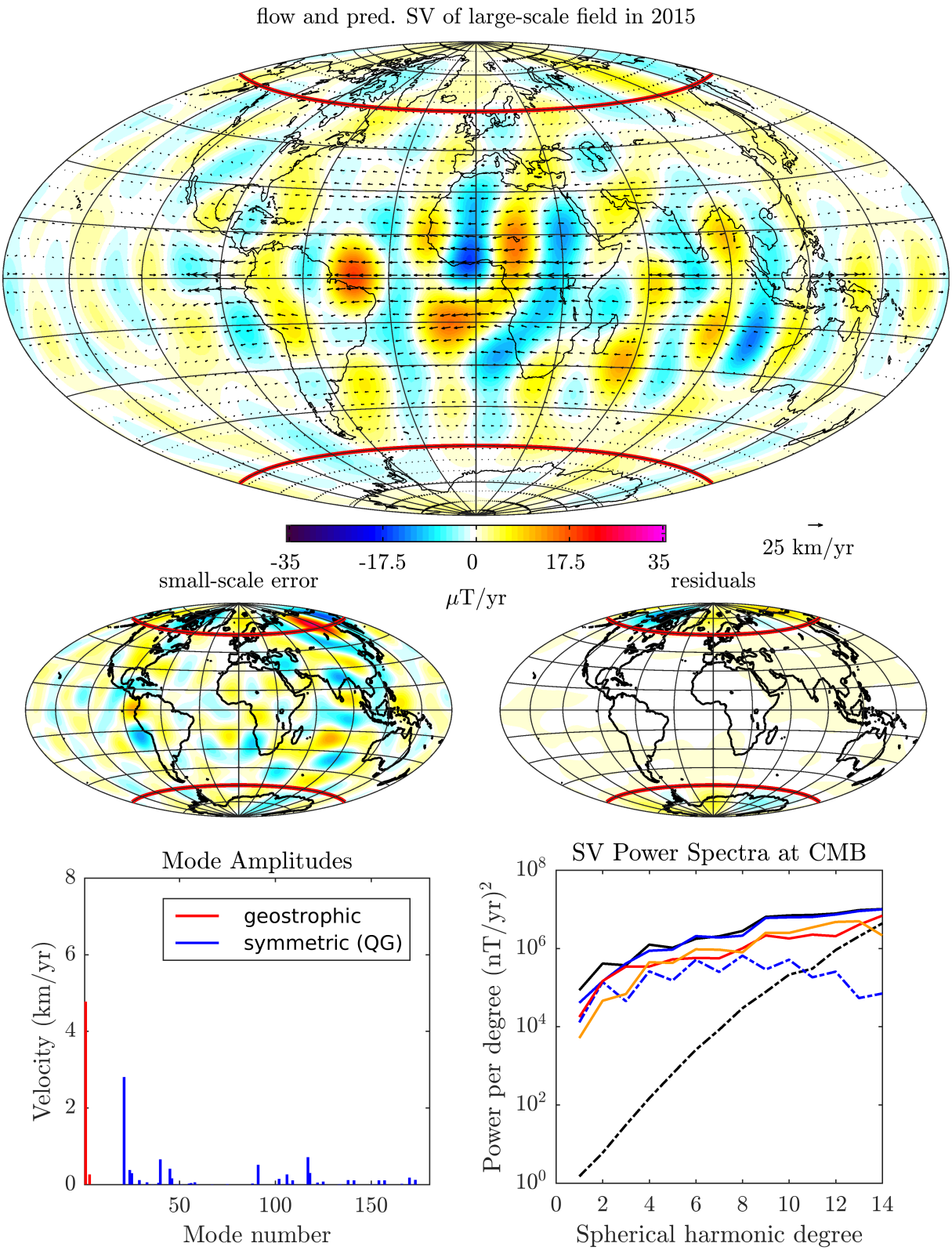

Figure 4.4. Strongly l_1-regularized inversion for geostrophic ($k \leq 20$) and quasi-geostrophic modes ($N \leq 10$, $M \leq 16$). Top panel: estimated flow at CMB and predicted radial SV due to large-scale field advection in epoch 2015. Middle panel: map of radial SV due to the small-scale error term (left) and radial SV residuals (right). Bottom panel: mode amplitudes (left) and SV power spectra at the CMB (right) showing observed SV derived from CHAOS-6 (black); total predicted SV (blue); predicted SV from large-scale field advection (red); small-scale error (orange); SV residuals (dashed blue); and SV observation uncertainty (dashed black).

4.3.2. l_1-Inversion for Symmetric Modes

The basis of modes was next extended to include all symmetric modes (note this also includes the QG modes from the previous inversion) with $N \leq 10$ and $M \leq 16$. Together with the 20 geostrophic modes, the number of modes increased to 1780 which corresponded to 3540 mode coefficients that needed to be estimated in the model vector. The regularization parameter was again chosen to give an rms misfit of 136 nT/yr for the weakly regularized case or 235 nT/yr for the strongly regularized case in epoch 2015.

Fig. 4.5 shows the weakly-regularized case for which $\lambda = 24.9$ was chosen. The estimated flow is mostly going to the west and spatially smooth in a broad band around the equator between 30°N and S as opposed to the case of using QG modes only (Sec. 4.3.1). Note also that the flow pattern that is possibly associated with an eccentric planetary-scale gyre is hardly visible and of secondary importance when compared to the strong flow at the equator. There are a few modes whose amplitudes stand out but are not the QG modes. This shows that the algorithm does not prefer the QG modes over more general symmetric modes if given the freedom. Fig. 4.6 summarizes the results of a stronger l_1-regularized inversion using $\lambda = 76.2$. Again, the increased regularization decreases the mode amplitudes and causes increased power in the small-scale error.

4.3.3. l_1-Inversion for Symmetric and Antisymmetric Modes

Going further, the antisymmetric modes were included. This type of inertial modes breaks the formerly imposed equatorial symmetry expected for rapidly-rotating flow and results in a flow that is allowed to cross the equator. Relaxing the symmetry constraint is also tested by Baerenzung et al. (2014) who, based on the findings of their probabilistic core surface flow inversion, suggest that deviations from a quasi-geostrophic assumption should be allowed to occur.

Using all types of inertial modes, the base for the flow included geostrophic ($k \leq 20$), symmetric ($N \leq 10$, $M \leq 16$) and antisymmetric modes ($N \leq 10$, $M \leq 16$). In total 7412 mode coefficients of 3716 modes had to be estimated. Again, the misfit level was fixed to 136 nT/yr and 235 nT/yr for the two inversions which translated to $\lambda = 34.1$ in the first and $\lambda = 86.6$ in the second case. Fig. 4.7 and Fig. 4.8 give an overview of the inversion results. Low latitudes show a westward flow around the Atlantic sector but the amplitude of the flow is in general much smaller than in the previous cases of using a small number of modes. Baerenzung et al. (2014) obtained with their probabilistic approach a spatially smooth flow in epoch 2005 that also crossed the equator south of India and

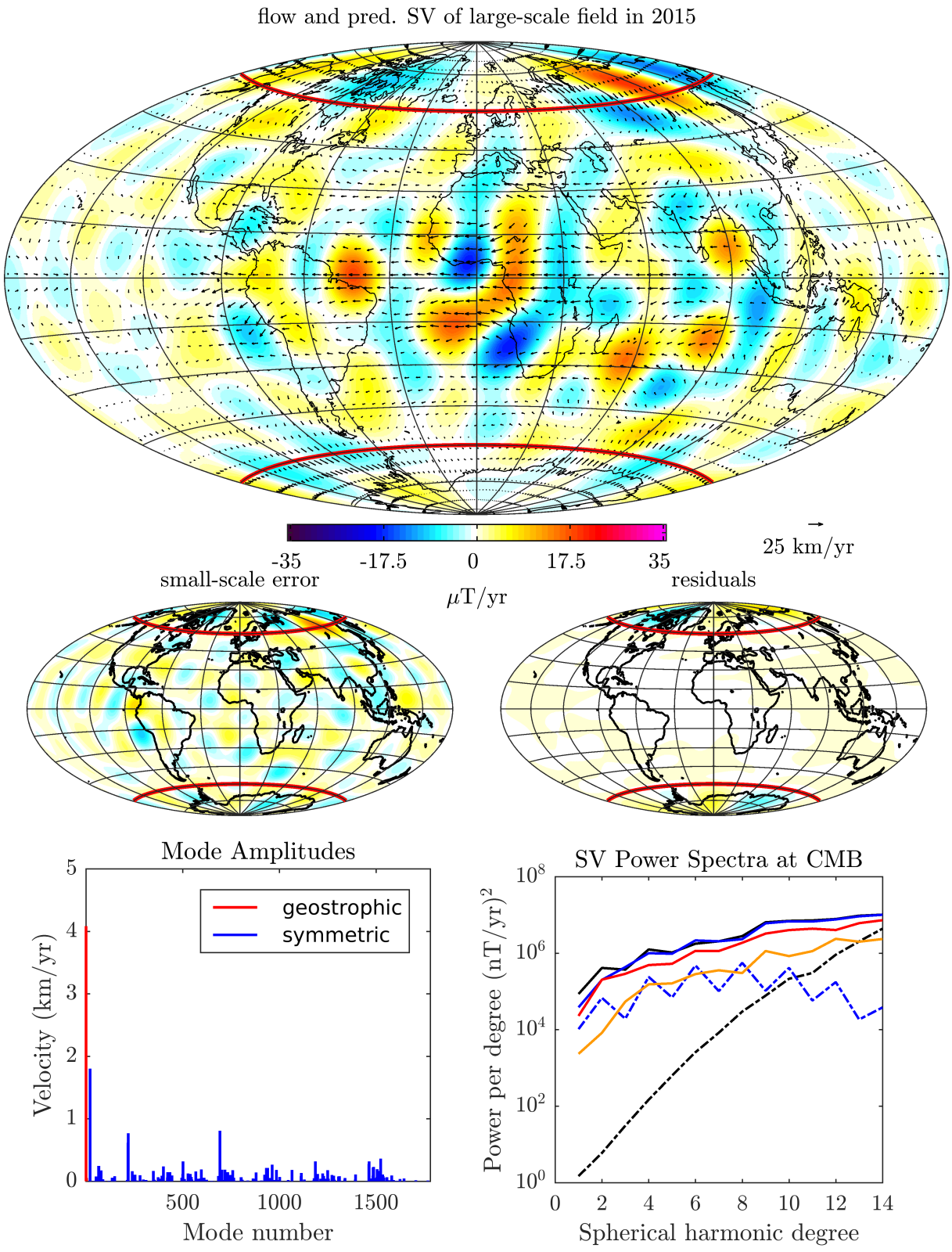

Figure 4.5. Weakly l_1-regularized inversion for geostrophic ($k \leq 20$) and symmetric modes ($N \leq 10$, $M \leq 16$). Top panel: estimated flow at CMB and predicted radial SV due to large-scale field advection in epoch 2015. Middle panel: map of radial SV due to the small-scale error term (left) and radial SV residuals (right). Bottom panel: mode amplitudes (left) and SV power spectra at the CMB (right) showing observed SV derived from CHAOS-6 (black); total predicted SV (blue); predicted SV from large-scale field advection (red); small-scale error (orange); SV residuals (dashed blue); and SV observation uncertainty (dashed black).

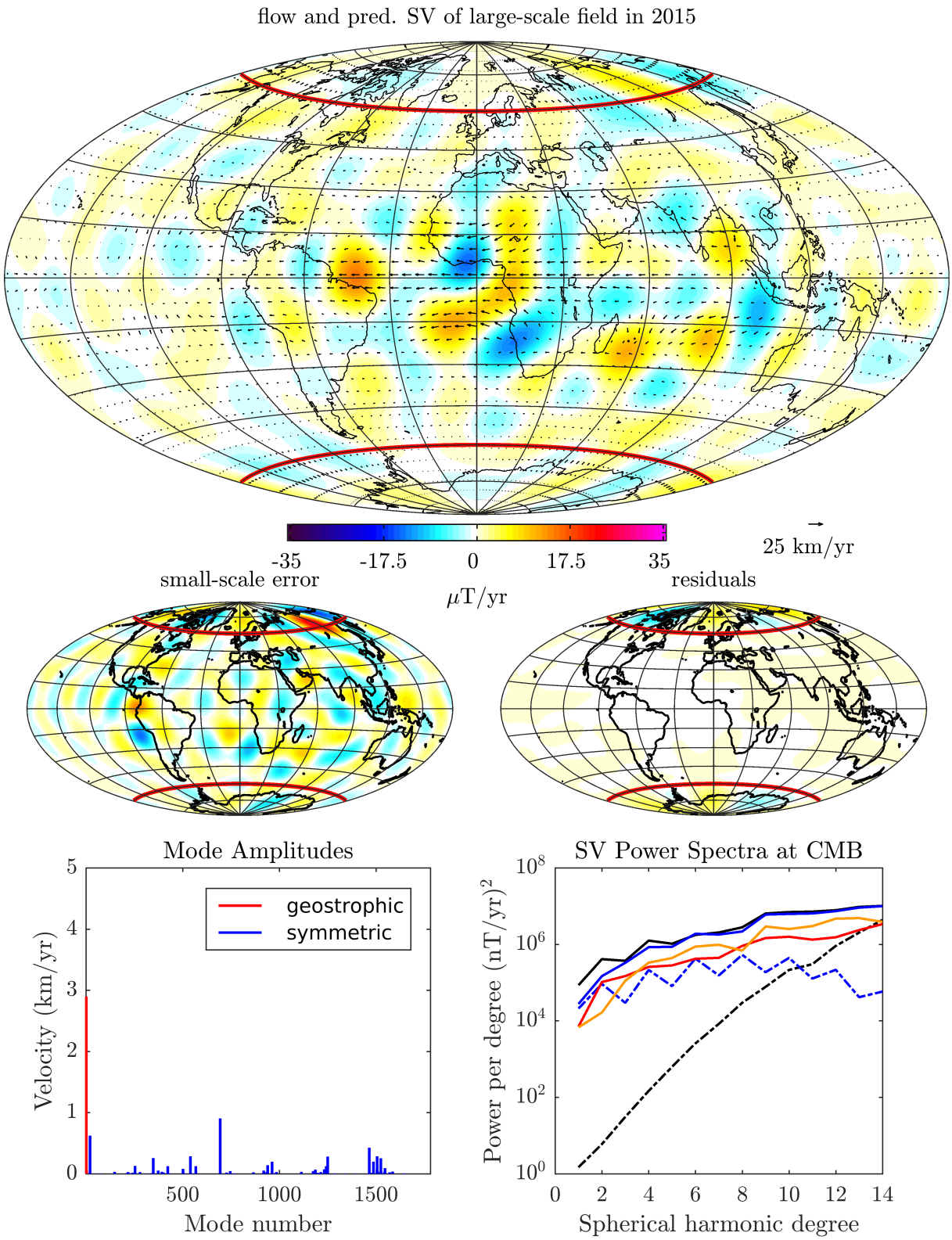

Figure 4.6. Strongly l_1-regularized inversion for geostrophic ($k \leq 20$) and symmetric modes ($N \leq 10$, $M \leq 16$). Top panel: estimated flow at CMB and predicted radial SV due to large-scale field advection in epoch 2015. Middle panel: map of radial SV due to the small-scale error term (left) and radial SV residuals (right). Bottom panel: mode amplitudes (left) and SV power spectra at the CMB (right) showing observed SV derived from CHAOS-6 (black); total predicted SV (blue); predicted SV from large-scale field advection (red); small-scale error (orange); SV residuals (dashed blue); and SV observation uncertainty (dashed black).

featured a large intensity of westward drift in the Southern Hemisphere. In this study, a strong and large-scale flow across the equator is not found at any epoch covered by CHAOS-6, however, the equatorial symmetry is clearly broken as seen by the power in the small-scale antisymmetric modes and for example in the Atlantic ocean southwest of Africa (see Fig. 4.7, top).

4.4. Flow Time-Dependence of the Inferred Core Flows

The geomagnetic field model CHAOS-6-x2 covers the time period from 1999 to 2017 and the approach developed above can be therefore used to study how the estimated flow changes through time. The approach here consists of simply estimating snapshots of the model vector at different epochs between 1999 and 2017 using the l_1-regularized inversion of the three sets of modes presented in the previous section. First, the regularization parameter was fixed to give a misfit of 136 nT/yr in epoch 2015 and then the whole inversion algorithm was repeatedly executed while computing the SV and the core field from the CHAOS-6-x2 geomagnetic field model at equally-spaced epochs within the considered time period. The spacing was chosen to be 0.5 years. After all snapshots had been evaluated, a cubic spline interpolation of the mode amplitudes was constructed. The interpolation could then be further used to evaluate means over the time interval and LOD changes (see Eq. 4.3) by taking time-derivatives. It should be kept in mind that this approach is very different from the time-dependent core flow inversion performed by Gillet et al. (2015b) since temporal correlations are not accounted for. Nonetheless, it was hoped to identify modes that are relevant for the time-dependence of the core flow and it also offered an opportunity to independently test the geostrophic part of the estimated flow with the help of length of day (LOD) predictions.

4.4.1. Predictions for LOD Changes

Earth's rotation period or LOD is not constant with 86 000 s but varies over days to millennia due to changes of its angular momentum caused by external torques and the interaction between different parts of the Earth system (Holme, 2015). This variation can be attributed to different sources such as the gravitational pull of the sun and the moon which cause a slowing down of currently 1.4 ms per century. Wind and ocean circulations also affect the rotation rate but on shorter, yearly or subyearly timescales. Further it was realized that the core takes up angular momentum and thus changes the observed LOD. Jackson et al. (1993) derived an expression to link changes of zonal toroidal motions with

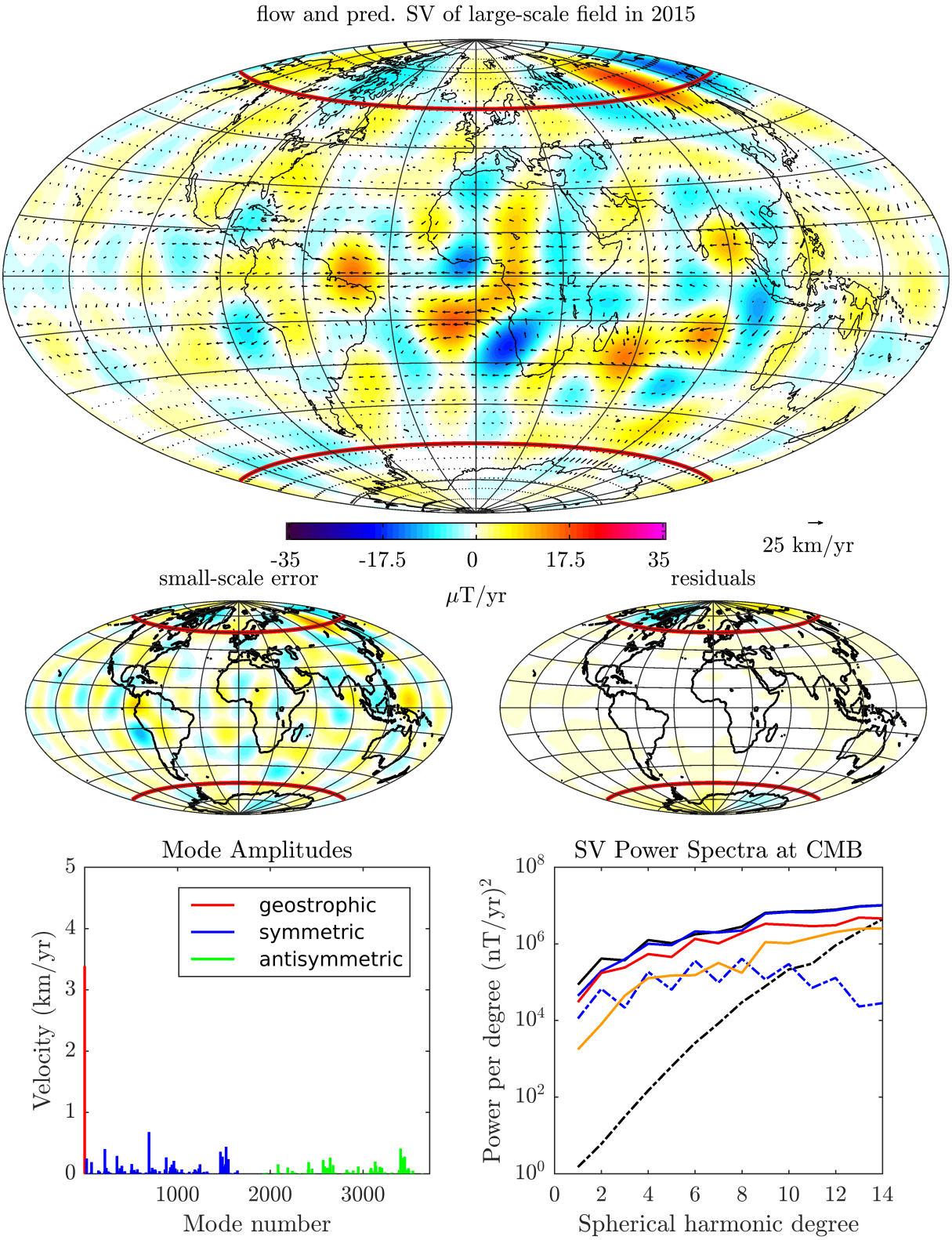

Figure 4.7. Weakly l_1-regularized inversion for geostrophic ($k \leq 20$), symmetric ($N \leq 10$, $M \leq 16$) and antisymmetric modes ($N \leq 10$, $M \leq 16$). Top panel: estimated flow at CMB and predicted radial SV due to large-scale field advection in epoch 2015. Middle panel: map of radial SV due to the small-scale error term (left) and radial SV residuals (right). Bottom panel: mode amplitudes (left) and SV power spectra at the CMB (right) showing observed SV derived from CHAOS-6 (black); total predicted SV (blue); predicted SV from large-scale field advection (red); small-scale error (orange); SV residuals (dashed blue); and SV observation uncertainty (dashed black).

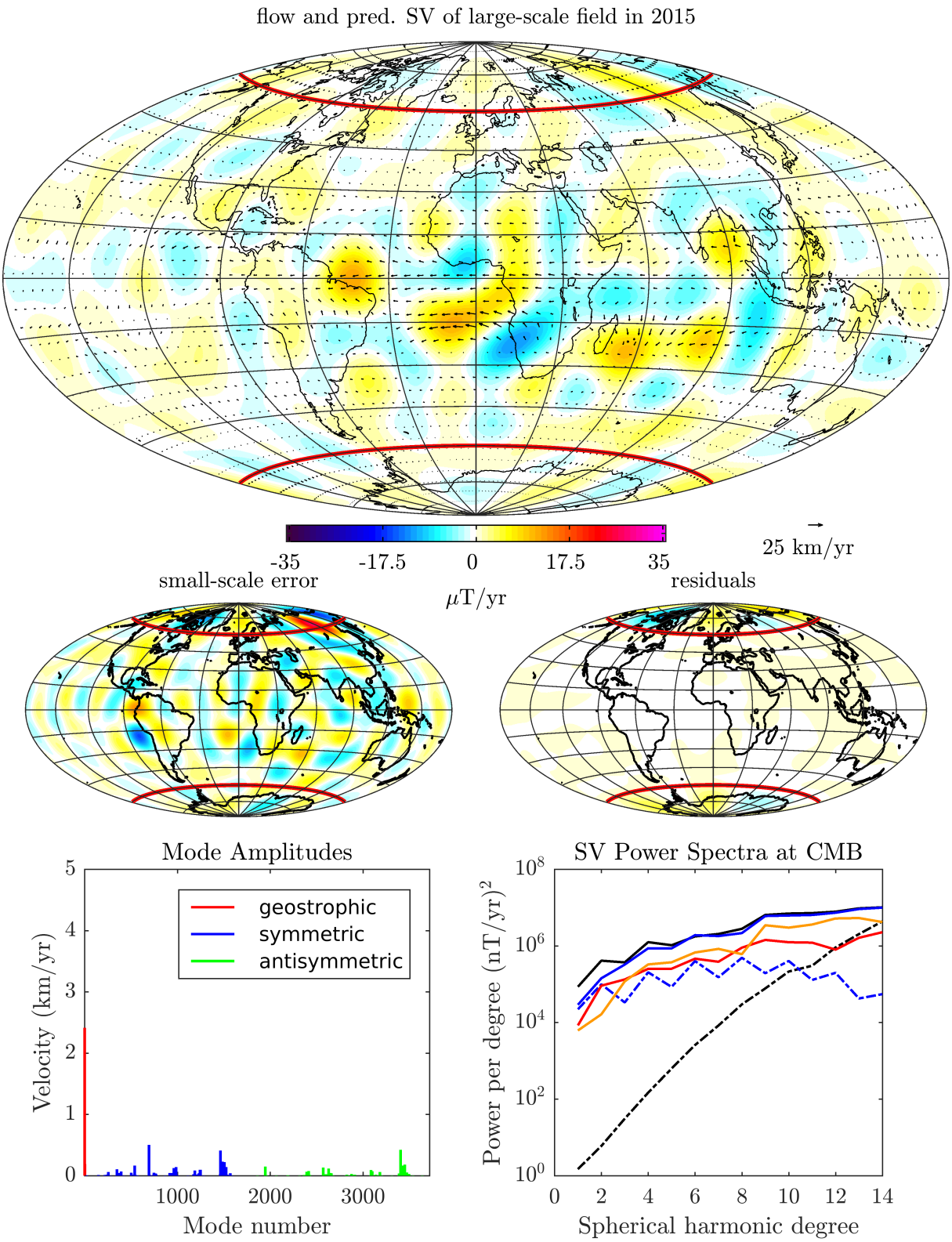

Figure 4.8. Strongly L_1-regularized inversion for geostrophic ($k \leq 20$), symmetric ($N \leq 10$, $M \leq 16$) and antisymmetric modes ($N \leq 10$, $M \leq 16$). Top panel: estimated flow at CMB and predicted radial SV due to large-scale field advection in epoch 2015. Middle panel: map of radial SV due to the small-scale error term (left) and radial SV residuals (right). Bottom panel: mode amplitudes (left) and SV power spectra at the CMB (right) showing observed SV derived from CHAOS-6 (black); total predicted SV (blue); predicted SV from large-scale field advection (red); small-scale error (orange); SV residuals (dashed blue); and SV observation uncertainty (dashed black).

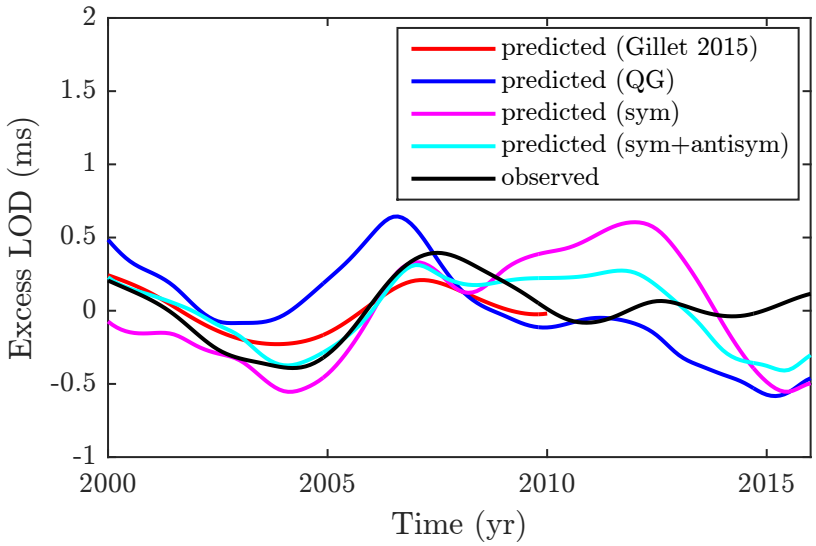

Figure 4.9. Predicted and observed excess LOD corrected for atmospheric dynamics, tidal signal and tidal braking. The individual graphs of the excess LOD were made offset-free by removing the respective time-averages.

changes of LOD. In particular, only two toroidal expansion coefficients are required in (Jackson et al., 1993)

$$\Delta T = 1.138 \frac{\text{ms}}{\text{km} \cdot \text{yr}^{-1}} \left(\Delta t_1^{0c} + \frac{12}{7} \Delta t_3^{0c} \right), \tag{4.3}$$

where the change of LOD, ΔT, is measured in ms and the toroidal coefficients under the Schmidt quasi-normalization in km/yr. With this equation, changes of LOD can be predicted and tested against observed LOD from which signals of sources other than the core have been removed. In particular, the observed LOD was corrected by removing the contribution of atmospheric dynamics and model predictions of the tidal signal from the solid Earth (Gillet et al., 2015b). Further, the slowing down of 1.4 ms/cy due to tidal braking was subtracted. Fig. 4.9 shows the corrected observed excess LOD together with the predictions of the weakly l_1-regularized inversions of this study and Gillet et al. (2015b) (until 2010). Especially in the first half of the considered time period, the predicted LOD agrees well with the observations. However in the second half, the predictions start to deviate more. The lack of satellite data in 2010-2013 might explain the departures of the predicted LOD from the observed LOD during this time. Following Gillet et al. (2015b), the ratio between the rms values of observed and predicted LOD, calculated over the considered time period, can be used to measure the impact of the model choice. The statistic is given by (Gillet et al., 2015b)

$$\mathcal{L}_\gamma = \left(\int (\gamma_{\text{obs}} - \hat{\gamma}_{\text{obs}})^2 \text{d}t \right)^{-1} \int (\gamma_{\text{prd}} - \hat{\gamma}_{\text{prd}})^2 \text{d}t, \tag{4.4}$$

where γ is the observed or predicted LOD and $\hat{\gamma}$ denotes its time-average. The integration was replaced with a summation of discrete values from epoch 2000 to 2016. Values for $\mathcal{L}_\gamma$ were found to be 2.26 in the case of QG modes, 3.13 for all symmetric modes and 1.27 when the antisymmetric modes were also included. Gillet et al. (2015b) found for a value of 1.34 for this measure.

As could be seen in the previous sections, there is a great variety of results that can be produced by choosing different sets of geostrophic and inertial modes to represent the flow. In the following, only results from the l_1-inversion for QG modes are presented. They give the most restrictive basis and are important because they represent the expected core dynamics.

4.4.2. Mode Time-Dependence

First, the mode amplitudes and accelerations for the 180 geostrophic and QG modes are considered. The amplitude of a single mode, which is equivalent to a velocity, for a given N and M was formed by taking the square root of the sum of the squared mode coefficients, corresponding to the sine and cosine constituents in longitude. The acceleration amplitude was calculated essentially the same way except that the time-derivative of the spline-interpolated coefficients was used.

Fig. 4.10 shows the rms of the mode amplitude and the acceleration amplitude calculated over the epochs from 2000 to 2016. Most of the modes have rms amplitudes below 2 km/yr that gradually decrease towards high mode numbers, which are associated with small-scale flows. Noteworthy is a small number of modes which have high amplitudes. For example, the first mode, which corresponds to the geostrophic mode with $k = 1$, shows the highest amplitude with 5.8 km/yr. In case of the acceleration, most of the modes have averages below 0.2 km/yr^2. Besides the geostrophic mode with $k = 1$, there are in particular four QG modes that have high rms amplitudes. The time-dependence of the amplitudes and the acceleration amplitudes for these modes is shown in Fig. 4.11. The last two modes of the selection, ($N = 5$, $M = 2$) and ($N = 7$, $M = 3$), are also the ones which experience the highest rms acceleration in the considered period. The shown mode amplitudes do not change uniformly but have short period oscillations of a few years superimposed on the long timescale trend. Further it seems that the modes in Fig. 4.11 undergo quite distinct changes in time. In order to get a better understanding of the spatial appearance of the QG modes, maps of the meridional plane and the CMB are shown in Fig. 4.12. The geostrophic mode with $k = 1$ is characterized by a zonal flow with a maximum velocity at the equator and zero velocity at the poles. The QG

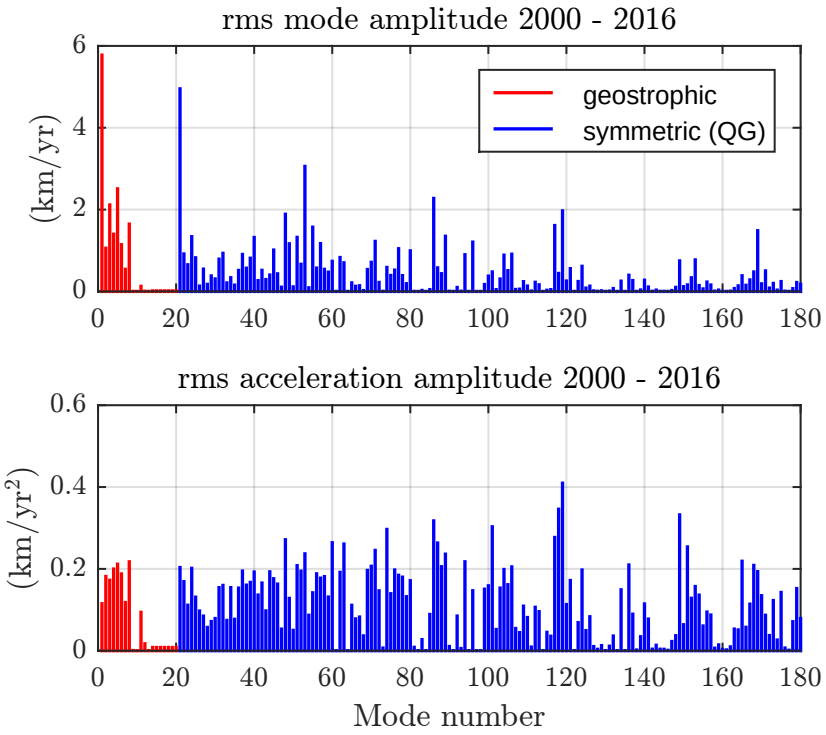

Figure 4.10. Rms velocity and acceleration amplitudes of geostrophic ($k \leq 20$) and QG modes ($N \leq 10$, $M \leq 16$).

modes with high wavenumber strongly contribute to the core surface velocity at mid and low latitudes in the form of non-axisymmetric azimuthal flow. Note that the QG mode with $N = 1$ and $M = 1$ has the second largest rms amplitude which is interesting since it allows large-scale flows that are similar to the planetary-scale eccentric gyre, interpreted by other authors.

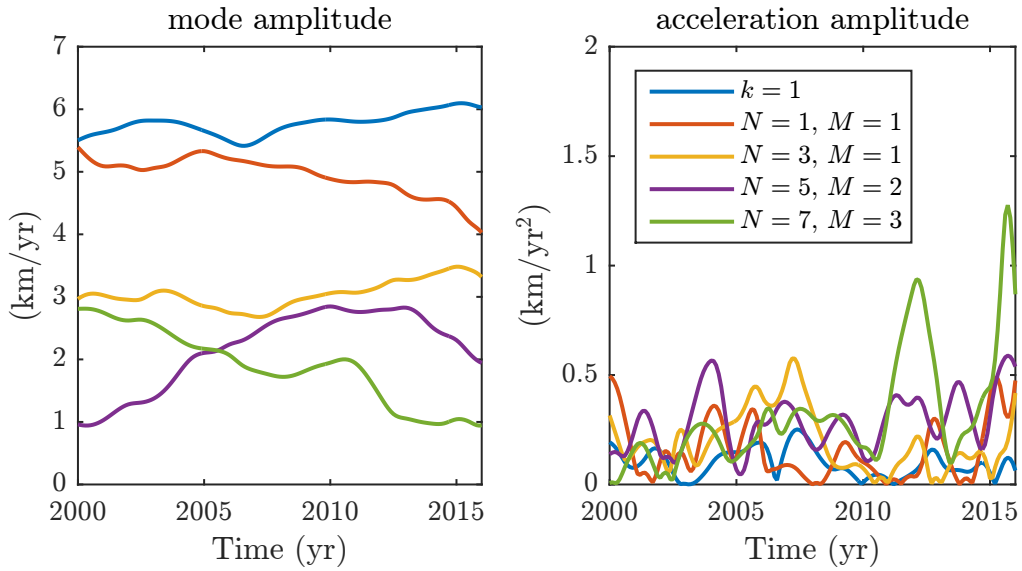

Figure 4.11. Mode and acceleration amplitude of the first geostrophic and four QG modes which have the highest rms amplitude over the period from 2000 to 2016.

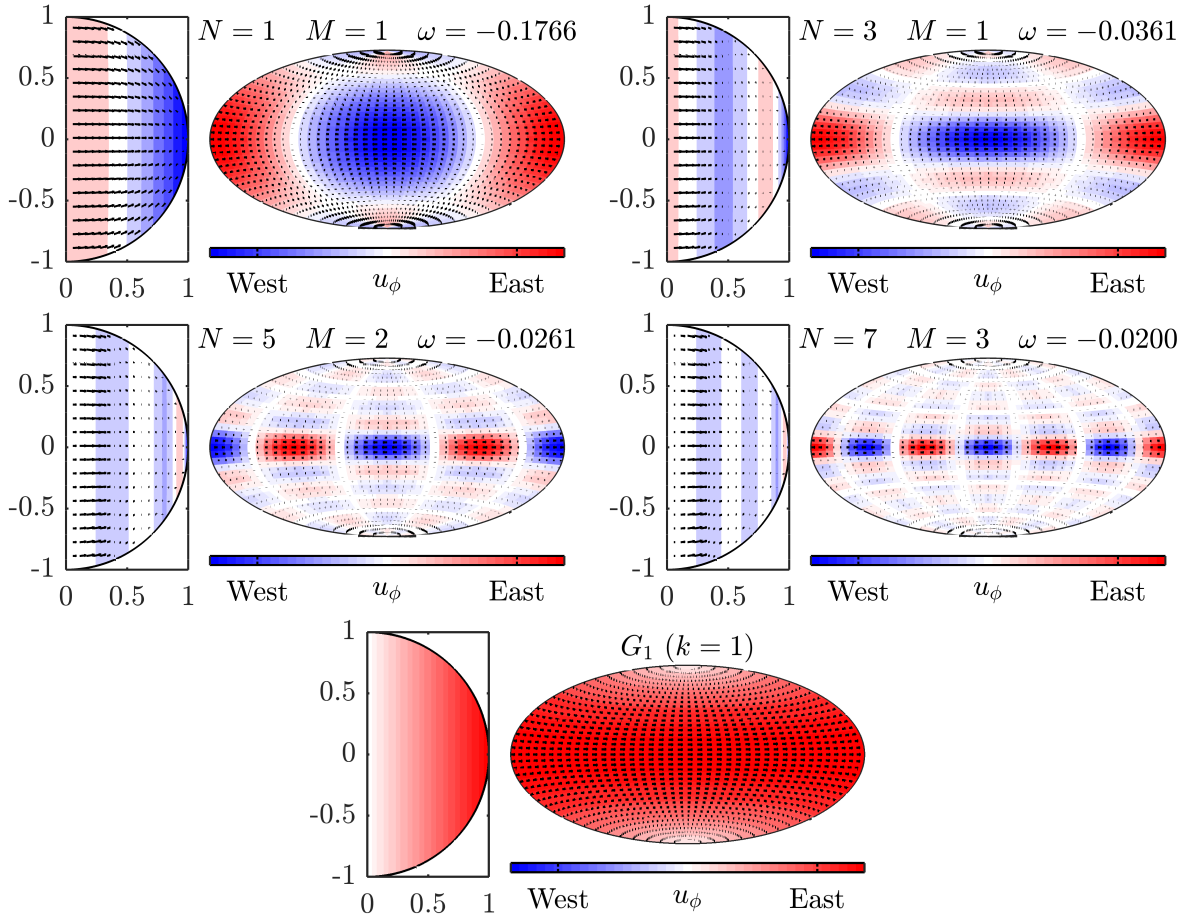

Figure 4.12. Maps of the meridional plane and CMB (left and right in each panel) of the QG mode and the first geostrophic mode with the five highest rms mode amplitudes in 2000-2016.

5. Discussion

A number of interesting aspects of the inversion results presented in Ch. 4 are chosen here for further discussion. First, the flow in mid and low latitudes is examined in detail to see if they can account for SA pulses associated with geomagnetic jerks (Sec. 5.1). Second, it is considered whether the l_1-regularized models can be further reduced to give a simple description of the flow in terms of a subset of chosen modes (Sec. 5.2), and third, the impact of the small-scale error parametrization is discussed (Sec. 5.3). Finally, the prospect of moving to a probabilistic approach, to better describe the range of possible flows, is briefly presented and discussed (Sec. 5.4).

5.1. The Origin of Geomagnetic Jerks and Secular Acceleration Pulses

An important question is whether l_1-regularized models can provide new insights into the dynamics of the flow in mid and low latitudes. A better understanding of the core flow is in particular of interest for the study of geomagnetic jerks and related SA pulses (see Ch. 1).

Fig. 5.2 shows the SA calculated from the CHAOS-6-x2 model in epochs 2006, 2009 and 2013 when SA pulses peaked. The pulses in epoch 2006 and 2009 are clearly visible at the core surface in form of three patches of increased SA in the Atlantic sector which are similar but have changing polarity. In epoch 2013 the SA patches appear again with the same polarity as in 2006 but are slightly shifted to the west. Fig. 5.2 shows the SA that is generated by the time-dependent estimated l_1-norm QG flow at the same epochs. Again, patches of increased SA appear in the Atlantic sector, similar to those in Fig. 5.1. It was found that much more power was contained in the QG flow and not in the small-scale error. When all symmetric and antisymmetric modes are modeled, the SA pulses are mostly explained by the small-scale error term, suggesting problems with its use in those cases. Fig. 5.2 also shows the acceleration of the modeled QG flow. Especially in the

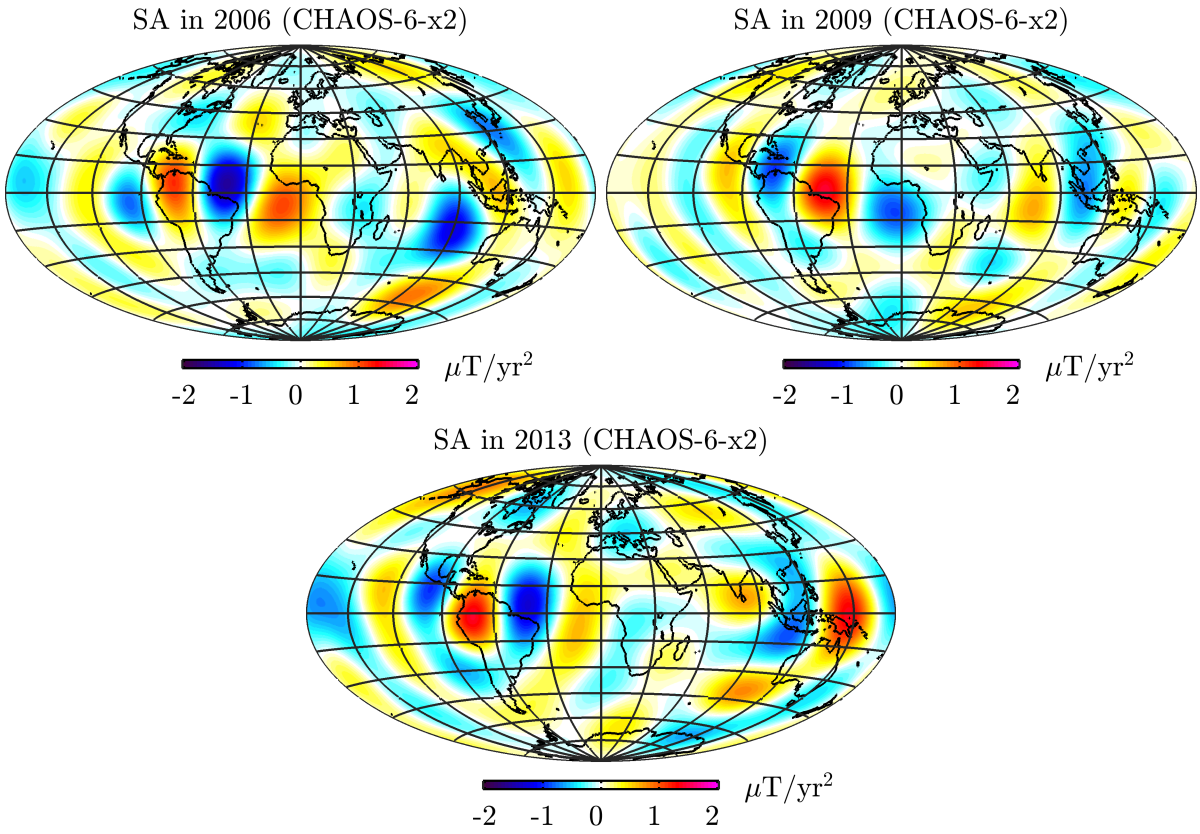

Figure 5.1. Secular acceleration (SA) at the core surface (degree 1 to 8 only) calculated from CHAOS-6-x2 model.

epochs 2006 and 2013, there is strong acceleration in azimuthal direction at around 40°W at the Equator. The result in Fig. 5.2 support the hypothesis of Finlay et al. (2016), that the time-dependence of the azimuthal flow at 40°W at the Equator is responsible for SA pulses at that location.

A possible improvement of the method might be achieved by solving for a steady background flow using symmetric and antisymmetric modes, while allowing time-dependence of certain geostrophic and QG modes.

5.2. A Reduced QG Mode Model

In this study, the flow at the core surface has been parametrized in terms of geostrophic and inertial modes. The regularization in the inverse problem with an l_1-norm resulted in models which were characterized by a relatively small number of modes having high amplitudes and time-dependence. One can ask the question whether a subset of modes could be selected that would still be able to explain the data reasonably well, and capture

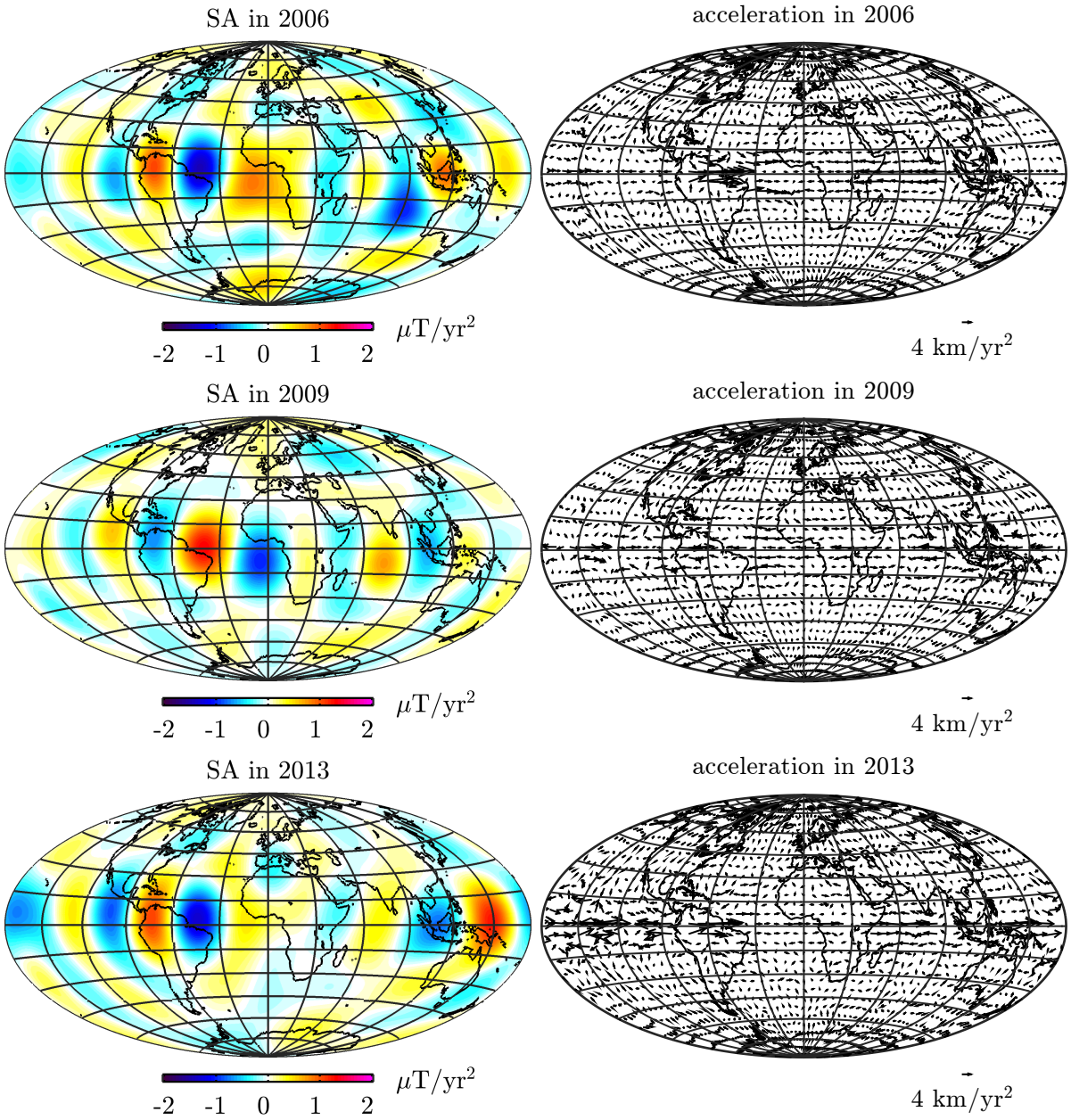

Figure 5.2. Left: Secular acceleration (SA) at the core surface (degree 1 to 8 only) predicted by the effect of the QG flow on the large-scale magnetic field in epoch 2006, 2009 and 2013. Right: acceleration of the QG flow at the same epochs. The l_1-norm was used to regularize the flow (see Sec. 4.3.1, weakly regularized).

the crucial time-dependence.

A first attempt to do this involved increasing the regularization parameter in the l_1-inversion algorithm. However, this severely decreased many of the mode amplitudes which was not desired. An alternative approach was therefore explored, taking the solution of a weakly l_1-regularized inversion using QG modes and selecting a subset of 21 modes which showed large rms mode amplitude and mode acceleration amplitude over the considered

time period. These were chosen as a reduced basis which was then used in a un-regularized (for the flow) least-squares approach to fit the data while still co-estimating the SV due to the unresolved small-scales. The misfit level was found to be twice that of the original model and the flow was found to be mostly azimuthal without many pronounced vortices (Fig. 5.3). Also, it was found to overpredict the amplitude of LOD changes by a factor of two and gave $\mathcal{L}_\gamma = 23$ (see Sec. 4.4.1). These observations suggest that the performance of this reduced model is less good compared to other l_1-regularized models of this study, although this might also be expected given the smaller number of model parameters. The manner of choosing the modes for the reduced model should also be reconsidered since it was rather crude and might not correctly identify the modes that are important for the flow structure and its time-dependence. However, it is interesting to see that the reduced model still catches the SA pulses in Fig. 5.1, only slightly less pronounced.

5.3. Impact of the Parametrization of the Small-Scale Error Term

All lengthscales of the magnetic field at the core surface contribute to the observable large-scale SV by interacting with the core surface flow. The fact that the small-scale magnetic field is unknown necessarily leads to the a small-scale error term (Eq. 3.5) which significantly impacts the ability to infer meaningful core flows from SV observations. A serious inversion for the flow needs to take the bias due to small-scale errors into account.

This study adopts an augmented state approach which allows the small-scale error to be co-estimated along with the flow. The implementation requires a covariance matrix of the small-scale error in order to specify a priori information on the expected variance and spatial correlations of the small-scale error. A further shortcoming of the present study is that temporal correlations of the error has not been addressed although their importance has been pointed out by Gillet et al. (2015b). Here, a covariance matrix from a geodynamo calculation Barrois et al., 2017 has been used. Although a reasonable start, this is not formally consistent with the large-scale flow estimated. In future studies, experiments with the estimated flow acting on small scales consistent with the geomagnetic spectrum could be performed and the covariance matrix $\mathbf{C}_\mathrm{e}$ iteratively updated. A more complete approach such as the one presented by Gillet et al. (2015b), however, was beyond the scope of this study. The presented approach is therefore considered as a first attempt to account for the small-scale error in the core flow inversion.

With the augmented state approach, it was found that the small-scale error can have

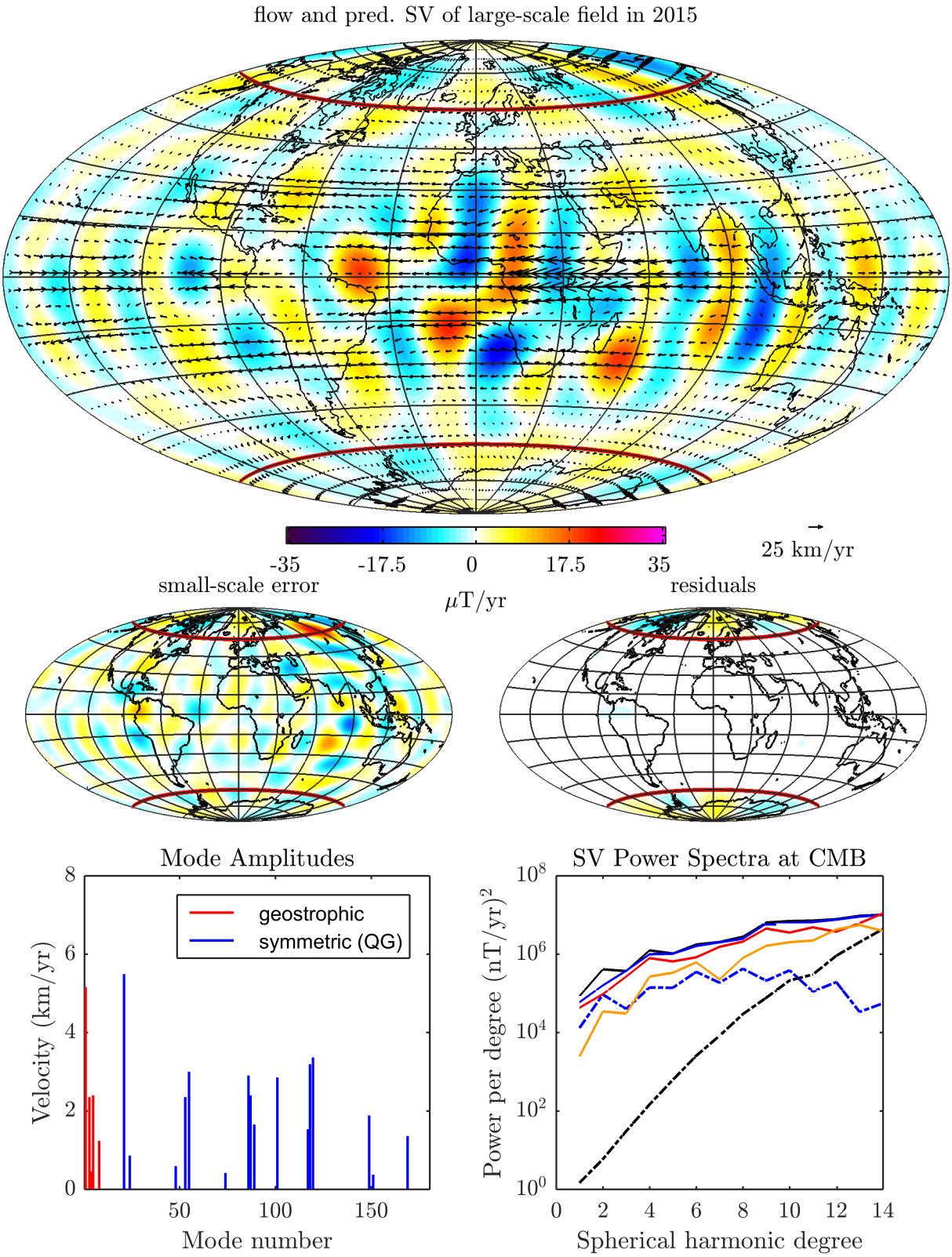

Figure 5.3. A reduced model for a subset of geostrophic and QG modes. Top panel: estimated flow at CMB and predicted radial SV due to large-scale field advection in epoch 2015. Middle panel: map of radial SV due to the small-scale error term (left) and radial SV residuals (right). Bottom panel: mode amplitudes (left) and SV power spectra at the CMB (right) showing observed SV derived from CHAOS-6 (black); total predicted SV (blue); predicted SV from large-scale field advection (red); small-scale error (orange); SV residuals (dashed blue); and SV observation uncertainty (dashed black).

a significant effect on both the flow structure and the level of misfit. This can be seen for example, when the core flow is estimated without including the small-scale error. If the level of misfit is to be maintained, then the regularization of the flow has to be reduced. This yields stronger and more complex flows. In other words, if the small-scale error is included then the regularization parameter can be increased, reducing the power in the flow. Fig. 5.4 shows an l_1-regularized model based on geostrophic, symmetric and antisymmetric modes having the same misfit as the model in Fig. 4.7 but without including the small scale error term. Ideally, the misfit level is set equal to the observational error. In this study however, such a misfit level regularized the flow to an unacceptable level at which most of the observed SV power was modeled by the small-scale error and not by the action of the flow on the large-scale magnetic field. Therefore, the regularization parameter was initially selected based on a high correlation factor between the modeled flow here and that one derived in the more complete study by Gillet et al. (2015b), where LOD changes and rapid SV changes were fit. A better approach would be to directly fit to satellite and ground-based data rather than a field model, since better error estimates are available for such data.

5.4. Towards a Probabilistic Inversion

The inverse problem studied here is highly non-unique and has many solutions that are consistent with the data. In this thesis, this was dealt with by minimizing a cost function Φ including a norm of the model which penalizes undesired features. For example, Gillet's l_2-norm penalizes small-scales in favor of large-scale flows, while the l_1-norm penalized large mode amplitudes.

This approach has major limitations. An alternative is to adopt a probabilistic point of view where the inverse problem and all its components are defined in terms of probability density functions. The solution is then given as posterior probability density of the model $\sigma(\mathbf{m})$, which summarizes all the available information of the physical system and the prior information on the data as well as the model. This is often stated as (Tarantola, 2005)

$$\sigma(\mathbf{m}) = cL(\mathbf{m})\rho(\mathbf{m}), \tag{5.1}$$

where c is a normalization constant, $L(\mathbf{m})$ is the likelihood probability density and $\rho(\mathbf{m})$ the prior probability density of the model. $L(\mathbf{m})$ gives a measure of how well the model explains the data whereas $\rho(\mathbf{m})$ encodes prior information concerning the model often in form of specific assumptions. In particular for a linearized and explicit inverse problem with $\mathbf{d}_{\text{obs}} = \mathbf{Gm}$ and constant $\mathbf{G}$ and considering Gaussian distributions for the expected

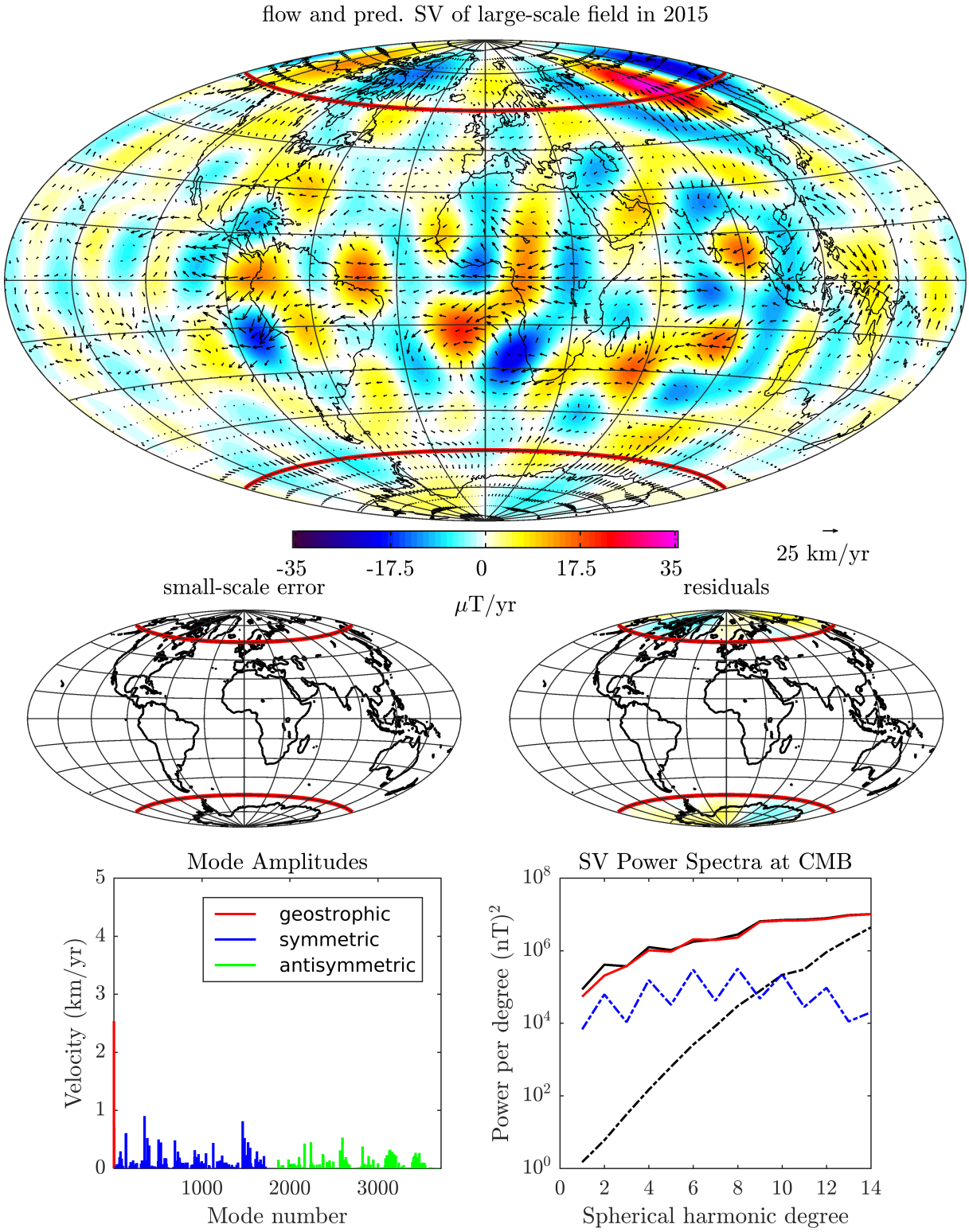

Figure 5.4. l_1-regularized inversion for geostrophic ($k \leq 20$), symmetric ($N \leq 10$, $M \leq 16$) and antisymmetric modes ($N \leq 10$, $M \leq 16$) without including the small-scale error term. Top panel: estimated flow at CMB and predicted radial SV due to large-scale field advection in epoch 2015. Middle panel: map of radial SV due to the small-scale error term (left) and radial SV residuals (right). Bottom panel: mode amplitudes (left) and SV power spectra at the CMB (right) showing observed SV derived from CHAOS-6 (black); predicted SV from large-scale field advection (red); SV residuals (dashed blue); and SV observation uncertainty (dashed black).

error and the prior model, these quantities can be written as (Mosegaard and Rygaard-Hjalsted, 1999)

$$
\begin{aligned}
L(\mathbf{m}) &\propto \exp\left(-\frac{1}{2}(\mathbf{d}_{\text{obs}} - \mathbf{G}\mathbf{m})^{\mathrm{T}}\mathbf{C}_{\text{d}}^{-1}(\mathbf{d}_{\text{obs}} - \mathbf{G}\mathbf{m})\right) \\
\rho(\mathbf{m}) &\propto \exp\left(-\frac{1}{2}\mathrm{m}^{\mathrm{T}}\mathbf{R}\mathrm{m}\right).
\end{aligned}
\tag{5.2}
$$

Note the analogy to the previous formulation of the inverse problem in terms of the cost function (Eq. 3.16). There, the misfit was measured with $(\mathbf{d}_{\text{obs}} - \mathbf{G}\mathbf{m})^{\mathrm{T}}\mathbf{C}_{\text{d}}^{-1}(\mathbf{d}_{\text{obs}} - \mathbf{G}\mathbf{m})$ and appears now in the Likelihood probability density. Similarly, the regularization, which is controlled by $\mathbf{R}$, provides an expression for the prior knowledge on the model and is equivalent to the inverse of the covariance matrix $\mathbf{C}_{\text{m}} = \mathbf{R}^{-1}$. Indeed, by regularizing small-scale flows, a prior information on the model is effectively specified. In the probabilistic framework, the posterior $\sigma(\mathbf{m})$ can be obtained analytically for Gaussian $L(\mathbf{m})$ and $\rho(\mathbf{m})$ or for complex priors sampled via a Markov chain Monte Carlo (MCMC) algorithm (see e.g. Mosegaard and Tarantola, 1995). Various statistics to characterize the distribution can be then derived from the collection of samples. In the case of Gaussian-distributed Likelihood and a priori information as in Eq. (5.2), the algorithm used in this study (Eq. 3.29), provides a model estimate that maximizes the posterior distribution. Hence, under the assumption of Gaussian distributions, the probabilistic approach and the one of this study are equivalent. Both can adequately characterize the posterior by providing a mean model and a covariance of the model parameters. Fig. 5.5 shows the estimated mode coefficients from Sec. 4.2 with the uncertainty extracted from the diagonal elements of the a priori and a posteriori model covariance matrices. A shortcoming of the

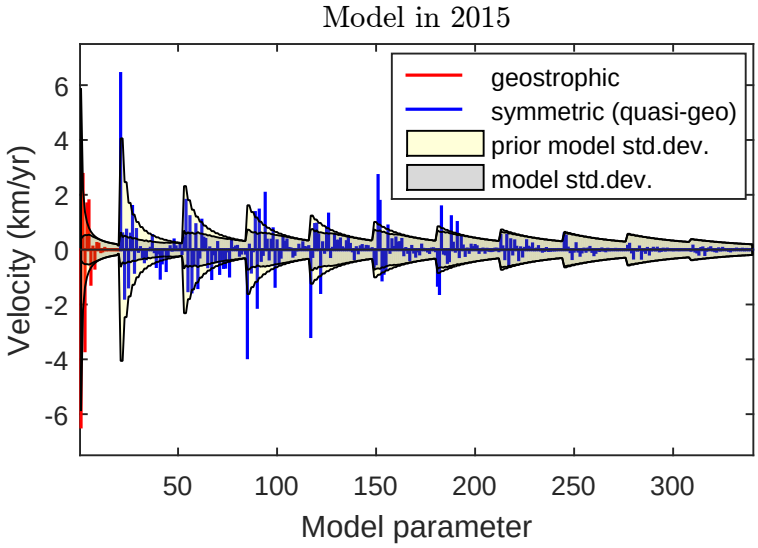

Figure 5.5. Estimated mode coefficients in 2015 (Sec. 4.2) with prior and posterior model uncertainty.

approach used here is the choice of the regularization parameter λ. It would be better to specify this a priori, as done in the probabilistic approach.

The uncertainty of the magnetic field itself cannot be included in the approach of this study. But Mosegaard and Rygaard-Hjalsted (1999) have shown that it is possible in a probabilistic framework. The Likelihood probability density in Eq. (5.2) then becomes non-Gaussian and the MCMC algorithm must be applied to sample the posterior (Mosegaard and Rygaard-Hjalsted, 1999). They also show that the model is better resolved (non-uniqueness and uncertainty) than in the non-probabilistic approach. A probabilistic inversion using the geostrophic and inertial modes of this study and fitting directly to satellite and ground data with their uncertainties is an attractive way forward in the future.

One challenge will be to specify more useful prior information on the modes, in order to restrict the model space. For example, the QG mode inversions involve 564 model parameter; this would be very difficult to sample using a MCMC algorithm. Perhaps the use of a reduced model (Sec. 5.2) may be helpful in this regard.

6. Conclusions

In this thesis, a new scheme has been developed for predicting the secular variation (SV) of Earth's magnetic field given a core flow based on normal modes in a rotating fluid sphere. The choice of this scheme for representing the core flow is motivated by the dynamical balance expected in Earth's core and it allows a suitable modeling of the flow especially in mid and low latitudes. The error of the SV prediction associated with unknown small-scale fields at the core surface was accounted for by introducing a small-scale error term that augmented the vector containing the flow model coefficients. This forward scheme has then been used as the basis for inverting radial SV from the CHAOS-6-x2 geomagnetic field model to infer the core flow. Two types of regularization were explored in the inversion method. First, a standard l_2-norm of the horizontal divergence and vorticity of the flow and second, a new approach based on an l_1-norm which penalized the amplitudes of the normal modes. The latter approach required an iterative numerical scheme for estimating the model.

A benchmark test demonstrated that the developed inversion scheme could successfully reproduce previous results by using an l_2-norm regularizing the horizontal divergence and the radial vorticity. Further, by instead using an l_1-norm to regularize mode amplitudes, models were obtained that were dominated by relatively few modes. Considering only QG modes, the inferred flow became very rough at mid and low latitudes due to increased power allowed in the small-scale flow. The effect of increasing regularization was studied, showing that although the power in the modes was decreased, the power in the small-scale error then increased. The time-dependence of the inferred core flow was studied by estimating flow snapshots at different epochs between 1999 and 2016. The obtained flow models showed good agreement with LOD observations until 2010 but deviated somewhat thereafter, perhaps due to the lack of satellite data in 2010-2013. Considering the time-dependence of the flow model based on the QG modes, it was found that some modes had noticeable high rms velocities and rms accelerations over the considered time interval. They were therefore used in an un-regularized (for the flow) inversion scheme in an attempt to determine a reduced model. Although the overall performance of this reduced model was less good (in terms of misfit to the SV) compared to the other models, it successfully

reproduced SA pulses in 2006, 2009 and 2013.

In conclusion, the developed forward and inversion scheme based on normal modes in a rotating fluid sphere works well but now requires further investigation. For example in how best to specify prior information on the modes to restrict the model space. A further shortcoming is the missing time correlation of the small-scale error, and the present inconsistency between the estimated large-scale flow and spatial covariance of the small-scale error.

Coming back to geomagnetic jerks, this study was able to estimate core flow at low and mid latitudes with a QG mode-based inversion that reproduced SA patches when pulses occurred in 2006, 2009 and 2013, and the related geomagnetic jerks. Around these locations, strong time-dependent azimuthal flow structures were inferred. This suggests that the time-dependence of these features may be the origin of these pulses and hence of geomagnetic jerks.

In a future work, the inversion should be carried out by directly using magnetic observations from satellites and ground observatories including their estimated uncertainties and not, as in this study, indirectly using the predictions of a geomagnetic model.

Bibliography

Amit, H., P. Olson, and U. Christensen (2007). "Tests of core flow imaging methods with numerical dynamos." In: *Geophysical Journal International* 168.1, pp. 27–39 (cit. on p. 37).

Aster, R. C., B. Borchers, and C. H. Thurber (2013). *Parameter Estimation and Inverse Problems second edition Elsevier Inc* (cit. on p. 31).

Aubert, J. (2013). "Flow throughout the Earth's core inverted from geomagnetic observations and numerical dynamo models." In: *Geophysical Journal International* 192.2, pp. 537–556 (cit. on p. 34).

Backus, George E (1968). "Kinematics of geomagnetic secular variation in a perfectly conducting core." In: *Philosophical Transactions of the Royal Society of London A: Mathematical, Physical and Engineering Sciences* 263.1141, pp. 239–266 (cit. on pp. 19, 24).

Baerenzung, J., M. Holschneider, and V. Lesur (2014). "Bayesian inversion for the filtered flow at the Earth's core-mantle boundary." In: *Journal of Geophysical Research: Solid Earth* 119.4, pp. 2695–2720 (cit. on p. 45).

Barrois, O., N. Gillet, and J. Aubert (2017). "Transient motions within the Earth's core under realistic constraints." In: *Geophysical Journal International*. (under review) (cit. on pp. 34, 58).

Bloxham, J. and A. Jackson (1991). "Fluid flow near the surface of Earth's outer core." In: *Reviews of Geophysics* 29.1, pp. 97–120 (cit. on pp. 20, 25).

Chulliat, A. and S. Maus (2014). "Geomagnetic secular acceleration, jerks, and a localized standing wave at the core surface from 2000 to 2010." In: *Journal of Geophysical Research: Solid Earth* 119.3, pp. 1531–1543 (cit. on p. 3).

Chulliat, A., E. Thebault, and G. Hulot (2010). "Core field acceleration pulse as a common cause of the 2003 and 2007 geomagnetic jerks." In: *Geophysical Research Letters* 37.7 (cit. on p. 3).

Farquharson, C. G. and D. W. Oldenburg (1998). "Non-linear inversion using general measures of data misfit and model structure." In: *Geophysical Journal International* 134.1, pp. 213–227 (cit. on pp. 32, 33).

Finlay, C. C., M. Dumberry, A. Chulliat, and M. A. Pais (2010). "Short timescale core dynamics: theory and observations." In: *Space science reviews* 155.1-4, pp. 177–218 (cit. on pp. 2, 6, 8, 18, 19).

Finlay, C. C., N. Olsen, S. Kotsiaros, N. Gillet, and L. Tøffner-Clausen (2016). "Recent geomagnetic secular variation from Swarm." In: *Earth, Planets and Space* 68.1, pp. 1–18 (cit. on pp. 4, 22, 23, 56).

Gillet, N., O. Barrois, and C. C. Finlay (2015a). "Stochastic forecasting of the geomagnetic field from the COV-OBS. x1 geomagnetic field model, and candidate models for IGRF-12." In: *Earth, Planets and Space* 67.1, p. 71 (cit. on p. 24).

Gillet, N., D. Jault, and C. C. Finlay (2015b). "Planetary gyre, time-dependent eddies, torsional waves, and equatorial jets at the Earth's core surface." In: *Journal of Geophysical Research: Solid Earth* 120.6, pp. 3991–4013 (cit. on pp. 4, 24, 36–40, 48, 51, 52, 58, 60).

Gillet, N., M. A. Pais, and D. Jault (2009). "Ensemble inversion of time-dependent core flow models." In: *Geochemistry, Geophysics, Geosystems* 10.6 (cit. on pp. 25, 34, 39).

Greenspan, H. P. (1968). *The theory of rotating fluids*. CUP Archive (cit. on p. 7).

Holme, R. (2015). *Large-Scale Flow in the Core. In: Treatise on Geophysics*. Ed. by Gerald Schubert (editor-in-chief). 2nd. Vol. 8. p. 91-113. Elsevier (cit. on pp. 2, 20, 48).

Ivers, D. J., A. Jackson, and D. Winch (2015). "Enumeration, orthogonality and completeness of the incompressible Coriolis modes in a sphere." In: *Journal of Fluid Mechanics* 766, pp. 468–498 (cit. on p. 9).

Jackson, A., J. Bloxham, and D. Gubbins (1993). "Time-dependent flow at the core surface and conservation of angular momentum in the coupled core-mantle system." In: *Dynamics of Earth's Deep Interior and Earth Rotation*, pp. 97–107 (cit. on pp. 48, 51).

Jault, D. (2008). "Axial invariance of rapidly varying diffusionless motions in the Earth's core interior." In: *Physics of the Earth and Planetary Interiors* 166.1, pp. 67–76 (cit. on pp. 8, 39).

Jault, D. and J. L. Le Mouël (1991). "Physical properties at the top of the core and core surface motions." In: *Physics of the Earth and Planetary Interiors* 68.1-2, pp. 76–84 (cit. on p. 19).

Leopardi, P. (2006). "A partition of the unit sphere into regions of equal area and small diameter." In: *Electronic Transactions on Numerical Analysis* 25.12, pp. 309–327 (cit. on p. 30).

Liao, X. and K. Zhang (2010a). "A new Legendre-type polynomial and its application to geostrophic flow in rotating fluid spheres." In: *Proceedings of the Royal Society of London A: Mathematical, Physical and Engineering Sciences* (cit. on p. 10).

Liao, X. and K. Zhang (2010b). "Asymptotic and numerical solutions of the initial value problem in rotating planetary fluid cores." In: *Geophysical Journal International* 180.1, pp. 181–192 (cit. on pp. 12, 13, 16).

Livermore, P. W., R. Hollerbach, and C. C. Finlay (2017). "An accelerating high-latitude jet in Earth's core." In: *Nature Geoscience* 10.1, pp. 62–68 (cit. on p. 30).

Lloyd, D. and D. Gubbins (1990). "Toroidal fluid motion at the top of the Earth's core." In: *Geophysical Journal International* 100.3, pp. 455–467 (cit. on p. 26).

Mandea, M., R. Holme, A. Pais, K. Pinheiro, A. Jackson, and G. Verbanac (2010). "Geomagnetic jerks: rapid core field variations and core dynamics." In: *Space science reviews* 155.1, pp. 147–175 (cit. on p. 3).

Mosegaard, K. and C. Rygaard-Hjalsted (1999). "Probabilistic analysis of implicit inverse problems." In: *Inverse problems* 15.2, p. 573 (cit. on pp. 62, 63).

Mosegaard, K. and A. Tarantola (1995). "Monte Carlo sampling of solutions to inverse problems." In: *Journal of Geophysical Research: Solid Earth* 100.B7, pp. 12431–12447 (cit. on p. 62).

Olsen, N., G. Hulot, and T. J. Sabaka (2010). "Sources of the Geomagnetic Field and the Modern Data That Enable Their Investigation." In: *Handbook of Geomathematics*. Springer, pp. 105–124 (cit. on pp. 1, 2).

Pais, M. A. and D. Jault (2008). "Quasi-geostrophic flows responsible for the secular variation of the Earth's magnetic field." In: *Geophysical Journal International* 173.2, pp. 421–443 (cit. on p. 8).

Rau, S., U. Christensen, A. Jackson, and J. Wicht (2000). "Core flow inversion tested with numerical dynamo models." In: *Geophysical Journal International* 141.2, pp. 485–497 (cit. on p. 37).

Sabaka, T. J., G. Hulot, and N. Olsen (2010). "Mathematical Properties Relevant to Geomagnetic Field Modeling." In: *Handbook of Geomathematics*. Springer, pp. 504–536 (cit. on pp. 20, 21, 23).

Schaeffer, N., D. Jault, H. Nataf, and A. Fournier (2017). "Geodynamo simulations with vigorous convection and low viscosity." In: *arXiv preprint arXiv:1701.01299* (cit. on p. 3).

Tarantola, A. (2005). *Inverse problem theory and methods for model parameter estimation*. SIAM (cit. on p. 60).

Zhang, K., P. Earnshaw, X. Liao, and F. H. Busse (2001). "On inertial waves in a rotating fluid sphere." In: *Journal of Fluid Mechanics* 437, pp. 103–119 (cit. on pp. 9, 12, 13, 16).

A. Example Code

The code was written in MATLAB R2015a and requires additional functions which can be supplied on request.

A.1. l_1-Regularized Inversion

```
%% ======================================================================
%%% L1-Regularisation on Grid using CHAOS-6-x2
%%%======================================================================

set(0,'defaulttextinterpreter','latex')
set(0,'defaultaxesfontsize',10.8);
set(0,'defaulttextfontsize',10.8);

%define radii of Earth's surface and CMB in km
r_surf = 6371.2;
r_cmb = 3485;
lat_tc = 30; %distance of TC, co-latitude in degree
theta_tc = lat_tc*pi/180; %in radians

%load MF and SV from CHAOS6
time = 2015; %epoch
load('./CHAOS-6-x2.mat'); %load spline coefficients of CHAOS-6-x2
g_mf_chaos = fnval(jd2000(time, 1, 1), pp, 0); %MF
g_sv_chaos = fnval(jd2000(time, 1, 1), fnder(pp, 1))*365.25; %SV
n_sv = 14; %harmonic degree of SV
n_mag = n_sv; %harmonic degree of MF
```

```
g_mf_chaos = g_mf_chaos(1:n_mag*(n_mag+2)); %adjust ↩
    coefficients vector
g_sv_chaos = g_sv_chaos(1:n_sv*(n_sv+2));

%load variance structure of SV from COVOBS.x1 (1840 - 2015)
fid = './SV_CovMat_COVOBS.x1_1840_2015_1y.dat';
time_covmat = 2005; %epoch of SV variance
num_row = time_covmat - 1840;
P=n_sv*(n_sv+2);
line=dlmread(fid,'',[num_row 0 num_row P*(P+1)/2-1]);
var_sv=zeros(P,1); %stores variance of SV
for j=1:P
    i=j;
    var_sv(i)=line(i + (j-1)*j/2);
end

%make sv variance isotropic
spec = powerspec(sqrt(var_sv),n_sv,'Surface');
var_sv = zeros(size(var_sv));
for n=1:n_sv
    var_sv(n^2:(n+1)^2-1) = spec(n)/(n+1)*ones(2*n+1,1);
end

%load covariance of small-scale error term
P_ee = dlmread('Pee_divhudeltaBr_N-trunc%3d14.dat');
invP_ee = inv(P_ee);

%load toroidal/poloidal coefficients of normal modes
load '\modes\zon20_qgN10M16'
% load '\modes\zon20_symN5M10'
% load '\modes\zon20_symN5M10_asymN5M10'
M = [Tor_coeff;Pol_coeff];

%generate equal area grid outside TC
num = 20000; %number of points
points_s = transpose(eq_point_set_polar(2,num));
phi_tangent = points_s(:,1); %azimuth
```

```
58 theta_tangent = points_s(:,2); %co-latitude
59
60 idx = (theta_tangent >= theta_tc & theta_tangent <= (pi-↩
       theta_tc));
61 phi_tangent = phi_tangent(idx); %extract point outside TC
62 theta_tangent = theta_tangent(idx);
63 r_tangent = r_cmb/r_surf*ones(size(theta_tangent)); %at CMB
64
65 %produce matrix to go from spherical harmonics to grid
66 G_gauss2grid = design_SHA(r_tangent,theta_tangent,phi_tangent,↩
       n_sv);
67
68 %Compute matrix for forward problem
69 A = SV_synthesis(n_mag,n_v,n_sv,g_mf_chaos); %induction ↩
       equation
70 H = A*M;
71 H_aug = [H,eye(n_sv*(n_sv+2))]; %augmented state description
72 H_aug_grid = G_gauss2grid*H_aug;
73
74 %Gillet Flow 2005 (for comparison)
75 load ./Gillet_flow_2005.mat %first half toroidal/ second half ↩
       poloidal
76 n_Gillet = 20; %harmonic degree of expansion
77 T_Gillet = Flow_Gillet(1:n_Gillet*(n_Gillet+2)); %toroidal
78 S_Gillet = Flow_Gillet(n_Gillet*(n_Gillet+2)+1:end); %poloidal
79
80 %data weight matrix
81 Cov_sv = diag(var_sv); %assume uncorrelated SV Gauss ↩
       coefficients
82 Cov_sv_grid = G_gauss2grid*Cov_sv*G_gauss2grid'; %covariance ↩
       of SV on grid
83 Cov_sv_grid = diag(diag(Cov_sv_grid)); %only diagonal elements
84 H2_aug_grid=H_aug_grid'*(Cov_sv_grid\H_aug_grid);
85 B_obs = G_gauss2grid*g_sv_chaos; %gridded SV
86
87 %augmented data vector for inversion
88 d = H_aug_grid'*(Cov_sv_grid\B_obs);
```

```
89
90 %% L-curve
91
92 %predefine arrays for L-curve output
93 % lambda_exp=linspace(-1.8,3,40);
94 lambda_exp=log10(2.4174); %specify lambda
95 reg_norm2=zeros(size(lambda_exp));
96 misfit=reg_norm2;
97 cor = zeros(size(lambda_exp));
98 cor2 = zeros(size(lambda_exp));
99 all_a_aug = NaN(size(H_aug,2),length(lambda_exp));
100
101 %initial values for non-linear solver
102 eps = 1e-5; %for small values, norm tends to Lp-norm
103 Niter_max = 300; %maximal number of iterations
104 delta_min = 1e-2; %convergence threshold of solution ↩
    difference
105
106 for i=1:length(lambda_exp)
107
108     %L1-Regularization nonlinear solver
109     lambda = 10^lambda_exp(i);
110
111     R = eye(size(H,2)); %initial matrix for Ekblom measure
112     R_aug = blkdiag(lambda*R,invP_ee); %augmented ↩
        regularization
113
114     G = H2_aug_grid + R_aug; %update sytem matrix
115     a_aug = G\d; %update model vector
116
117     Niter = 1;
118     delta = 1;
119     while delta>delta_min && Niter<=Niter_max
120         a = a_aug(1:size(M,2)); %extract flow amplitudes
121         R = diag(1./sqrt(a.^2+eps^2)); %update Ekblom measure
122         R_aug = blkdiag(lambda*R,invP_ee); %augmented ↩
            regularization
```

```
123         a_aug_old = a_aug;
124         G = H2_aug_grid + R_aug; %update sytem matrix
125         a_aug=G\d; %update model vector
126 
127         delta = max(abs(a_aug-a_aug_old));
128         Niter = Niter+1;
129     end
130 
131     if Niter == Niter_max+1 && delta>delta_min
132         disp(['maximum number of iterations reached (delta = '↩
                ,num2str(delta),')']);
133         disp(['lambda = ',num2str(lambda)])
134         misfit(i) = NaN;
135         reg_norm2(i) = NaN;
136         cor(i) = NaN;
137         cor2(i) = NaN;
138     else
139         %write L-curve output
140         all_a_aug(:,i) = a_aug;
141         misfit(i)=((H_aug_grid*a_aug-B_obs)'*(Cov_sv_grid\(↩
                H_aug_grid*a_aug-B_obs)));
142         a = a_aug(1:size(M,2)); %flow amplitudes
143         reg_norm2(i)=a'*R*a;
144         cor(i) = flow_correlation(T_Gillet,Tor_coeff*a,↩
                S_Gillet,Pol_coeff*a);
145         cor2(i) = point_recovery(T_Gillet,Tor_coeff*a,S_Gillet↩
                ,Pol_coeff*a);
146     end
147 end
148 
149 %plot L-curve (L1-Regularization^2 over misfit^2)
150 fig1=figure(1);
151 dcm_obj = datacursormode(fig1);
152 set(dcm_obj,'DisplayStyle','Window','Enable','on')
153 scatter3(misfit,reg_norm2,1:length(lambda_exp),[],lambda_exp,'↩
    filled','DisplayName','L-curve')
154 hold on
```

```
155 plot(misfit,cor,'DisplayName','Pattern cor.')
156 plot(misfit,cor2,'DisplayName','Point cor.')
157 hold off
158 view(2)
159 grid off
160 set(gca,'xscale','log','yscale','log','TicklabelInterpreter','latex')
161 xlabel('misfit at CMB')
162 ylabel('$||a||^2_R$ $(\mathrm{km}/\mathrm{yr})^2$')
163 c=colorbar;
164 ylabel(c,'$\log\lambda$','Interpreter','latex')
165 legend('toggle')
166
167 %% Statistics on selected solution
168
169 %select solution and compute covariances
170 idx_lambda = 1;
171 a_aug = all_a_aug(:,idx_lambda);
172 a = a_aug(1:size(M,2)); %flow amplitudes
173 e = a_aug(size(M,2)+1:end); %co-estimated small-scale error
174
175 R = diag(1./sqrt(a.^2+eps^2));
176 R_aug = blkdiag(10^lambda_exp(idx_lambda)*R,invP_ee); %augmented regularization
177 Cov_a_aug = inv(H2_aug_grid + R_aug);
178 Cov_a_aug_prior = blkdiag(10^-lambda_exp(idx_lambda)*eye(size(H,2)),P_ee); %when initializing nonlinear solver
179
180 %% Make plots
181
182 %estimated flow power spectra at CMB
183 T = Tor_coeff*a; %toroidal flow coefficients
184 S = Pol_coeff*a; %poloidal flow coefficients
185 g = g_sv_chaos;
186 g_pred_ls = H*a; %SV due to flow and large-scale MF interaction
187 g_pred = g_pred_ls + e; %total predicted SV
```

```
188 g_diff = g_pred - g; %residual SV
189 T_diff = T(1:min(length(T),length(T_Gillet)))-T_Gillet(1:min(length(T),length(T_Gillet)));
190 S_diff = S(1:min(length(S),length(S_Gillet)))-S_Gillet(1:min(length(S),length(S_Gillet)));
191
192 %predefine arrays for spectra
193 nmax = 25; %maximum spherical harmonic degree for plotting
194 powspec_tor = zeros(nmax,1);
195 powspec_pol = zeros(nmax,1);
196 powspec_tor_Gillet = zeros(n_Gillet,1);
197 powspec_pol_Gillet = zeros(n_Gillet,1);
198 powspec_sv = zeros(n_sv,1);
199 powspec_pred = zeros(n_sv,1);
200 powspec_pred_ls = zeros(n_sv,1);
201 powspec_diff = zeros(n_sv,1);
202 powspec_var = zeros(n_sv,1);
203 powspec_e = zeros(n_sv,1);
204 powspec_tor_diff = zeros(min(n_sv,n_Gillet),1);
205 powspec_pol_diff = zeros(min(n_sv,n_Gillet),1);
206
207 %flow power spectra per independent mode
208 for n=1:nmax
209     powspec_tor(n) = n*(n+1)*rms(T(n^2:((n+1)^2-1)))^2;
210     powspec_pol(n) = n*(n+1)*rms(S(n^2:((n+1)^2-1)))^2;
211 end
212
213 for n=1:n_Gillet
214     powspec_tor_Gillet(n) = n*(n+1)*rms(T_Gillet(n^2:((n+1)^2-1)))^2;
215     powspec_pol_Gillet(n) = n*(n+1)*rms(S_Gillet(n^2:((n+1)^2-1)))^2;
216 end
217
218 for n=1:min(n_Gillet,nmax)
219     powspec_tor_diff(n) = n*(n+1)*rms(T_diff(n^2:((n+1)^2-1)))^2;
```

```
220     powspec_pol_diff(n) = n*(n+1)*rms(S_diff(n^2:((n+1)^2-1)))^2;
221 end
222
223 %SV power spectra (sum over independent modes)
224 r=r_cmb/r_surf; %CMB radius in units of surface radius
225 for n=1:n_sv
226     powspec_sv(n) = (n+1)*r^-(2*n+4)*sum(g(n^2:((n+1)^2-1)).^2);
227     powspec_pred_ls(n) = (n+1)*r^-(2*n+4)*sum(g_pred_ls(n^2:((n+1)^2-1)).^2);
228     powspec_pred(n) = (n+1)*r^-(2*n+4)*sum(g_pred(n^2:((n+1)^2-1)).^2);
229     powspec_diff(n) = (n+1)*r^-(2*n+4)*sum(g_diff(n^2:((n+1)^2-1)).^2);
230     powspec_e(n) = (n+1)*r^-(2*n+4)*sum(e(n^2:((n+1)^2-1)).^2);
231     powspec_var(n) = (2*n+1)*r^-(2*n+4)*spec(n);
232 end
233
234 %Rau's correlation coefficient
235 cor_pattern = flow_correlation(T_Gillet,T,S_Gillet,S);
236
237 %pointwise recovery factor (Amit et al. 2007)
238 cor_point = point_recovery(T_Gillet,T,S_Gillet,S);
239
240 %-------------------------------------------------------------------------
241 %plot spectra
242
243 fig2=figure(2);
244 fig2.Units = 'normalized';
245 fig2.OuterPosition=[0 0.05 1 0.95];
246
247 %toroidal flow spectra
248 subplot(1,3,1)
249 plot(1:nmax,powspec_tor,'r-','Marker','none','LineWidth',1.2,'DisplayName','toroidal flow (km/yr)^2')
```

```
250 hold on
251 plot(1:n_Gillet,powspec_tor_Gillet,'b-','Marker','none','↩
    LineWidth',1.2,'DisplayName','Gillet toroidal flow (km/yr)↩
    ^2')
252 plot(1:min(n_Gillet,nmax),powspec_tor_diff,'k--','Marker','↩
    none','LineWidth',1.2,'DisplayName','toroidal flow diff. (↩
    km/yr)^2')
253 hold off
254 set(gca,'yscale','log','TicklabelInterpreter','latex','YTick'↩
    ,10.^(-4:2:4))
255 axis([0 nmax 1e-4 1e4])
256 xlabel('Spherical harmonic degree n')
257 ylabel('Flow power spectra per harm. mode (km/yr)$^2$')
258 title('Toroidal Flow Power Spectra at CMB')
259 legend('Location','northwest')
260
261 %poloidal flow spectra
262 subplot(1,3,2)
263 plot(1:nmax,powspec_pol,'r-','Marker','none','LineWidth',1.2,'↩
    DisplayName','poloidal flow (km/yr)^2')
264 hold on
265 plot(1:n_Gillet,powspec_pol_Gillet,'b-','Marker','none','↩
    LineWidth',1.2,'DisplayName','Gillet poloidal flow (km/yr)↩
    ^2')
266 plot(1:min(n_Gillet,nmax),powspec_pol_diff,'k--','Marker','↩
    none','LineWidth',1.2,'DisplayName','poloidal flow diff. (↩
    km/yr)^2')
267 hold off
268 set(gca,'yscale','log','TicklabelInterpreter','latex','YTick'↩
    ,10.^(-4:2:4))
269 axis([0 nmax 1e-4 1e4])
270 xlabel('Spherical harmonic degree n')
271 ylabel('Power per harm. mode (km/yr)$^2$')
272 title('Poloidal Flow Power Spectra at CMB')
273 legend('Location','northwest')
274
275 %sv power spectra
```

```
subplot(1,3,3)
plot(1:n_sv,powspec_sv,'k-','Marker','none','LineWidth',1.2,'DisplayName','SV model (CHAOS-6) (nT/yr)^2')
hold on
plot(1:n_sv,powspec_var,'k-.','Marker','none','LineWidth',1.2,'DisplayName','SV obs. error (nT/yr)^2')
plot(1:n_sv,powspec_pred,'b-','Marker','none','LineWidth',1.2,'DisplayName','SV prediction (large + small) (nT/yr)^2')
plot(1:n_sv,powspec_diff,'b-.','Marker','none','LineWidth',1.2,'DisplayName','SV diff. (large + small) (nT/yr)^2')
plot(1:n_sv,powspec_pred_ls,'r-','Marker','none','LineWidth',1.2,'DisplayName','SV large-scales (nT/yr)^2')
plot(1:n_sv,powspec_e,'-','Color',[1,0.6,0],'Marker','none','LineWidth',1.2,'DisplayName','SV small-scales (nT/yr)^2')
hold off
set(gca,'yscale','log','TicklabelInterpreter','latex','YTick',10.^(-2:2:8))
axis([0 n_sv 1e-2 1e8])
xlabel('Spherical harmonic degree n')
ylabel('Power per degree (nT)$^2$')
title('SV Power Spectra at CMB')
legend('Location','southeast')

%-------------------------------------------------------------------------
%plot flow maps

%equal-spaced grid for plot
TMax=81;
theta=(1:(TMax-1)/2)'*2*pi/TMax; %excludes poles
PMax=TMax-1;
phi=(0:PMax-1)'*2*pi/PMax;
[phi_grid,theta_grid]=meshgrid(phi,theta);

%generate flow pattern for plot
Q = TorPol_synthesis(n_v,theta_grid(:),phi_grid(:));
Q_theta = Q(1:end/2,:);
Q_phi = Q(end/2+1:end,:);
```

```
306
307 %velocity components
308 v_theta=Q_theta*M*a;
309 v_theta_grid=reshape(v_theta,size(theta_grid));
310 v_phi=Q_phi*M*a;
311 v_phi_grid=reshape(v_phi,size(theta_grid));
312
313 %generate grid of SV at CMB
314 Step = 0.25;
315 lat_B = 0:Step:180;
316 lon_B = -180:Step:180;
317 B_r_sv = synth_grid(H*a,r_cmb/r_surf,fliplr(lat_B),lon_B); %↩
    large-scale SV prediction
318 B_r_sv_res = synth_grid(H*a+e-g_sv_chaos,r_cmb/r_surf,fliplr(↩
    lat_B),lon_B); %measured SV
319 B_r_sv_e = synth_grid(e,r_cmb/r_surf,fliplr(lat_B),lon_B); %↩
    measured SV
320
321 rad=180/pi;
322 lat_v=90-theta_grid*rad;
323 lon_v=phi_grid*rad;
324
325 B_ref =  makerefmat('RasterSize', size(B_r_sv), ...
326     'Latlim', [-90 90], 'Lonlim', [-180 180]);
327
328 C_1=35000; %nT
329 v_scale = 25; %km/yr
330 load coast;
331
332 fig3=figure(3);
333 % fig3.Units = 'centimeters';
334 % fig3.Position=[0 5 16 15];
335 fig3.Units = 'normalized';
336 fig3.OuterPosition=[0 0.05 1 0.95];
337
338 %reference arrow
```

```
339 axes('Position',[0.01 0.11 0.78 0.76]-[0 0.4 0 0], 'Box', 'off↩
    ')
340 axesm('MapProjection','hammer','Frame', 'off','FLineWidth',1)
341 quiverm(0,0,0,5,'k',0)
342 set(gca, 'Box', 'off', 'Visible', 'off')
343 tightmap
344 text(0.5,0.47,[num2str(v_scale),' km/yr'], 'Color', 'k','Units↩
    ', 'normalized', 'HorizontalAlignment', 'Center','↩
    Interpreter','latex')
345
346 %B_r_sv and flow
347 axes('Position',[0.01 0.11 0.78 0.76], 'Box', 'off')
348 axesm('MapProjection', 'hammer', 'Frame', 'on','FLineWidth',1,↩
    'Grid','on','GLineStyle','-')
349 meshm(B_r_sv, B_ref)
350 hold on
351 quiverm(lat_v,lon_v,-v_theta_grid*(5/v_scale),v_phi_grid*(5/↩
    v_scale),'k',0)
352 plotm(lat, long, '-k','Linewidth',0.5)
353 plotm((90-lat_tc)*ones(size(lon_B)),lon_B,'-r','Linewidth',2)
354 plotm(-(90-lat_tc)*ones(size(lon_B)),lon_B,'-r','Linewidth',2)
355 hold off
356 set(gca, 'Box', 'off', 'Visible', 'off')
357 caxis(C_1*[-1 1])
358 tightmap
359 nio_colormap2
360 text(0.5, 1.1,['flow and pred. SV of large-scale field in ',↩
    num2str(time,'%4.1f')], 'Color', 'k','Units', 'normalized',↩
     'HorizontalAlignment', 'Center','Interpreter','latex')
361
362 %colorbar
363 axes('Position', [0.92 0.35 .03 0.3], 'Box', 'off')
364 image([length(map):-1:1]', 'YData', [C_1 -C_1]);
365 set(gca,'YTick',(-C_1:C_1/2:C_1), 'YtickLabel',(-C_1/1000:C_1↩
    /2000:C_1/1000),'yaxislocation','right','Xdir', 'Normal', '↩
    FontWeight', 'normal', 'Xcolor', 'k', 'XTickLabel', {}, '↩
    Ydir', 'Normal','TicklabelInterpreter','latex')
```

```
366 text(0.5, -0.1,'$\mu\mathrm{T}$ / yr', 'Color', 'k','Units', '↩
      normalized', 'HorizontalAlignment', 'Center','Interpreter',↩
      'latex')
367
368 %B_r_sv plot of small-scale error
369 axes('Position',[0.63 0.65 0.4 0.3], 'Box', 'off')
370 axesm('MapProjection', 'hammer', 'Frame', 'on','FLineWidth',1,↩
      'Grid','on','GLineStyle','-')
371 meshm(B_r_sv_e, B_ref)
372 hold on
373 plotm(lat, long, '-k','Linewidth', 1)
374 plotm((90-lat_tc)*ones(size(lon_B)),lon_B,'-r','Linewidth',2)
375 plotm(-(90-lat_tc)*ones(size(lon_B)),lon_B,'-r','Linewidth',2)
376 hold off
377 set(gca, 'Box', 'off', 'Visible', 'off')
378 caxis(C_1*[-1 1])
379 tightmap
380 nio_colormap2
381 text(0.5, 1.1,['small-scale error (n = ',num2str(n_sv),')'], '↩
      Color', 'k','Units', 'normalized', 'HorizontalAlignment', '↩
      Center','Interpreter','latex')
382
383 %B_r_sv map of residuals
384 axes('Position',[0.63 0.02 0.4 0.3], 'Box', 'off')
385 axesm('MapProjection', 'hammer', 'Frame', 'on','FLineWidth',1,↩
      'Grid','on','GLineStyle','-')
386 meshm(B_r_sv_res, B_ref)
387 hold on
388 plotm(lat, long, '-k','Linewidth', 1)
389 plotm((90-lat_tc)*ones(size(lon_B)),lon_B,'-r','Linewidth',2)
390 plotm(-(90-lat_tc)*ones(size(lon_B)),lon_B,'-r','Linewidth',2)
391 hold off
392 set(gca, 'Box', 'off', 'Visible', 'off')
393 caxis(C_1*[-1 1])
394 tightmap
395 nio_colormap2
```

```
396 text(0.5, 1.1,['residuals (n = ',num2str(n_sv),')'], 'Color', ↩
    'k','Units', 'normalized', 'HorizontalAlignment', 'Center',↩
    'Interpreter','latex')
397
398 %-------------------------------------------------------------------
399 %plot amplitudes of modes
400 kmax=inistruct.zonal.kmax;
401 Nmax_sym=inistruct.symmetric.Nmax;
402 Mmax_sym=inistruct.symmetric.Mmax;
403 Nmax_asym=inistruct.antisymmetric.Nmax;
404 Mmax_asym=inistruct.antisymmetric.Mmax;
405
406 fig4=figure(4);
407 fig4.Units = 'normalized';
408 fig4.OuterPosition=[0 0.05 1 0.95];
409
410 lim=10;
411
412 stem(1:kmax,a(1:kmax)','r','filled','Marker','none','LineWidth↩
    ',1.25,'DisplayName','zonal');
413 hold on
414 if strcmp(inistruct.symmetric.status,'on') && strcmp(inistruct↩
    .symmetric.qgeostrophy,'on')
415     stem(sum([kmax,1]):sum([kmax,2*Nmax_sym*Mmax_sym]),a(sum([↩
        kmax,1]):sum([kmax,2*Nmax_sym*Mmax_sym]))','b','filled'↩
        ,'Marker','none','LineWidth',1.25,'DisplayName','↩
        symmetric (quasi-geo)');
416     stem(sum([kmax,2*Nmax_sym*Mmax_sym,1]):sum([kmax,2*↩
        Nmax_sym*Mmax_sym,(Mmax_asym*(2*Nmax_asym*(Nmax_asym+2)↩
        +2))]),a(sum([kmax,2*Nmax_sym*Mmax_sym,1]):sum([kmax,2*↩
        Nmax_sym*Mmax_sym,(Mmax_asym*(2*Nmax_asym*(Nmax_asym+2)↩
        +2))]))','g','filled','Marker','none','LineWidth',1.25,↩
        'DisplayName','antisymmetric');
417 else
418     stem(sum([kmax,1]):sum([kmax,(2*Nmax_sym*Mmax_sym*(↩
        Nmax_sym+1))]),a(sum([kmax,1]):sum([kmax,(2*Nmax_sym*↩
        Mmax_sym*(Nmax_sym+1))]))','b','filled','Marker','none'↩
```

```
        ,'LineWidth',1.25,'DisplayName','symmetric');
419     stem(sum([kmax,(2*Nmax_sym*Mmax_sym*(Nmax_sym+1)),1]):sum↩
        ([kmax,2*Nmax_sym*Mmax_sym*(Nmax_sym+1),(Mmax_asym*(2*↩
        Nmax_asym*(Nmax_asym+2)+2))]),a(sum([kmax,2*Nmax_sym*↩
        Mmax_sym*(Nmax_sym+1),1]):sum([kmax,2*Nmax_sym*Mmax_sym↩
        *(Nmax_sym+1),(Mmax_asym*(2*Nmax_asym*(Nmax_asym+2)+2))↩
        ])),'g','filled','Marker','none','LineWidth',1.25,'↩
        DisplayName','antisymmetric');
420 end
421 var_amp = diag(Cov_a_aug);
422 var_amp = var_amp(1:size(M,2));
423 var_amp_prior = diag(Cov_a_aug_prior);
424 var_amp_prior = var_amp_prior(1:size(M,2));
425 fill([1:length(a) fliplr(1:length(a))],[sqrt(var_amp_prior)' -↩
    fliplr(sqrt(var_amp_prior)')],'y','FaceAlpha',0.15,'↩
    DisplayName','prior std.dev.')
426 fill([1:length(a) fliplr(1:length(a))],[sqrt(var_amp)' -fliplr↩
    (sqrt(var_amp)')],'k','FaceAlpha',0.15,'DisplayName','↩
    posterior std.dev.')
427 hold off
428 ylabel('Velocity (km/yr)')
429 axis([0.5,length(a)+0.5,-lim,lim])
430 title(['Solution in ',num2str(time)])
431 legend('toggle')
432
433 %-------------------------------------------------------------------
434 %Two Flow Map
435 T_Gillet2 = zeros(n_v*(n_v+2),1);
436 T_Gillet2(1:length(T_Gillet)) = T_Gillet;
437 S_Gillet2 = zeros(n_v*(n_v+2),1);
438 S_Gillet2(1:length(S_Gillet)) = S_Gillet;
439
440 v_Gillet_theta=Q_theta*[T_Gillet2;S_Gillet2];
441 v_Gillet_theta_grid=reshape(v_Gillet_theta,size(theta_grid));
442 v_Gillet_phi=Q_phi*[T_Gillet2;S_Gillet2];
443 v_Gillet_phi_grid=reshape(v_Gillet_phi,size(theta_grid));
444
```

```
445 fig5=figure(5);
446 fig5.Units = 'normalized';
447 fig5.OuterPosition=[0 0.05 0.55 0.95];
448 fig5.Color='white';
449
450 load coast;
451
452 %Flow Map
453 axes('Position',[0.125 0.36 0.75 0.75], 'Box', 'off')
454 axesm('MapProjection', 'hammer', 'Frame', 'on','FLineWidth',1,↩
      'Grid','on','GLineStyle','-')
455 hold on
456 quiverm(lat_v,lon_v,-v_theta_grid*(5/v_scale),v_phi_grid*(5/↩
      v_scale),'k',0)
457 plotm(lat, long, '-k','Linewidth',0.5)
458 hold off
459 set(gca, 'Box', 'off', 'Visible', 'off')
460 tightmap
461 text(0.5, 1.1,['Flow (CHAOS6 in ',num2str(time),')'], 'Color',↩
      'k','Units', 'normalized', 'HorizontalAlignment', 'Center'↩
     ,'Interpreter','latex')
462
463 %reference arrow
464 axes('Position',[0.125 0.36 0.75 0.75]+[0.3 -0.19 0 0], 'Box',↩
      'off')
465 axesm('MapProjection','hammer','Frame', 'off','FLineWidth',1)
466 quiverm(0,0,0,5,'k',0)
467 set(gca, 'Box', 'off', 'Visible', 'off')
468 tightmap
469 text(0.5,0.47,[num2str(v_scale),' km/yr'], 'Color', 'k','Units↩
     ', 'normalized', 'HorizontalAlignment', 'Center','↩
     Interpreter','latex')
470
471 %Gillet Flow Map
472 axes('Position',[0.125 -0.15 0.75 0.75], 'Box', 'off')
473 axesm('MapProjection', 'hammer', 'Frame', 'on','FLineWidth',1,↩
      'Grid','on','GLineStyle','-')
```

```
474 hold on
475 quiverm(lat_v,lon_v,-v_Gillet_theta_grid*(5/v_scale),↩
      v_Gillet_phi_grid*(5/v_scale),'k',0)
476 plotm(lat, long, '-k','Linewidth',0.5)
477 hold off
478 set(gca, 'Box', 'off', 'Visible', 'off')
479 tightmap
480 text(0.5, 1.1,'Gillet Ensemble Average (COV-OBS 2005)', 'Color↩
      ', 'k','Units', 'normalized', 'HorizontalAlignment', '↩
      Center','Interpreter','latex')
481
482 %-------------------------------------------------------------------
483 %plot mode amplitudes
484
485 fig6=figure(6);
486 fig6.Units = 'normalized';
487 fig6.OuterPosition=[0 0.05 1 0.95];
488
489 ax1 = gca;
490 hold on
491 amp_zon = abs(a(1:kmax));
492 phase_zon = atan2(zeros(size(amp_zon)),sign(a(1:kmax)));
493 stem(1:kmax,amp_zon','r','filled','Marker','none','LineWidth'↩
      ,1.25,'DisplayName','zonal');
494 if strcmp(inistruct.symmetric.status,'on') && strcmp(inistruct↩
      .symmetric.qgeostrophy,'on')
495     a_sym = a(sum([kmax,1]):sum([kmax,2*Nmax_sym*Mmax_sym]));
496     amp_sym = sqrt(a_sym(1:2:(end-1)).^2+a_sym(2:2:end).^2);
497     phase_sym = atan2(a_sym(2:2:end),a_sym(1:2:(end-1)));
498     a_asym = a(sum([kmax,2*Nmax_sym*Mmax_sym,1]):sum([kmax,2*↩
        Nmax_sym*Mmax_sym,(Mmax_asym*(2*Nmax_asym*(Nmax_asym+2)↩
        +2))]));
499     amp_asym = sqrt(a_asym(1:2:(end-1)).^2+a_asym(2:2:end).^2)↩
        ;
500     phase_asym = atan2(a_asym(2:2:end),a_asym(1:2:(end-1)));
501     stem(sum([kmax,1]):sum([kmax,Nmax_sym*Mmax_sym]),amp_sym',↩
        'b','filled','Marker','none','LineWidth',1.25,'↩
```

```
        DisplayName','symmetric (quasi-geo)');
502     stem([kmax,Nmax_sym*Mmax_sym,1]):sum([kmax,Nmax_sym*Mmax_sym,(Mmax_asym*(Nmax_asym*(Nmax_asym+2)+1))]),amp_asym','g','filled','Marker','none','LineWidth',1.25,'DisplayName','antisymmetric');
503     ylabel('Amplitude (km/yr)')
504     axis([0.5,(length(a)+kmax)/2+0.5,0,lim])
505     legend('Location','northeast')
506 else
507     a_sym = a(sum([kmax,1]):sum([kmax,(2*Nmax_sym*Mmax_sym*(Nmax_sym+1))]));
508     amp_sym = sqrt(a_sym(1:2:(end-1)).^2+a_sym(2:2:end).^2);
509     phase_sym = atan2(a_sym(2:2:end),a_sym(1:2:(end-1)));
510     a_asym = a(sum([kmax,2*Nmax_sym*Mmax_sym*(Nmax_sym+1),1]):sum([kmax,2*Nmax_sym*Mmax_sym*(Nmax_sym+1),(Mmax_asym*(2*Nmax_asym*(Nmax_asym+2)+2))]));
511     amp_asym = sqrt(a_asym(1:2:(end-1)).^2+a_asym(2:2:end).^2);
512     phase_asym = atan2(a_asym(2:2:end),a_asym(1:2:(end-1)));
513     stem(sum([kmax,1]):sum([kmax,(Nmax_sym*Mmax_sym*(Nmax_sym+1))]),amp_sym','b','filled','Marker','none','LineWidth',1.25,'DisplayName','symmetric');
514     stem(sum([kmax,(Nmax_sym*Mmax_sym*(Nmax_sym+1)),1]):sum([kmax,Nmax_sym*Mmax_sym*(Nmax_sym+1),(Mmax_asym*(Nmax_asym*(Nmax_asym+2)+1))]),amp_asym','g','filled','Marker','none','LineWidth',1.25,'DisplayName','antisymmetric');
515     ylabel('Amplitude (km/yr)')
516     axis([0.5,(length(a)+kmax)/2+0.5,0,lim])
517     legend('Location','northeast')
518 end
519 hold off
520 title(['Mode Amplitude in ',num2str(time,'%4.1f')])
```

DTU Space
National Space Institute
Technical University of Denmark

Elektrovej, building 327
DK - 2800 Kgs. Lyngby
Tel (+45) 4525 9500
Fax (+45) 4525 9575

www.space.dtu.dk